Photonic Devices for Integrated Optical Applications

Nicholas David Psaila BSc(Hons) MSc

Submitted for the degree of Doctor of Philosophy

Heriot Watt University

School of Engineering and Physical Sciences

March 2010

ABSTRACT

The work presented in this thesis encompasses an investigation into the use of ultrafast laser inscription in the fabrication of glass based photonic devices for integrated optical applications. Waveguide fabrication and characterisation experiments were carried out in three categories of glass substrate.

Firstly, waveguides were inscribed in an erbium doped glass with the aim of fabricating optical amplifiers and lasers operating in the 1.5 μm spectral region. Low loss waveguides were fabricated in substrates with different dopant concentrations. Fibre to fibre net gain was achieved from one substrate composition, however it was found that ion clustering limited the amount of achievable gain. Laser action was demonstrated by constructing an optical fibre based cavity around the erbium doped waveguide amplifier.

Waveguides were also inscribed in bismuth doped glass with the aim of fabricating optical amplifiers and lasers operating in the 1.3 μm spectral region. Low loss waveguides were fabricated, however the initial composition was incapable of providing gain. A proven substrate material was employed, demonstrating ultra-broadband gain spanning more than 250 nm. High losses prevented the achievement of net gain, however the broad potential of the substrate material was highlighted.

Finally, waveguides were inscribed in a Chalcogenide glass. Strong refractive index contrasts were observed, with a wide range of waveguiding structures produced. Supercontinuum experiments were carried out in order to confirm the nonlinear behaviour of the waveguides. A spectrally smooth supercontinuum spanning 600 nm was generated, providing a potentially useful source for optical coherence tomography.

ACKNOWLEDGEMENTS

First and foremost I would like to thank my supervisor Ajoy Kar who has provided great support, friendship and kindness during my time as a PhD student. His vast experience, patience and outlook are inspirational. Ajoy has been an invaluable source of guidance throughout my time at Heriot Watt.

I would also like to acknowledge the immense support from my colleagues Robert Thomson and Henry Bookey, from whom I have learned a great deal, both inside and outside the laboratory.

I would like to thank our collaborators at the Politecnico di Milano, specifically Roberto Osellame, Giulio Cerullo and Nicola Chiodo, who helped make my visits there fruitful and always made me feel extremely welcome. Without them this work would not have been possible.

I thank our collaborators at the University of Leeds, specifically Animesh Jha and Shaoxiong Shen for their support and glass making skills. I also thank our collaborators at the University of Osaka, Specifically Yasushi Fujimoto for providing glass samples and spending time to take me on amazing visits to Kyoto and Nara.

I would like to thank all the Heriot Watt support staff, specifically Peter Heron and Mark Stewart in the mechanical workshop who have had to put up with my incessant need for holes to be drilled in metal plates.

The unconditional support I have received from my Mum and Dad over the years has been instrumental in my progress in life. It is undeniable that I owe a great deal to their patience and love. Without them I certainly would not be where I am now.

Last but certainly not least, I thank my fiancée Helena for her relentless love and support throughout my PhD. In particular I thank her great patience with the many weeks apart she has endured on my various trips abroad, and all the late nights and weekends I have spent making this PhD possible. I am extremely lucky to have someone so special.

CONTENTS

Abstract ..... **i**

Acknowledgements ..... **ii**

List of Figures ..... **vi**

List of Abbreviations ..... **ix**

List of Publications by the Author ..... **xii**

CHAPTER 1 - INTRODUCTION **1**

1.1 Integrated Optics as a concept 1

1.2 Integrated Optical Devices 1

1.3 Fabrication of Integrated Optical Devices 5

1.3.1 Glass film deposition techniques for waveguide fabrication 5

1.3.2 Implantation techniques for waveguide fabrication 8

1.3.3 Direct-write waveguide fabrication 9

1.4 Thesis outline 12

CHAPTER 2 – REVIEW OF ULTRAFAST LASER INSCRIPTION **14**

2.1 The origin of guided modes 14

2.2 Ultrashort pulses in dielectric materials 18

2.2.1 Energy absorption mechanisms 19

2.2.2 Material modification from ultrashort pulses 24

2.2.3 Photonic applications of ultrafast laser inscription 28

CHAPTER 3 – WAVEGUIDE INSCRIPTION IN OXYFLUORIDE SILICATE GLASS **36**

3.1 Introduction 36

3.2 Erbium-doped gain media 37

3.2.1 Rare Earth Ions 37

3.2.2 Erbium doped glasses as gain media 38

3.2.3 Erbium doped oxyfluoride silicate glass 41

3.2.4 Ultrafast laser inscribed waveguides in Erbium doped substrates 42

3.2.5 The cavity-dumped stretched cavity oscillator 44

3.3 Waveguide fabrication in oxyfluoride silicate glass 47

3.3.1 Absorption spectra of OSG samples 47

3.3.2 Initial waveguide fabrication experiments 50

3.3.3 Waveguide morphology and guided modes 52

3.3.4 Loss characterisation 55

3.3.5 Optimised waveguide fabrication experiments 62

3.4 Gain investigation of OSG waveguides 64

3.4.1 Gain measurements 64
3.5 Demonstration of laser action 70
3.5.1 Formation of a laser cavity using an Er:Yb doped OSG waveguide 70
3.5.2 Laser emission from an Er:Yb doped OSG waveguide 71
3.6 Conclusions and further work 74

CHAPTER 4 – WAVEGUIDE INSCRIPTION IN BISMUTH DOPED GLASS 76
4.1 Introduction 76
4.2 Bi-doped glass as a gain medium 77
4.2.1 Origins of luminescence 77
4.2.2 Active Bi-doped devices 79
4.3 Waveguide Inscription in Bi:LAZS 81
4.3.1 Initial fabrication experiments 81
4.3.2 Waveguide morphology and guided modes 82
4.3.3 Loss characterisation 87
4.3.4 Refractive index profiling 92
4.3.5 Fluorescence measurements 96
4.3.6 Gain measurements 99
4.4 Waveguide inscription in Bi:alumino-Silica 102
4.4.3 Substrate material provided by Osaka University 102
4.4.4 Waveguide fabrication 103
4.4.5 Waveguide morphology 104
4.4.6 Guided mode profiles 106
4.4.7 Gain measurements 108
4.5 Conclusions and further work 113

CHAPTER 5 – WAVEGUIDE INSCRIPTION IN CHALCOGENIDE GLASS 115
5.1 Introduction 115
5.2 Chalcogenide glasses 116
5.2.1 Introduction to chalcogenides 116
5.2.2 Applications of chalcogenides 117
5.3 Waveguide fabrication in Chalcogenide glass 120
5.3.1 ONL2 Glass 120
5.3.2 Waveguide fabrication 121
5.3.3 Waveguide morphology 122
5.3.4 Guiding properties 128
5.4 Supercontinuum Generation Experiments 133
5.4.1 Supercontinua 133
5.4.2 Experimental setup 134
5.4.3 Supercontinuum results 135
5.5. Conclusions and further work 139

CHAPTER 6 – CONCLUSIONS AND FUTURE WORK 141
6.1 Conclusions 141
6.2 Future work 142

References 145

Appendix 164

LIST OF FIGURES

Figure 1-1. Schematic diagram of a 1 to 4 port AWG. 2

Figure 1-2. Schematic diagram of an integrated MZI for switching applications. 3

Figure 1-3. Schematic diagram of an integrated optical waveguide amplifier. 4

Figure 1-4. Schematic diagram of FHD waveguide fabrication 6

Figure 1-5. Schematic diagram of ultrafast laser waveguide inscription 10

Figure 2-1. Graph showing fundamental MFD *vs* core diameter for a square core cross-section waveguide. 16

Figure 2-2. Photo-ionisation mechanisms and corresponding Keldysh parameter, showing processes of liberating an electron from the Coulomb potential [11]....20

Figure 2-3. Diagram showing energy depletion as the pulse is focussed. Intensities above the nonlinear absorption threshold I_{th} are quickly absorbed, causing a capping to the peak intensity of the pulse and subsequent energy deposition before the focus [23]. 23

Figure 2-4. Schematic diagram of waveguide fabrication geometry. Transverse geometry is shown on the left, where the sample is translated perpendicular to the laser axis. Longitudinal geometry is shown on the right where the sample is translated parallel to the laser axis. 29

Figure 3-1. Energy level scheme of Erbium ions in a glass substrate [91]....39

Figure 3-2. Overhead view of the cavity dumped oscillator 46

Figure 3-3. Alternate view of the cavity dumped oscillator 46

Figure 3-4. Absorption spectra for Er-doped OSG samples P4, P1, and P7. 48

Figure 3-5. Absorption spectra for Er:Yb-doped OSG samples P10, P11 and P15....49

Figure 3-6. Schematic diagram of waveguide fabrication setup 51

Figure 3-7. Schematic diagram of the multi-scan technique. 51

Figure 3-8. a) - c) Guided mode profiles for three multi-scan waveguides. d) - f) Corresponding microscope facet images of the same waveguides. 53

Figure 3-9. a) - c) Guided mode profiles for three single-scan waveguides. d) - f) Corresponding microscope facet images. 54

Figure 3-10. Schematic diagram of IL characterisation setup. 55

Figure 3-11. Insertion loss, Coupling loss and Propagation loss for 40-scan waveguides. 57

Figure 3-12. Insertion loss, Coupling loss and Propagation loss for 20-scan waveguides. 59

Figure 3-13. Insertion loss, Coupling loss and Propagation loss for single-scan waveguides. 61

Figure 3-14. a) Graph showing IL results for 20-scan waveguides. b) Graph showing IL results for 40-scan waveguides. 62

Figure 3-15. a) Microscope facet image of the optimal waveguide. b) Guided mode profile of the optimal waveguide. 63

Figure 3-16. Schematic diagram of gain characterisation experimental setup. 65

Figure 3-17. Relative gain, total insertion loss and net gain spectra for the optimal waveguide parameters fabricated in sample P11. 67

Figure 3-18. Graph showing relative gain *vs* pump power using a tunable laser source as the signal. 68

Figure 3-19. Graph showing a comparison of internal gain per unit length for varying dopant concentrations. 69

Figure 3-20. Graph showing normalised reflectivity spectra of the two FBGs used to form a laser cavity. 70

Figure 3-21. Schematic diagram of the cavity configuration used to form a waveguide laser. 71

Figure 3-22. Graph showing the evolution of the laser output spectrum as a function of 980 nm pump power. 72

Figure 3-23. Graph showing laser output power versus input pump power for both 980- and dual-wavelength pumping schemes. Inset shows the fine laser spectrum at maximum pump power. 73

Figure 4-1. Microscope facet images showing the evolution of the waveguide cross section as a function of pulse energy for both single and 20-scan waveguides. 83

Figure 4-2. Waveguide facet and corresponding guided mode images for various waveguides. SMF-28 fibre is shown for comparison in k) and l). 85

Figure 4-3. Loss measurements for single-scan waveguides. a) Insertion loss, b) Coupling loss per facet, c) Propagation loss per unit length. 88

Figure 4-4. Loss measurements for 40-scan waveguides. a) Insertion loss, b) Coupling loss per facet, c) Propagation loss per unit length. 90

Figure 4-5. Loss measurements for 20-scan waveguides. a) Insertion loss, b) Coupling loss per facet, c) Propagation loss per unit length. 91

Figure 4-6. Schematic diagram of RNF profilometry, adapted for profiling silica-on-silicon waveguides [134]. 93

Figure 4-7. a), b) Optical microscope images of waveguide facets taken in transmission mode, c) d) refractive index profiles, e) f) near field guided mode profiles taken at 1320 nm. a) c) e) Lowest insertion loss single-scan waveguide, b) d) f) Lowest insertion loss multi-scan waveguide. 95

Figure 4-8. a) Optical microscope image of the waveguide facet, b) refractive index profile. 96

Figure 4-9. Photograph of visible upconversion visible from the waveguide under pumping. 97

Figure 4-10. a), c) Fluorescence emission for the lowest IL multi-scan waveguide. b), d) fluorescence emission from the lowest IL single-scan waveguide. a) and b) were pumped with 60 mW at 810 nm, c) and d) were pumped with 980 nm. 98

Figure 4-11. Experimental setup for gain measurements. 100

Figure 4-12. Comparison of the fluorescence (a), b)) and relative gain (c), d)) for the bulk sample (a), c)), and lowest IL single-scan waveguide (b), d)). 101

Figure 4-13. Bulk fluorescence spectra for Bi-doped alumino-silica glass pumped with up to 190 mW at 810 nm and 600 mW at 980 nm. 103

Figure 4-14. Microscope facet images for various structures. The left column shows multi-scan structures, the right column single scan structures for the same pulse energy and translation speed. All structures shown were fabricated with a translation speed of 1 mm/s. 105

Figure 4-15. Microscope facet images and corresponding guided mode profiles of various waveguides. SMF-28 fibre is included for comparison in i) and j). 107

Figure 4-16. Experimental setup for insertion loss and gain measurements. 109

Figure 4-17. Relative gain spectra for waveguide G1. a) 810 nm pumping, b) 980 nm pumping. 110

Figure 4-18. Relative gain spectra for waveguide G2. a) 810 nm pumping, b) 980 nm pumping. 111

Figure 5-1. Absorption spectrum of ONL2 chalcogenide glass. 121

Figure 5-2. Microscope cross-sectional facet images of waveguides, showing scaling with both translation speed and pulse energy. The left column shows waveguides with a pulse energy of 492 nJ and varying translation speed, and the right column shows waveguides written with a 250 μm/s translation speed and varying pulse energy. The bottom two images show the same waveguide. 123

Figure 5-3. Graphs showing variations in the dimensions of the fabricated structures. a) Horizontal size, b) Vertical size. 124

Figure 5-4. Graph showing variation in aspect ratio as a function of fabrication parameters. The inset image shows the measurements used for obtaining the data. The errors were calculated from the relative contributions from the uncertainties in the edges of the structures.....126

Figure 5-5. Graph showing depth dependence of the waveguide from the sample surface. 127

Figure 5-6. Schematic diagram of experimental setup for capturing near-field guided mode images. 128

Figure 5-8. Microscope facet images and corresponding near-field guided mode images at 1480 nm for low pulse-energy waveguides.....130

Figure 5-9. Single-mode guiding. a) microscope facet image, b) corresponding single guided-mode at 1480 nm. c) intensity line plots through the guided mode. The mode image captured from the camera was gamma corrected and normalised to obtain b) and c). 131

Figure 5-10. Experimental setup for supercontinuum generation. 134

Figure 5-11. Supercontinuum generation from the ultrafast laser inscribed waveguide. 136

Figure 5-12. Supercontinuum generation when pumped with the idler port of the OPA tuned to 2.4 μm. 137

LIST OF ABBREVIATIONS

ASE	Amplified Spontaneous Emission
AWG	Arrayed Waveguide Grating
CET	Co-operative Energy Transfer
CL	Coupling Loss
CNT	Carbon Nanotube
CVD	Chemical Vapour Deposition
CW	Continuous Wave
CWDM	Coarse Wavelength Division Multiplexing
EDFA	Erbium Doped Fibre Amplifier
EDWA	Erbium Doped Waveguide Amplifier
ESA	Excited State Absorption
FBG	Fibre Bragg Grating
FHD	Flame Hydrolysis Deposition
FOM	Figure of Merit
FWHM	Full Width Half Maximum
FWM	Four Wave Mixing
GSA	Ground State Absorption
GVD	Group Velocity Dispersion
IL	Insertion Loss
IO	Integrated Optics
KGW	Potassium-Gadolinium-Tungstate
LAN	Local Area Network
LIB	Laser Induced Breakdown
MAN	Metropolitan Area Network
MFD	Mode Field Diameter
MOPA	Master Oscillator Power Amplifier

MPA	Multiphoton Absorption
MPI	Multiphoton Ionisation
MZI	Mach-Zehnder Interferometer
NA	Numerical Aperture
NBOHC	Non-bridging Oxygen Hole Centre
ND	Neutral Density
NMR	Nuclear Magnetic Resonance
NOLM	Nonlinear Optical Loop Mirror
OCT	Optical Coherence Tomography
OPA	Optical Parametric Amplifier
OSA	Optical Spectrum Analyser
OSG	Oxyfluoride Silicate Glass
PDL	Polarisation Dependant Loss
PDG	Polarisation Dependant Gain
PI	Physik Instrumente
PL	Propagation Loss
PLD	Pulsed Laser Deposition
PVD	Physical Vapour Deposition
RE	Rare Earth
RI	Refractive Index
RNF	Refracted Near Field
WDM	Wavelength Division Multiplexing
TDM	Time Division Multiplexing
ULI	Ultrafast Laser Inscription
UV	Ultraviolet
SESAM	Semiconductor Saturable Absorber Mirror
SLED	Superluminescent Light Emitting Diode
SPM	Self Phase Modulation

SRS	Stimulated Raman Scattering
TI	Tunnelling Ionisation
USAF	United States Air Force
XPM	Cross Phase Modulation

LIST OF PUBLICATIONS BY THE AUTHOR

Journal Papers

[1] R. R. Thomson, H. T. Bookey, **N. Psaila**, S. Campbell, D. T. Reid, S. X. Shen, A. Jha, and A. K. Kar, "Internal gain from an erbium-doped oxyfluoride-silicate glass waveguide fabricated using femtosecond waveguide inscription," *IEEE Photonics Technology Letters*, **18**, 1515 (2006).

[2] **N. D. Psaila**, R. R. Thomson, H. T. Bookey, A. K. Kar, N. Chiodo, R. Osellame, G. Cerullo, G. Brown, A. Jha, and S. Shen, "Femtosecond laser inscription of optical waveguides in bismuth ion doped glass," *Optics Express,* **14**, 10452 (2006).

[3] **N. D. Psaila**, R. R. Thomson, H. T. Bookey, A. K. Kar, N. Chiodo, R. Osellame, G. Cerullo, A. Jha, and S. Shen, "Er : Yb-doped oxyfluoride silicate glass waveguide amplifier fabricated using femtosecond laser inscription," *Applied Physics Letters*, **90**, (2007).

[4] **N. D. Psaila**, R. R. Thomson, H. T. Bookey, S. X. Shen, N. Chiodo, R. Osellame, G. Cerullo, A. Jha, and A. K. Kar, "Supercontinuum generation in an ultrafast laser inscribed chalcogenide glass waveguide," *Optics Express,* **15**, 15776 (2007).

[5] H. T. Bookey, J. Lousteau, A. Jha, N. Gayraud, R. R. Thomson**, N. D. Psaila**, H. Li, W. N. MacPherson, J. S. Barton, and A. K. Kar, "Multiple rare earth emissions in a multicore tellurite fiber with a single pump wavelength," *Optics Express*, **15**, 17554 (2007).

[6] H. T. Bookey, R. R. Thomson, **N. D. Psaila**, A. K. Kar, N. Chiodo, R. Osellame, and G. Cerullo, "Femtosecond laser inscription of low insertion loss waveguides in Z-cut lithium niobate," *IEEE Photonics Technology Letters*, **19**, 892 (2007).

[7] R. Osellame, M. Lobino, N. Chiodo, M. Marangoni, G. Cerullo, R. Ramponi, H. T. Bookey, R. R. Thomson, **N. D. Psaila**, and A. K. Kar, "Femtosecond laser writing of waveguides in periodically poled lithium niobate preserving the nonlinear coefficient," *Applied Physics Letters*, **90**, (2007).

[8] R. R. Thomson, H. T. Bookey, **N. D. Psaila**, A. Fender, S. Campbell, W. N. MacPherson, J. S. Barton, D. T. Reid, and A. K. Kar, "Ultrafast-laser inscription of a three dimensional fan-out device for multicore fiber coupling applications," *Optics Express*, **15**, 11691 (2007).

[9] **N. D. Psaila**, R. R. Thomson, H. T. Bookey, N. Chiodo, S. Shen, R. Osellame, G. Cerullo, A. Jha, and A. K. Kar, "Er : Yb-doped oxyfluoride silicate glass waveguide laser fabricated using ultrafast laser inscription," *IEEE Photonics Technology Letters*, **20**, 126 (2008).

[10] F.M. Bain, A.A. Lagatsky, R.R. Thomson, **N.D. Psaila**, N.V. Kuleshov, A.K. Kar, W. Sibbett, and C.T.A. Brown, "Ultrafast laser inscribed Yb:KGd$(WO_4)_2$ and Yb:KY$(WO_4)_2$ channel waveguide lasers," *Optics Express,* **17**, 22417 (2009).

Conference Papers

[1] **N. D. Psaila**, R. R. Thomson, H. T. Bookey, A. K. Kar, N. Chiodo, R. Osellame, G. Cerullo, S. Shen, and A. Jha, "Laser action from an Er : Yb-doped oxyfluoride silicate glass waveguide fabricated using femtosecond laser inscription," *2007 Pacific Rim Conference on Lasers and Electro-Optics*, **Vols 1-4**, 808 (2007).

[2] **N. D. Psaila**, R. R. Thomson, H. T. Bookey, K. Kar, N. Chiodo, R. Osellame, G. Cerullo, G. Brown, S. Shen, and Jha, "Femtosecond Laser Inscription of Optical Waveguides in Bismuth Ion Doped Glass," *2007 Conference on Lasers & Electro-Optics/Quantum Electronics and Laser Science Conference,* **Vols 1-5**, 853 (2007).

[3] **N. D. Psaila**, R. R. Thomson, H. T. Bookey, K. Kar, N. Chiodo, R. Osellame, G. Cerullo, S. Shen, and Jha, "Er:Yb-doped Waveguide Amplifier Fabricated in Oxyfluoride Silicate Glass Using Femtosecond Laser Inscription," *2007 Conference on Lasers & Electro-Optics/Quantum Electronics and Laser Science Conference*, **Vols 1-5**, 1908 (2007).

[4] H. T. Bookey, R. R. Thomson, **N. D. Psaila**, A. K. Kar, N. Chiodo, R. Osellame, and G. Cerullo, "Multi-scan femtosecond laser waveguide inscription in z-cut lithium niobate," *2007 Pacific Rim Conference on Lasers and Electro-Optics*, **Vols 1-4**, 806 (2007).

[5] H. T. Bookey, R. R. Thomson, **N. D. Psaila**, K. Kar, N. Chiodo, R. Osellame, and G. Cerullo, "Low Insertion Loss Waveguides in Lithium Niobate using Multi-Scan Femtosecond Inscription," *2007 Conference on Lasers & Electro-Optics/Quantum Electronics and Laser Science Conference*, **Vols 1-5**, 1209 (2007).

[6] **N. Psaila**, R. R. Thomson, H. T. Bookey, A. K. Kar, Y. Fujimoto, M. Nakatsuka, N. Chiodo, R. Osellame, and G. Cerullo, "Ultra Broadband Gain from a Bismuth-doped Glass Waveguide Fabricated Using Ultrafast Laser Inscription," *2008 Conference on Lasers and Electro-Optics & Quantum Electronics and Laser Science Conference*, **Vols 1-9**, 2215 (2008).

[7] **N. D. Psaila**, R. R. Thomson, H. T. Bookey, A. K. Kar, N. Chiodo, R. Osellame, G. Cerullo, S. Shen, and A. Jha, "Waveguide Fabrication and Supercontinuum Generation in an Ultrafast Laser Inscribed Chalcogenide Glass Waveguide," *2008 Conference on Lasers and Electro-Optics & Quantum Electronics and Laser Science Conference*, **Vols 1-9**, 422 (2008).

[8] H. T. Bookey, R. R. Thomson, **N. D. Psaila**, A. K. Kar, J. Lousteau, A. Jha, N. Gayraud, H. Li, W. N. MacPherson, and J. S. Barton, "Three-core tellurite fiber with multiple rare earth emission," *2008 Conference on*

Lasers and Electro-Optics & Quantum Electronics and Laser Science Conference, **Vols 1-9**, 238 (2008).

[9] R. Osellame, N. Chiodo, M. Lobino, M. Marangoni, G. Cerullo, R. Ramponi, H. T. Bookey, R. R. Thomson, **N. Psaila**, and A. K. Kar, "Efficient second harmonic generation in femtosecond laser written optical waveguides on periodically poled lithium niobate - art. no. 688112," *Commercial and Biomedical Applications of Ultrafast Lasers Viii*, **6881**, 88112 (2008).

[10] R. R. Thomson, H. T. Bookey, **N. D. Psaila**, A. Fender, S. Campbell, W. N. Macpherson, J. S. Barton, D. T. Reid, and A. K. Kar, "Ultrafast laser inscription of a three dimensional fan-out device for multicore fiber coupling applications," *2008 Conference on Lasers and Electro-Optics & Quantum Electronics and Laser Science Conference*, **Vols 1-9**, 2812 (2008).

[11] R. R. Thomson, **N. D. Psaila**, H. T. Bookey, A. K. Kar, N. Chiodo, R. Osellame, G. Cerullo, S. Shen, and A. Jha, "Probing the $I^{-4}_{13/2}$ level lifetime of Er-ions embedded in ultrafast laser inscribed waveguides," *2008 Conference on Lasers and Electro-Optics & Quantum Electronics and Laser Science Conference*, **Vols 1-9**, 2838 (2008).

Book Chapters

[1] Robert R. Thomson, **Nicholas D. Psaila**, Henry T. Bookey, Derryck T. Reid and Ajoy K. Kar, “Controlling the cross-section of ultrafast laser inscribed optical waveguides,” To be published by Springer in Topics of Applied Physics, book title "Femtosecond laser micromachining: fabrication of photonic and microfluidic devices in transparent materials" Edited by Roberto Osellame, Giulio Cerullo and Roberta Ramponi.

CHAPTER 1 - INTRODUCTION

1.1 INTEGRATED OPTICS AS A CONCEPT

The concept of guiding light around a bend using total internal reflection was first established in the mid-19th century during demonstrations using illuminated liquid jets by Swiss physicist Daniel Colladon, and separately by French physicist Charles Babinet [1]. Despite being widely accredited with the discovery, the Irish physicist John Tyndall famously demonstrated the concept to the Royal Institution in 1854, some 12 years after the publication of Colladon's work [2]. The simple principle of guiding light in a transparent medium of higher refractive index (RI) than the surrounding medium has led to tremendous developments, revolutionising telecommunications and directly enabling the rapid expanse of the internet. The primary developments in guided wave optics have centred on optical fibres, however as electronic integrated circuits flourished, integrated optics (IO) emerged as a concept at the end of the 1960s, with seminal papers from Shubert and Harris [3] and later Tiens [4].

Inspired by the advances in electronic integrated circuits, research into IO devices has progressed steadily, however IO has not yet seen the vast scale of complexity present in electronics. This is primarily due to limitations in the size, functionality and geometry of the optical analogy of wires – waveguides. An optical waveguide can be defined as a dielectric structure that transports energy in the optical region of the electromagnetic spectrum. Typically, a waveguide employing total internal reflection as a guiding mechanism consists of a 'core' region that has a higher refractive index than the surrounding medium. This simple concept allows confinement of the radiation into a small area in and around the core, enabling routing and manipulation of the guided light.

1.2 INTEGRATED OPTICAL DEVICES

Currently, the primary application of IO devices is in compact telecommunications components. One example of such a device is an Arrayed

Waveguide Grating (AWG) as shown in Figure 1-1. AWGs are commonly used for wavelength division multiplexed (WDM) systems, whereby many wavelength channels can be combined or split in order to multiply usable bandwidth in an optical fibre communication system. Other components such as directional couplers, star couplers and Y-splitters are useful for power splitting and generating interactions between separate waveguides in order to harness useful phenomena such as interference.

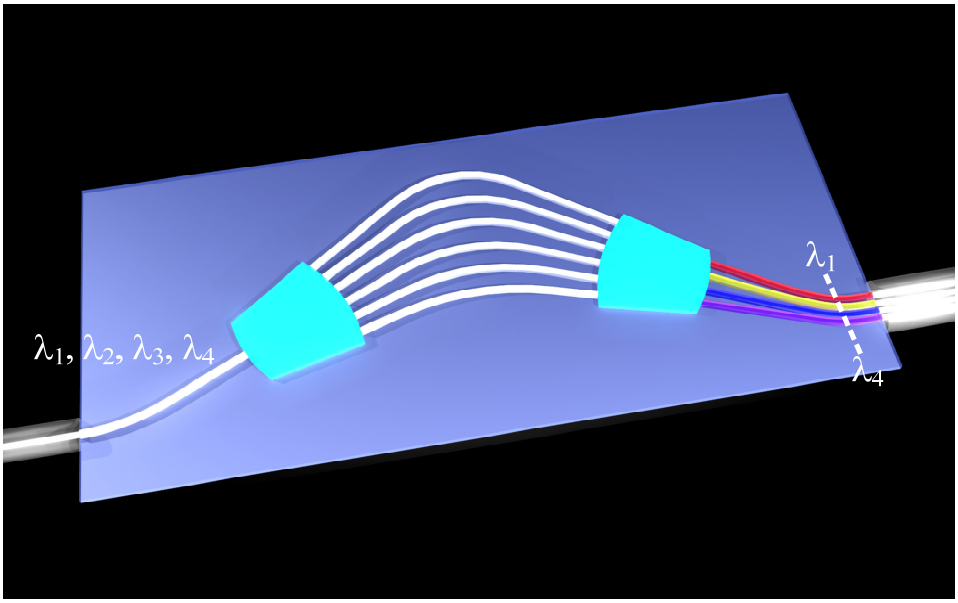

Figure 1-1. Schematic diagram of a 1 to 4 port AWG.

The integrated version of a Mach-Zehnder Interferometer (MZI) is commonly used in waveguide modulators and switches. In these devices, the waveguides are typically fabricated using a material with a high electro-optic coefficient, such as Lithium Niobate ($LiNbO_3$). Directional couplers or Y-splitters function as the power splitters and combiners. Typical commercial devices are capable of multi-GHz modulation rates, with drive voltages of approximately 5 V. Figure 1-2 shows a schematic diagram of an integrated MZI configured as a switch for time division multiplexing (TDM) or routing applications.

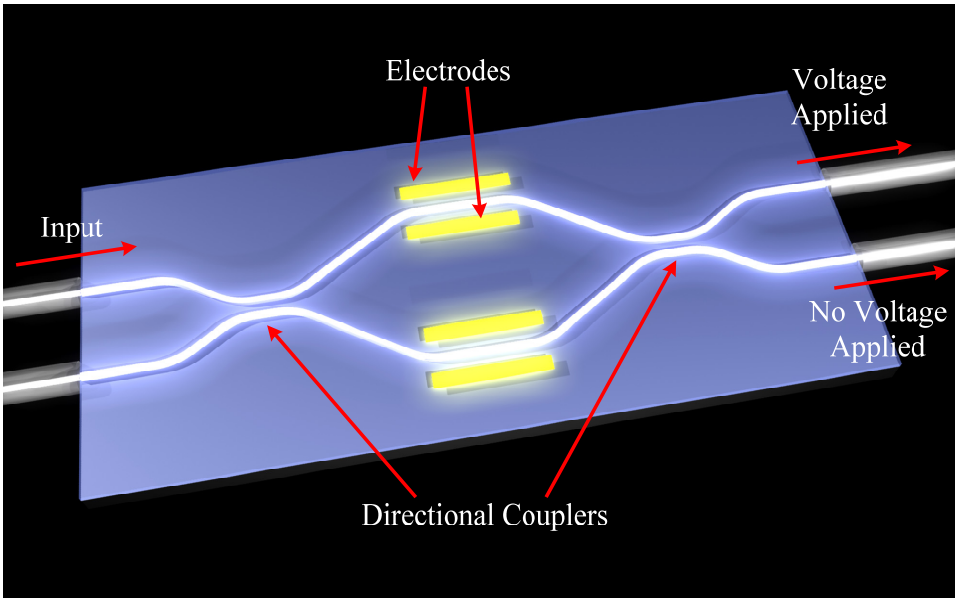

Figure 1-2. Schematic diagram of an integrated MZI for switching applications.

As waveguides have the capability to confine light into small volumes, high light intensities can be achieved over long lengths with relatively low input launch powers. This is of particular benefit for nonlinear devices, where the magnitude of the nonlinear effect is highly dependent on the electric field intensity. In the case of substrate materials with high third-order nonlinearities, this can be exploited for ultrafast all-optical signal processing applications such as high data rate wavelength conversion as demonstrated by Ta'eed *et al.* [5]. This was achieved using a 22.5 cm long As_2S_3 chalcogenide glass as the waveguide core material in an S-bend configuration. IO devices constructed out of materials exhibiting high second order nonlinearities also have major efficiency benefits over their bulk counterparts, and enable a whole host of parametric processes to be achieved at lower launch powers than would be required for bulk nonlinear crystals.

Optical sensors also benefit from a compact integrated architecture, enabling the combination of several functions into a single compact package. In particular, devices such as unbalanced MZIs enable high sensitivity measurements of refractive index or temperature. Combining microfluidic channels with waveguide components allows the realisation of multi-functional sensor devices.

Such devices can employ optical characterisation techniques such as analysing absorption, scattering and fluorescence to produce 'lab-on-chip' devices.

One important application of IO devices is in compact active devices such as optical amplifiers and lasers. In this case, the IO format can achieve significant cost and footprint savings. This is of particular importance for future local area networks (LAN) and metropolitan area networks (MAN) as they increasingly move from electronic to optical network architectures, and further into more advanced single-mode technologies employing WDM techniques. Erbium doped fibre amplifiers (EDFAs) are now a standard component in long-haul optical communications, dramatically improving the bandwidth and reducing the system complexity. This is due to their inherent capability to amplify WDM signals without returning to the electrical domain in order to provide gain. Their integrated-optical counterpart, the erbium-doped waveguide amplifier (EDWA) offers much the same functionality in a compact, low cost format. Such devices are commercially available, however considerable research interest exists in providing low-cost solutions and enabling amplification in other spectral regions in order to increase the available bandwidth. Figure 1-3 shows a schematic diagram of an IO waveguide amplifier.

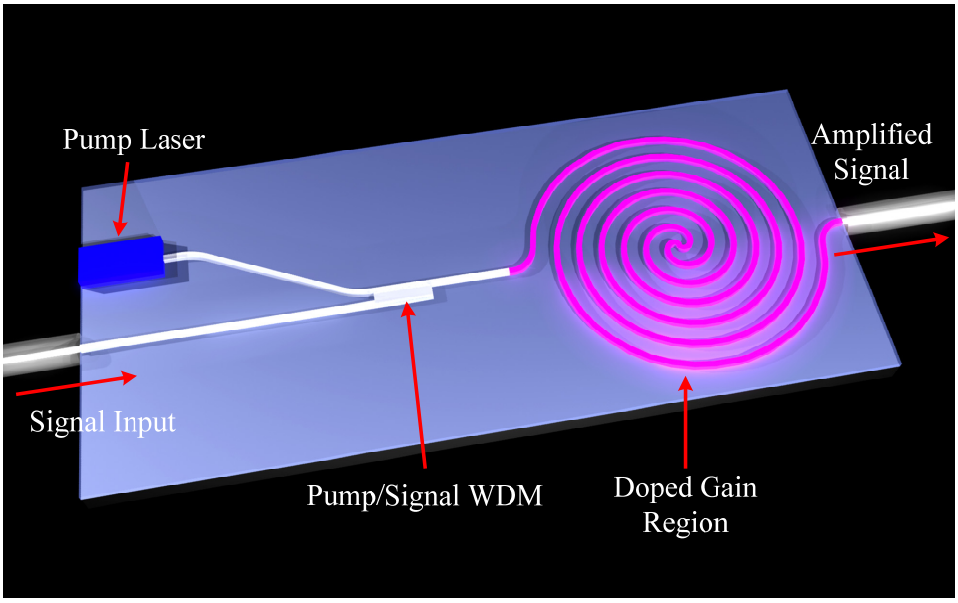

Figure 1-3. Schematic diagram of an integrated optical waveguide amplifier.

In the same manner that fibre lasers are displacing bulk solid state lasers in many areas, waveguide lasers offer many of the same inherent benefits such as simplicity and stability, combined with the compact size of an IO device. The ability to integrate arrays of individual lasers of different wavelengths onto a single substrate could be particularly useful as sources for course wavelength division multiplexing (CWDM) applications, replacing many diode signal lasers with a single pump diode. Significant interest also exists in fabricating compact mode-locked lasers. Such sources are inherently broadband and are of particular interest for sensing, and compact nonlinear optical applications.

1.3 FABRICATION OF INTEGRATED OPTICAL DEVICES

A wide variety of techniques are available for the fabrication of integrated optical devices. These can broadly be separated into two categories. Firstly, the most widely used and developed techniques rely on thin film deposition technologies in order to produce high quality optical films. The deposition processes are followed by further steps such as lithographic patterning and more film deposition to define the waveguide structures. An alternate approach for waveguide fabrication is to process a pre-fabricated material into a waveguide structure by locally raising the refractive index. This could be for example by impregnating dopants into the substrate material, or by directly inscribing a refractive index change using a laser or proton beam. Direct-write technologies have recently gained popularity due to the rapid fabrication time, reduced complexity and low number of process steps required to fabricate a device. The following sections will give an overview of the various waveguide fabrication techniques and their relative benefits.

1.3.1 Glass film deposition techniques for waveguide fabrication

The most widely adopted process for depositing glass films used for fabricating waveguides is Flame Hydrolysis Deposition (FHD). This multi-step process relies on depositing soot from an oxygen – hydrogen combustion flame onto a

silicon or glass substrate. Figure 1-4 shows a schematic diagram of the waveguide fabrication process.

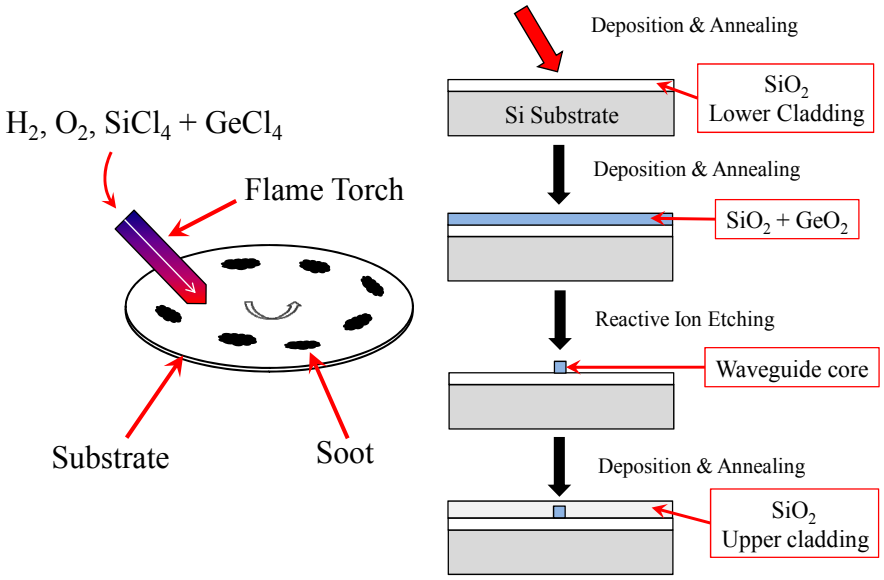

Figure 1-4. Schematic diagram of FHD waveguide fabrication .

The O_2/H_2 mixture is impregnated with $SiCl_4$, which upon combustion in the O_2/H_2 mixture, leaves behind a soot of SiO_2 particles. The soot is then baked to form a homogeneous layer of amorphous SiO_2. A further layer is deposited, with $GeCl_4$ added to the mixture, in order to leave behind a soot of SiO_2 and GeO_2. This is again baked to form a homogeneous layer having a higher refractive index than the pure SiO_2. Germanium as a dopant is also typically used to raise the refractive index in the core of standard silica optical fibres. The layer is then lithographically patterned with photo-resist and then etched to leave the waveguide core structures. A further SiO_2 cladding layer is then deposited to generate the complete device [6].

The FHD process is a relatively rapid thin film deposition technique, however it has severe material limitations based upon the chemistry required for deposition of the soot. It is highly scalable and capable of depositing structures with high levels of optical quality. It is for these reasons that FHD is widely used in the commercial fabrication of passive devices such as AWGs, for which silica is a suitable material.

Several other technologies for thin film deposition have been developed over the decades, with Physical Vapour Deposition (PVD) based techniques forming the bulk of these methods. PVD relies on depositing a continuous stream of vaporised particles onto a substrate. An accelerated gaseous ion is typically used to bombard a solid target, resulting in the ejection of a stream of target particles which are then deposited onto the substrate. The substrate may then be post-processed in order to produce a homogeneous layer. This deposition technique is also known as sputtering, or in the case where an electron beam is used to bombard the target it is known as E-beam evaporation. Chemical Vapour Deposition (CVD) differs from PVD techniques in that the deposition relies on a high temperature reduction or decomposition of a chemical vapour that is present around the substrate on which the film is to be grown. All the film deposition techniques described here are capable of producing high quality films of a wide variety of materials, however they are inherently slow relative to FHD [7].

Pulsed laser deposition (PLD) has emerged as an enhanced extension of PVD techniques, employing focussed high-energy laser pulses to directly ablate a target. The plume of vaporised material that is ejected from the target is collected on the substrate in order to produce film. The benefit of PLD is in the capability to deposit films that match the stoichiometry of the bulk target. A common problem with PLD fabrication is that the film quality is often highly granular with a poor optical quality, and the areas of deposition are particularly small and inhomogeneous. This makes PLD a process not yet well suited for commercial mass production [8].

Another film deposition technique that has gained popularity in recent years is the Sol-Gel process. This flexible chemical deposition process relies on spin coating a solution containing dissolved glass components onto the desired substrate. The resulting gel is then annealed to evaporate the solvent and densify the glass layer. Further film deposition and photo-lithography is employed, combined with reactive ion etching in order to fabricate waveguides and provide a cladding structure. The technique benefits from being able to use simple wet chemical

processing techniques, and takes place at relatively low temperatures relative to FHD, for example [9].

1.3.2 Implantation techniques for waveguide fabrication

Once a bulk material or thin film structure is fabricated, the required refractive index change must be induced in the required pattern to produce waveguides. As described earlier, this is often done by further deposition and photo-lithography, however an alternate approach is to modify the refractive index of the material to form the waveguide core. This can be achieved by implanting a new compositional component into the substrate through exchanging ions, or by diffusion.

Ion exchange is a well established waveguide fabrication technique that relies on replacing a constitutional component in the substrate with an introduced dopant. This dopant is commonly silver, to exchange with sodium present in the substrate. Ion exchange can be achieved by immersing the substrate in a molten salt bath in order for the ions to diffuse in and out of a region close to the surface of the sample. Field-assisted ion exchange can be achieved by depositing a layer of the desired dopant onto the sample surface. An applied electric field drives the ion migration from the deposited layer into the substrate, avoiding the need for a molten salt bath. Ion exchange has limited material applicability due to the stringent requirements upon glass composition set by the few pairs of cations available for exchange. However, the process can be used on films or in bulk materials, and is capable of producing embedded waveguides by a further ion exchange step, replacing the dopant with the original ion [10].

Another well established technique that is commonly used is that of in-diffusion. This involves lithographically defining the waveguide structure by depositing and patterning a photoresist layer. A layer of the required diffusion dopant is then deposited on the sample surface. The sample is then heated to a high temperature and held there for several hours. The dopant then thermally diffuses into the substrate, generating the required refractive index change. This process is

routinely used in industry to produce waveguides in lithium niobate, with titanium commonly used as the in-diffused dopant. This waveguide fabrication technique is capable of generating large refractive index changes, and low propagation losses [11].

1.3.3 Direct-write waveguide fabrication

The direct-write concept has emerged as a simple, adaptable technique for producing integrated optical devices. The process involves a directed or focussed beam modifying the refractive index of a small area of the substrate material. This is accompanied by an appropriate translation of the substrate or beam to write a waveguiding structure. The method used to change the refractive index can be an extension of implantation methods in the form of proton or electron beam writing, or by direct photo-modification typically using a laser.

Continuous wave (CW) laser writing of waveguide structures most commonly uses ultraviolet (UV) laser wavelengths, however some materials do possess a photosensitivity to longer wavelengths, such as Argon ion laser lines around 488 nm. In some extraordinary cases such as in some polymers and chalcogenide glasses, which have strong photo-darkening responses, waveguides can also be written using low powers at a helium-neon wavelength of 633 nm. The efficacy of such waveguides is debatable considering the guided light itself is likely to cause further modification to the material. UV laser writing has become a widespread technique for directly writing high quality waveguides in a range of materials. Typically the required materials have to possess some photosensitivity in order for the refractive index to be modified, however some common glasses and polymers are suitable for UV waveguide inscription. Pure fused silica exhibits densification and a subsequent refractive index increase under UV irradiation, however the presence of germanium significantly increases the photosensitivity. The induced index changes are typically of the order of $\Delta n \approx 10^{-3} \rightarrow 10^{-2}$, and the technique is capable of producing low loss waveguides [12].

More recently, with the advent of robust, reliable ultrashort pulsed laser sources such as the Ti:Sapphire laser, ultrafast laser inscription (ULI) has surfaced as an extremely versatile technique for micro-modification of a wide range of transparent materials. The high peak powers attainable using ultrashort pulses enable extreme intensities to be achieved when such pulses are focussed. This allows nonlinear absorption processes to occur, the direct result of which is that the modification takes place only in the focal region. As the operating wavelength of these laser sources is typically in the near infrared, a vast array of substrate materials are transparent to the laser wavelength allowing three-dimensional micro-modification of small volumes.

Due to the extreme intensities achieved in the focal region, laser-induced optical breakdown allows modification to occur in any transparent medium. Dependant on the parameters used, this modification can be manifested in the form of a local refractive index change, or at higher powers the formation of nanostructures or voids. Figure 1-5 shows a schematic diagram of the ultrafast laser inscription of a waveguide device. The sample is mounted on a set of high accuracy three-dimensional translation stages on which the sample is moved in three dimensions through the focus of the ultrafast pulse train.

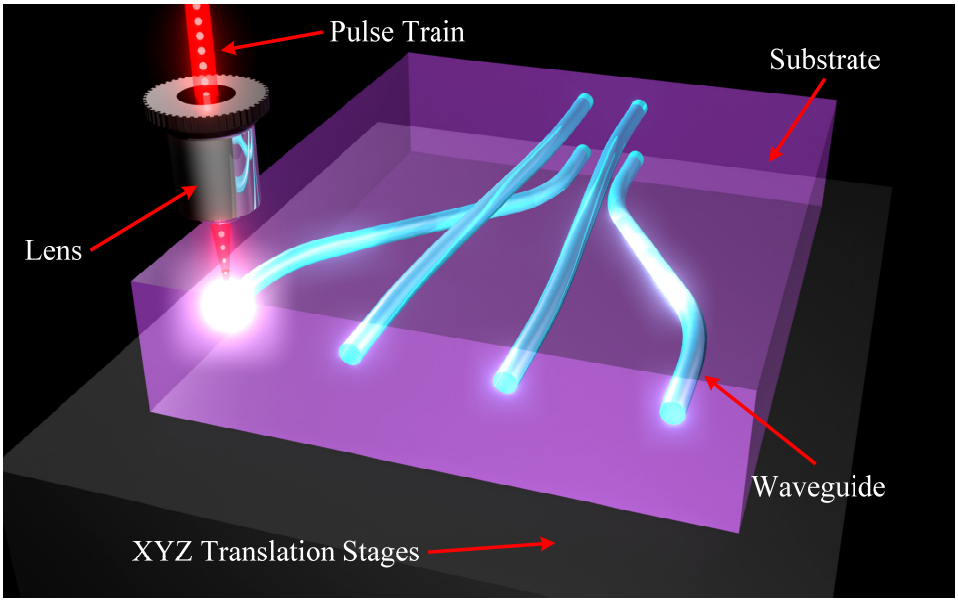

Figure 1-5. Schematic diagram of ultrafast laser waveguide inscription

The wide material flexibility, rapid fabrication and three dimensional capability makes ULI an ideal fabrication technology for a new generation of integrated optical devices. As the material modification occurs *inside* the substrate, clean room facilities are not required, reducing the required cost of running such a fabrication facility.

1.4 THESIS OUTLINE

The work presented in this thesis comprises the application of ultrafast laser inscription to the fabrication of waveguide devices in three optical material categories. The first material category investigated is an erbium-doped oxyfluoride silicate glass, with applications as an optical gain medium and laser gain material. The second material category is a novel bismuth-doped glass, with applications in ultra-broadband optical amplification and as a laser gain material. The final material category is a highly nonlinear germanium-sulphide based chalcogenide glass for applications in mid-infrared sensing, all-optical signal processing and spectral conversion.

Chapter two gives a background introduction to the field of ultrafast laser inscription. Fundamental waveguide theory is discussed, along with the interaction of ultrashort pulses in transparent materials, and the resulting material modification. The development of the field of ultrafast laser inscription is described, and the applications of the technology are outlined.

Chapter three presents a study of waveguide fabrication inside a novel erbium doped oxyfluoride silicate glass. An investigation of the optimal waveguide fabrication parameters is presented, along with an investigation of the gain properties for varying dopant concentrations. A waveguide laser is constructed, showing textbook threshold characteristics.

Chapter four presents a study of waveguide fabrication in a novel bismuth-doped glass, which offers ultra-broadband gain in the 1.3 μm spectral region. An investigation of the waveguide fabrication parameters is presented, along with an investigation of the active properties of the substrate material. Ultra-broadband fluorescence and gain are shown from the waveguides, indicating the potential for Bi-doped waveguide devices.

Chapter five presents a study of waveguide fabrication in a highly nonlinear germanium sulphide based chalcogenide glass for integrated nonlinear optical applications. Morphological studies of the fabricated structures are presented, offering insight into the waveguide formation mechanisms. Supercontinuum

generation experiments are carried out, demonstrating the nonlinear behaviour of the waveguides.

Finally, chapter six concludes the work presented in the thesis and discusses future work to be carried out as a result of the investigations.

CHAPTER 2 – REVIEW OF ULTRAFAST LASER INSCRIPTION

As this body of work provides an investigation of waveguide fabrication in a range of novel materials, it is important to understand the fundamental behaviour of light when it is confined to a waveguiding structure. This chapter begins by giving an overview of the origin of waveguiding.

2.1 THE ORIGIN OF GUIDED MODES

In order to describe the behaviour of electromagnetic waves inside waveguiding dielectric structures, we must first turn to Maxwell's equations in a non-magnetic, non-conducting medium. These are given by:

$$\nabla.\vec{D} = 0 \tag{2-1}$$

$$\nabla.\vec{B} = 0 \tag{2-2}$$

$$\nabla \times \vec{E} = -\frac{\partial \vec{B}}{\partial t} \tag{2-3}$$

$$\nabla \times \vec{H} = \frac{\partial \vec{D}}{\partial t} \tag{2-4}$$

where $\vec{D}$ is the electric displacement field, $\vec{B}$ is the magnetic field vector, $\vec{E}$ is the electric field vector, and $\vec{H}$ is the magnetising field vector. Assuming linear propagation, where $\vec{P}$ the polarisation field vector contains only linear terms:

$$\vec{P} = \varepsilon_0 \chi_e \vec{E} = \varepsilon_0(\varepsilon_r - 1)\vec{E} = \varepsilon\vec{E} - \varepsilon_0\vec{E} \tag{2-5}$$

where χ_0 is the electric susceptibility, ε_0 is the vacuum permittivity, ε_r is the relative permittivity and ε is the total electric permittivity. The electric displacement field then becomes:

$$\vec{D} = \varepsilon_0\vec{E} + \vec{P} = \varepsilon\vec{E} \tag{2-6}$$

and the magnetic field vector becomes:

$$\vec{B} = \mu_0\vec{H} \tag{2-7}$$

Taking the curl of equation 2-3, and substituting equations 2-4 and 2-6:

$$\nabla \times \left(\nabla \times \vec{E}\right) = -\mu_0 \frac{\partial}{\partial t}\left(\nabla \times \vec{H}\right) = -\mu_0 \frac{\partial^2 \vec{D}}{\partial t^2} = -\mu_0 \varepsilon \frac{\partial^2 \vec{E}}{\partial t^2} \qquad 2\text{-}8$$

Applying the well known vector identity:

$$\nabla \times \left(\nabla \times \vec{E}\right) = \nabla.\left(\nabla.\vec{E}\right) - \nabla^2 \vec{E} = -\nabla^2 \vec{E} \qquad 2\text{-}9$$

Given $\varepsilon = \varepsilon_0 n^2$ and $\varepsilon_0 \mu_0 = \frac{1}{c^2}$, combining equations 2-8 and 2-9 and allows us to arrive at the well known scalar wave equation:

$$\nabla^2 E - \frac{n^2}{c^2}\frac{\partial^2 E}{\partial t^2} = 0 \qquad 2\text{-}10$$

When this wave equation is subject to boundary conditions of the continuity of the electric field E and its derivative $\nabla.\mathrm{E}$ at the interface between the core and cladding of a waveguide, the allowed solutions to the wave equation form discrete modes. Within the core region, these modes are of the form:

$$E_j(x, y, z, t) = e_j(x, y) exp\left(i\beta_j z - i\omega t\right) \qquad 2\text{-}11$$

Where $e_j(x, y)$ is the spatial distribution of the electric field of the j^{th} mode. Outside the core region, the solution to the wave equation is a decaying exponential. The modal fields depend on all of the physical parameters defining the waveguide structure such as the refractive index contrast and the cross sectional geometry. Typically, the solutions are obtained using numerical techniques, as the form of the solutions cannot be achieved analytically except for in the case of very simple structures.

The mode field size and number of allowed guided modes depends on both the size of the waveguide, and the refractive index contrast between core and cladding. The size and spatial distribution of the electric field of a mode directly impacts the coupling loss attained when butt-coupling into a waveguide from an external source. It is therefore insightful to study the effect of the change of the mode size as the size and refractive index contrast are varied.

In order to demonstrate the dependence of the fundamental mode-field size on the waveguide diameter and refractive index change, square-core cross-section structures were modelled using the COMSOL Multiphysics Optics and Photonics

module. This is a commercial finite-element modelling package that calculates the allowed guided modes and subsequent mode profile for a given structure.

Figure 2-1 shows a plot of mode field diameter (MFD) of the fundamental mode *vs* waveguide diameter for several different refractive index changes. The MFD is defined as the width at which the intensity reaches a value of $\frac{1}{e^2}$ relative to the peak. The cladding refractive index was set to 1.5 and the wavelength was set to 1.55 μm.

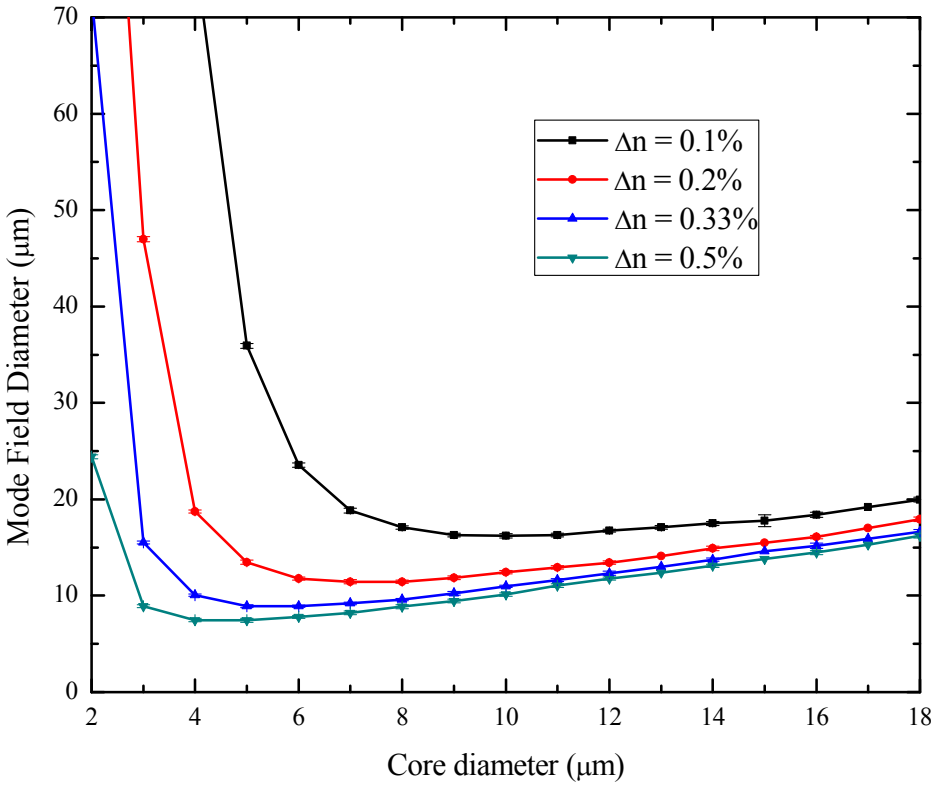

Figure 2-1. Graph showing fundamental MFD *vs* core diameter for a square core cross-section waveguide.

From Figure 2-1 it can be seen that as the core size is reduced, the mode size also reduces down to a minimum value. As the size is further reduced, the MFD then rises dramatically as the mode is no longer well confined with large amounts of the mode propagating in the cladding. As the refractive index contrast is increased, the minimum MFD becomes smaller allowing tighter confinement. Tailoring the size of the guided mode through control of the refractive index

change and core diameter enables the optimisation of coupling losses to optical fibres or other waveguides.

The fractional amount of coupling when direct butting between a single mode fibre and a single mode waveguide can be defined by the overlap integral as defined in equation 2-12.

$$\eta = \frac{\left(\int \overrightarrow{e_g}\overrightarrow{e_f}^{*}\, dxdy\right)^2}{\int \overrightarrow{e_g}\overrightarrow{e_g}^{*}\, dxdy \int \overrightarrow{e_f}\overrightarrow{e_f}^{*}\, dxdy} \qquad 2\text{-}12$$

where $\vec{e} = \vec{e}(x, y)$ is the electric field distribution of the guided mode, *"g"* stands for guide and *"f"* for fibre. If symmetrical Gaussian profiles are assumed with a waist w_0 equal to half the mode field diameter (MFD), the following simple formula for the fractional amount of coupling can be used:

$$\eta = \frac{4{w_{0f}}^2 {w_{0g}}^2}{\left({w_{0f}}^2 + {w_{0g}}^2\right)^2} \qquad 2\text{-}13$$

The coupling loss in decibels can then be defined as:

$$\eta[dB] = 10 \log_{10} \eta \qquad 2\text{-}14$$

Using equations 2-13 and 2-14, a useful estimate of the ideal coupling loss between fibre and waveguide can be achieved for single-mode structures when no Fresnel reflections are present.

In order to be able to fabricate waveguide devices, an understanding of the waveguide formation mechanism is highly desirable. The following sections describe the physical processes occurring during ultrafast laser inscription and the origins of the resultant refractive index changes. It is therefore important to first define the behaviour of ultrashort laser pulses inside dielectric materials.

2.2 ULTRASHORT PULSES IN DIELECTRIC MATERIALS

The propagation of an ultrashort laser pulse in a dielectric material exhibits significantly different behaviour to that observed during constant wave illumination. The nonlinear properties of the substrate play a large role in defining the material response to the incident radiation, due to the high peak powers attained by the laser pulses. This can be manifested as a whole range of nonlinear effects, causing modification to the laser spectrum through processes such as self-phase modulation (SPM) and four wave mixing (FWM), or through strong nonlinear propagation effects that distort the spatial or temporal profile of the laser beam.

One particularly important process is that of self-focussing. This arises as a result of the intensity dependence of the nonlinear refractive index as shown in equation 2-15.

$$n = n_0 + n_2 I \qquad 2\text{-}15$$

where I is the light intensity, n_0 is the linear refractive index and n_2 is the nonlinear refractive index, arising due to the $\chi^{(3)}$ component of the material polarisation. In most materials the sign of the n_2 response is positive, which leads to the higher intensity at the centre of a Gaussian beam to generate a higher refractive index than the edges of the beam. This forms a positive lens that causes the beam to self-focus inside the medium.

As the laser power is increased, the self-focusing effect becomes more pronounced until a critical power is reached whereby the self-focusing effect balances diffraction, forming a filament [13]. Equation 2-16 gives the critical power P_{cr} for filamentation.

$$P_{cr} = \frac{3.77\lambda^2}{8\pi n_0 n_2} \qquad 2\text{-}16$$

Above this critical power, the self-focusing is strong enough to cause a catastrophic collapse of the beam to the point where the intensity is high enough to cause nonlinear ionisation, generating a free electron plasma.

The energy deposition process through nonlinear ionisation is crucial to gaining an understanding of the fundamental mechanisms that occur during ultrafast laser inscription. The following section reviews these processes.

2.2.1 Energy absorption mechanisms

In a transparent material, the laser used to modify the material possesses a photon energy that is too small to directly excite an electron from the valence band to the conduction band. This means a nonlinear mechanism is necessary to achieve breakdown and energy deposition. Laser-induced breakdown (LIB) is a process whereby a normally transparent material is transformed into a highly absorbing plasma by an intense laser pulse. This forms the basis for energy deposition and material modification when ultrashort pulses interact with transparent materials.

LIB in transparent materials has been studied extensively since the invention of the laser, and fundamentally relies on photo-ionisation and avalanche ionisation. Photo-ionisation consists of two fundamental processes – multiphoton ionisation (MPI) and tunnelling ionisation (TI). MPI takes place when an electron simultaneously absorbs multiple photons in order to fully liberate itself from the bound state. TI occurs when the extreme electric field of the laser pulse is enough to approach the coulomb potential of the atom, allowing the electron to tunnel out of the bound state. The initial theoretical treatise for describing these processes was first developed by Keldysh in 1964 [14]. Keldysh formulated a model for describing the processes, resulting in a parameter which defines the dominant mechanism, known as the Keldysh parameter as shown in equation 2-17.

$$\gamma = \frac{\omega}{e}\sqrt{\frac{mcn\varepsilon_0 E_g}{I}} \qquad 2\text{-}17$$

Where ω is the laser frequency, I is the laser intensity, n is the refractive index, E_g is the band-gap of the material, c is the speed of light, ε_0 is the permittivity of free space and m and e are the reduced electron mass and charge. When the Keldysh parameter $\gamma > 1.5$ the dominant photo-ionisation process is MPI, when $\gamma < 1.5$ the dominant photo-ionisation process is TI. When the parameter is in

the region of $\gamma = 1.5$ the mechanism is an equal mixture of both MPI and TI [13]. Keldysh also described how the two processes can be dealt with in the same framework, however the physical origin of the processes is considerably different. Figure 2-2 shows a schematic diagram of the two photo-ionisation processes.

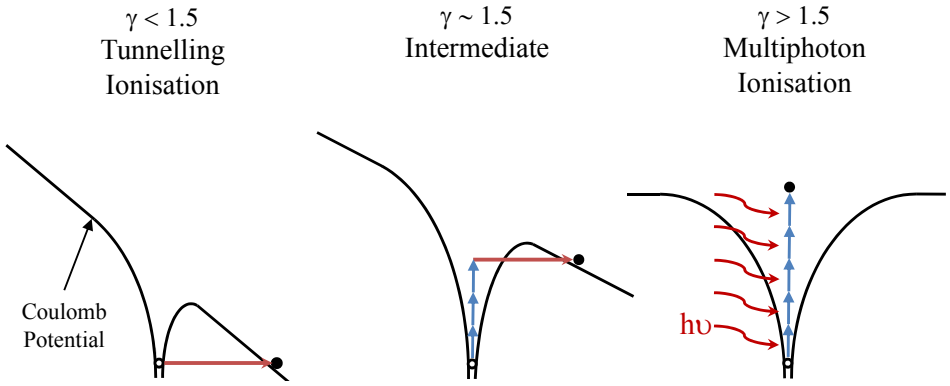

Figure 2-2. Photo-ionisation mechanisms and corresponding Keldysh parameter, showing processes of liberating an electron from the Coulomb potential [13].

Avalanche ionisation is an important mechanism for increasing the density of free electron plasmas during LIB. The mechanism was studied extensively by Bloembergen, utilising a pulsed CO_2 laser in order to remove the contribution from MPI. This is because the photon energy at 10.6 μm would require approximately 100 combined photons to liberate an electron [15]. The avalanche process relies on a 'seed' free electron present in the material. Normally a free electron oscillating in response to the laser field would not gain kinetic energy over an optical cycle. However, when it collides with the bound electrons and lattice, the free electron can absorb laser energy due to the Joule heating process, also known as inverse Bremsstrahlung [16]. Once the free electron can be accelerated enough so that its kinetic energy is greater than the ionisation potential of a bound electron, an impact with a bound electron can fully liberate it. The net result is two free electrons of low kinetic energy. This impact ionisation process quickly grows exponentially as more free electrons are generated.

For long pulses (>20 ps), the seed electrons for the avalanche process are supplied by thermally excited carriers, impurities or defect states present within the material. The initial free electron density present in the material can be

particularly low, such that large statistical variations occur in the number of free electrons present within the focal volume. This leads the LIB threshold to vary non-deterministically from area to area [16]. The behaviour of the LIB threshold for long pulses, although statistically fluctuating, generally follows as the square root of the pulse length. Several studies have investigated this dependence for ultrashort pulses, and this has been the subject of considerable debate.

The first pulse-length dependence study of LIB for ultrashort pulses was carried out in fused silica by Du *et al.* in 1994, using an amplified Ti:Sapphire laser system allowing variable output pulse lengths from 150 fs to 7 ns [17]. Deviation from the square root dependence was observed for pulse lengths below approximately 10 ps, with an increase in the damage threshold noted for sub-picosecond pulses. The large statistical variations in the LIB threshold disappeared, highlighting the key difference between long and short pulse LIB. Ultrashort pulses possess very high laser field strengths, such that nonlinear photo-ionisation can provide the seed electrons for the avalanche process. This does not rely on a random distribution of free electrons within the material, and so the statistical variation in the threshold behaviour disappears.

A subsequent study by Stuart *et al.* in 1995 also demonstrated a deviation from the square root dependence, however the LIB threshold was shown not to increase for ultrashort pulses [18]. Distinct morphological changes were also observed between the long and short pulse regime, which is further observed in the LIB threshold measurements. A model based around MPI seeded avalanche ionisation was suggested that agreed well with the experimental data. This model was expanded in a further study, along with an investigation of damage thresholds in optical coatings and fluorides [19, 20]. The model suggested that for extremely short pulses below 30 fs, MPI alone is capable of generating the critical plasma density for LIB.

A further study by Du *et al.* in 1996 studied LIB thresholds at 55 fs and 100 fs, using both linear and circular polarisations [21]. The authors suggest that the deviation from the square root dependence coupled with the polarisation insensitivity of the breakdown threshold indicates that the collision ionisation

taking place during the avalanche process suppresses the contribution from MPI. This would indicate that avalanche ionisation takes a dominant role, even for sub-100 fs pulses.

The debate was further progressed by Lenzner *et al.* in 1998, performing LIB threshold measurements for a much broader range of pulse lengths, extending down to 5 fs [22]. The measurements were also carried out in both fused silica and in a borosilicate glass. The authors found MPI rates several orders of magnitude lower than the predicted values under Keldysh theory, possibly due to a suppressant effect of avalanche ionisation. This also implicates tunnelling ionisation as an important process for very short pulses. Importantly the authors note a dramatic difference between fused silica and borosilicate glass, indicating that in fused silica the ionisation process is dominated by avalanche down to the 10 fs regime, whereas in borosilicate MPI dominates for pulse lengths below 100 fs due to the much smaller bandgap.

Modelling work carried out by Kaiser *et al.* in 2000, looked at ionisation processes assuming no defects [23]. The model contradicts evidence supplied in previous studies, suggesting that the avalanche mechanism is not significant for pulse lengths below 100 fs in fused silica due to the time required for the avalanche process to build up.

An important study by Schaffer *et al.* in 2001 studied ultrashort pulse LIB in bulk materials [13]. This is in stark contrast to the studies highlighted previously which looked at surface breakdown thresholds. Bulk measurements had been previously been avoided with ultrashort pulses due to the issues of self-focusing, dispersion and self phase modulation. Measurements were carried out at both 800 nm and 400 nm in several materials with different bandgaps. As with the study by Lenzner *et al.*, MPI rates were significantly lower than predicted by Keldysh. The authors suggest that tunnelling ionisation is important, particularly for wide bandgap materials and longer wavelengths.

Another interesting mechanism recently described is that of ‘multi-photon forest fires’ shown by Gaier *et al.* in 2004 [24]. This mechanism is particularly

applicable to very short pulses where the traditional avalanche process has no time to develop. The process stems from the effect of 'enhanced ionisation' when an electron is rapidly removed from an atom. Due to the presence of the uncompensated hole that is left behind, the ionisation potential in the local region around the hole is dramatically reduced, allowing the exponential creation of new holes. These nano-plasmas ignite in an avalanche-like process. The authors also suggest that the growth of the plasmas could also be facilitated by the excitation of surface plasmons leading to large enhancements of the local field, aiding TI.

More recently in 2005, Rayner *et al.* introduced the important concept of energy depletion of focused ultrashort pulses [25]. Self-limiting of the absorption process is observed due to the depletion of photons at the centre of the focussed beam. The mechanism is described in Figure 2-3. The authors state that self-focussing is overwhelmed by the energy depletion effect; however it is suggested that for larger F# beams, self-focusing will play a role.

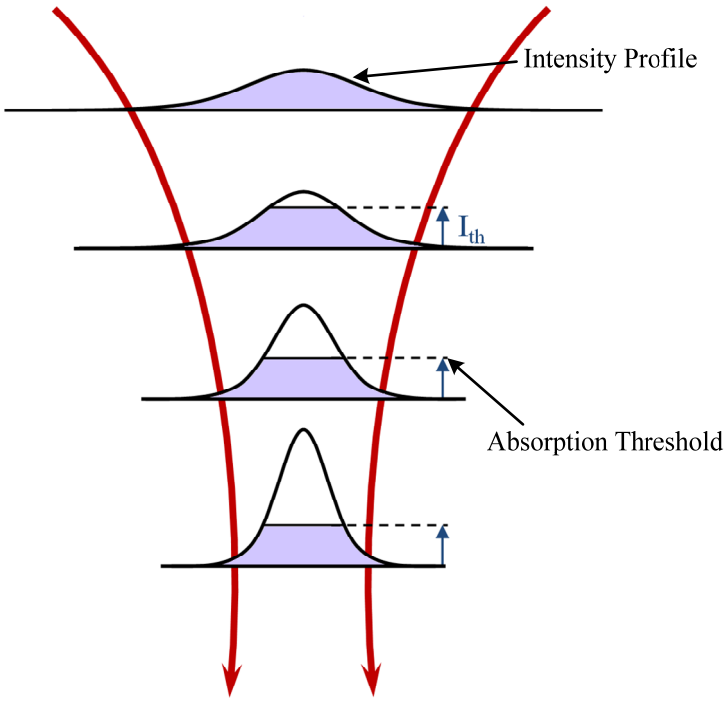

Figure 2-3. Diagram showing energy depletion as the pulse is focussed. Intensities above the nonlinear absorption threshold I_{th} are quickly absorbed, causing a capping to the peak intensity of the pulse and subsequent energy deposition before the focus [25].

The ionisation mechanisms discussed so far supply the energy required to generate material modification, however the nature of the induced modification depends dramatically on the processing parameters and material characteristics. The following section discusses the nature of the material modification created by the interaction of ultrashort laser pulses in dielectric materials.

2.2.2 Material modification from ultrashort pulses

So far the discussion of the interaction of ultrashort pulses with dielectrics has concentrated on plasma generation. However, the manner in which the plasma transfers energy to the surrounding material dramatically affects the resulting material modification once thermal relaxation has taken place.

Once the plasma grows to reach a critical density, the plasma frequency approaches the laser oscillation frequency. This then results in highly efficient absorption of the laser energy as the previously transparent plasma becomes opaque [16]. The electrons then transfer energy to the ions and lattice, heating the material. The absorbed energy leaves the laser focal volume by conduction due to the steep thermal gradient.

For long pulses, energy transfer during the laser-matter interaction is very efficient, with the long interaction time allowing the electrons and ions to be in equilibrium. The long timescales allow heat to diffuse significantly, generating a large heat affected zone. For ultrashort pulses, the small interaction time results in the electrons being driven to very high temperatures, with the ions and lattice remaining much colder. The optical excitation ends before the lattice is perturbed. This results in the electron to ion energy transfer mostly taking place after the laser pulse has disappeared, allowing the ions to be elevated to much higher temperatures than for long pulses [16]. The timescale for energy transfer from electrons to the ions and lattice is of the order of several picoseconds [26].

The localised energy heats the bulk material very quickly past the liquid phase into the vapour phase with high average kinetic energy. At pulse energies much greater than the damage threshold, this generates an explosive expansion through

coulomb repulsion leading to optical damage and void creation. This is often accompanied by densification and large changes to the optical properties due to the presence of voids. This was studied by Glezer *et al.* [26, 27], showing micro-explosions and void creation inside fused silica using 100 fs pulses. The explosions produced densified areas around the void structures which were approximately 200-250 nm in diameter. Self-focussing was attributed to the generation of such small structures. The study of void creation has been furthered by Sundaram *et al.* in tellurite glasses [28], and Toratani *et al.* showing self-organised voids in fused silica [29].

The explosive expansion and subsequent ablation of materials using high energy ultrashort pulses has been applied extensively to micromachining, where the much reduced heat-affected zone and deterministic behaviour allows machining with repeatability and great precision [16, 30, 31]. With high pulse energies, the voids or damage structures created are often accompanied by refractive index changes around the structure. These refractive index changes are generally due to stress and compressive densification around a damaged structure. However, when the pulse energy is reduced, the plasma is not energetic enough to produce an explosive expansion resulting in ablation. Refractive index changes are still observed, however the mechanism for this is less clear and has been the subject of considerable debate.

The discovery of refractive index changes when focussing ultrashort pulses inside dielectric materials by Davis *et al.* in 1996 was simultaneously exploited by the authors to show that waveguides could be produced by translating the material through the focus [32]. The origin for the refractive index changes was not explained, although the presence of colour centres was observed. Colour centres are known to cause local refractive index changes through the Kramers-Kronig mechanism. Since then, several studies have investigated the mechanisms for refractive index changes.

Schaffer *et al.* demonstrated refractive index changes using an unamplified high-repetition rate oscillator in 2001 [33]. The structural changes observed appeared to be thermal in nature, suggesting non-uniform resolidification leaves a greater

density at the centre of the modified region. A study of the modification in fused silica and borosilicate glass was carried out by Streltsov *et al.* in 2002 [34]. The authors were unable to determine the precise nature of the refractive index change, however colour centres were suggested to be responsible for a substantial contribution. The colour centres annealed out at elevated temperatures, however some refractive index change persisted. No evidence of densification could be observed.

This is in stark contrast to a subsequent study by Chan *et al.* in 2001. Raman microscopy revealed an increase in 3 and 4-member Si-O ring structures, evidence of an increase in bond-angles and subsequent densification. Fused silica is well known to be able to exhibit a dense phase typically achieved at high temperatures and pressures. The shockwave propagation from the rapid energy transfer was suggested as a mechanism for creating the densified phase. Colour centres were also present in the form of non-bridging oxygen hole centres (NBOHCs), a mechanism well known from UV/X-ray irradiation of fused silica.

These results support a mechanism of thermally induced changes whereby the rapid resolidification dynamics lead to left over density changes. This process is also known as 'fictive temperature', as fused silica is known to have its maximum density at 1800 K [35]. The generation of colour centres helps to modify the refractive index further. Schaffer *et al.* showed in 2003 that the use of a high repetition rate system allows heat build up from successive pulses to cumulate when the inter-pulse time is shorter than the heat diffusion time [36]. This generates modification which fits into the thermally induced densification framework as described above. This mechanism however does not explain the refractive index changes in many other cases.

Birefringent modification was first observed by Sudrie *et al.* in 2001, where a sharp threshold was observed for the onset of production of such structures in fused silica [37]. The explanation of such modification was first suggested by Shimotsuma *et al.* in 2003 with the formation of periodic nanograting structures [38], and further studied in 2004 by Bricchi *et al.* detecting form birefringence and negative refractive index changes [39]. These periodic nano-scale structures

are produced in an intermediate pulse energy regime, below the energy required to generate explosive ablation, and above the energy required to generate simply a refractive index change. The origin of the structures was suggested to be caused by the interference between the light field and the electric field of the bulk electron plasma wave. An alternative explanation for the formation of nanograting structures was suggested by Rajeev *et al.* in 2007 [40]. Local field enhancement around the microplasma, along with excitation and interference of surface plasmon-polaritons present in the photo-ionised material was suggested as the mechanism.

Nanogratings do not occur in all substrate materials, indeed only a handful possess the ability to generate such structures. This serves to highlight the wide range of material properties and processing parameters that affect the mechanism for material modification. Each of these possible mechanisms may or may not occur in a particular parameter set in a particular material.

Several studies have attempted to probe the ultrashort pulse laser-matter interaction and subsequent modification processes. One technique that has been pursued by Sakakura *et al.* is that of the transient lens technique [41-44]. This is a pump-probe based method for monitoring the spatially inhomogeneous laser-induced RI change. The pump pulse creates an RI distribution which causes the spatial distribution of the probe beam to be modified. As the time delay between the pump and probe pulses can be varied, snapshots of the RI distribution can be observed as the process evolves. Clear evidence of an expanding pressure wave was observed, with rapid oscillations of the refractive index occurring over a timescale of approximately 2 ns. This was attributed to the relaxation of thermo-elastic stress.

A paper by Cho *et al.* in 2002 performed pump probe transmission measurements to study the dynamics of plasma formation and bulk refractive index modification [45]. This was achieved by measuring the energy variation of the probe beam through the plasma. The authors noted significant differences between the plasma dynamics of RI modification and bulk damage. For RI modification, the plasma

decay time was considerably shorter at 15 ps, as opposed to the 35 ps for optical damage.

A more recent study by Gawelda *et al.* in 2008 utilised pump-probe microscopy to image the transient properties of the ultrafast light-matter interaction, created when focussing 130 fs pulses into phosphate glass [46]. Both transient transmission microscopy and plasma emission imaging was performed under different pump pulse lengths and polarisations. Filamentation was clearly observed, and was shown to occur more easily for shorter pulse lengths and for linear polarisation. The use of circular polarisation reduces the onset of filamentation and improves the spatial distribution of the transient plasma.

Overall, a wide range of mechanisms for below-damage material modification exist, and which of these processes occurs depends on the material composition and laser processing parameters. A comprehensive model of material modification that would be able to predict the nature and dynamics of bulk material modification does not yet exist. Nevertheless the ULI process has been proven to be a flexible, useful technique for producing integrated optical devices. The following section reviews the progress in applying ultrafast laser inscription to the fabrication of waveguides and various integrated optical devices.

2.2.3 Photonic applications of ultrafast laser inscription

The discovery of refractive index modification using ultrafast lasers by Davis *et al.*, was immediately exploited to fabricate waveguides simply by translating the substrate material through the focus of the beam [32]. Subsequent studies following Davis' seminal work extended the range of materials and parameter space investigated. Waveguide fabrication was shown by the same research group in fused silica, Ge-doped silica, borosilicate, borate, phosphate, fluorophosphates, fluorides and chalcogenide glasses [47, 48].

Due to the wide range of index modification effects and vast range of useful material compositions, the optimisation process for finding optimal waveguide parameters has to assume a trial and error approach. Initially, waveguide

fabrication was carried out either using amplified Ti:Sapphire laser systems, typically emitting pulse trains in the 1-200 kHz repetition rate range, or using unamplified oscillators with repetition rates of many MHz [33].

Waveguides can be written using two directional geometries – transverse and longitudinal. This is shown and described in Figure 2-4 below.

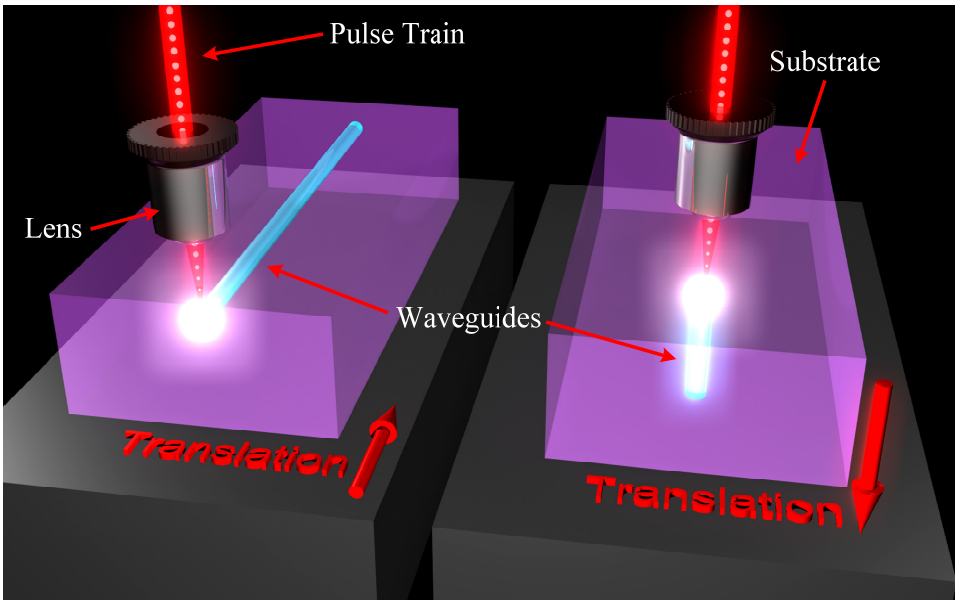

Figure 2-4. Schematic diagram of waveguide fabrication geometry. Transverse geometry is shown on the left, where the sample is translated perpendicular to the laser axis. Longitudinal geometry is shown on the right where the sample is translated parallel to the laser axis.

Waveguides fabricated using low repetition rate lasers have a RI modification profile that closely resembles the distribution of the laser intensity at the focus. For longitudinal waveguide fabrication this is not an issue as the shape of the waveguide cross-section follows that of the circular beam profile; however for transverse fabrication the cross section of the RI distribution is dependent on both the confocal parameter and beam waist. As the confocal parameter is generally considerably larger than the focussed beam waist, this leads to a cross-section that is highly asymmetrical. This produces an asymmetrical mode profile that causes excess coupling losses to symmetrical mode profiles of other components such as

single mode fibres. This issue can be addressed by using waveguide shaping techniques.

The task of waveguide shaping was first achieved by Cerullo *et al.* in 2004, using a cylindrical telescope to alter the symmetry of the beam before the objective lens [49]. Reducing the beam diameter in the axis perpendicular to the waveguide fabrication direction reduces the effective numerical aperture (NA) in that axis, increasing the focused spot size. With appropriate tuning of the ellipticity of the beam entering the objective lens, a symmetric waveguide can be fabricated.

Another similar technique was implemented by Ams *et al.* in 2005, whereby a slit is placed in front of the focussing lens [50]. This has the same effect of shaping the beam entering the focussing objective, however a considerable amount of power is lost due to aperturing by the slit. This configuration benefits from its inherent simplicity, with appropriate tuning of the slit width adjusting the asymmetry of the fabricated waveguide.

Waveguide shaping can also be achieved using a multi-scan approach [51, 52]. Using the multi-scan technique, the desired waveguide cross section is built up from many successive passes, each pass having an incremental translation with respect to the last. This allows effectively arbitrary cross sections to be built up, and removes the dependence of the modified cross-section on the intensity distribution in the focal region. This flexible technique has the penalty of an increase in the fabrication times, as the desired structure has to be built up from many scans. The multi-scan method is also useful for materials with a low damage threshold due to the reduced pulse energies required to generate the desired RI change.

More recently, Thomson *et al.* implemented a two-dimensional deformable mirror for beam shaping [53]. Using this technique, low coupling losses were achieved through controlling the phase profile of the beam entering the focussing optics. This technique offers great flexibility, and offers the prospect of controlling the waveguide cross-section during writing.

For situations whereby the repetition rate of the laser is such that the inter-pulse time is shorter than the thermal diffusion time, thermal accumulation can take place [36]. For most substrate materials this typically occurs at repetition rates around 1 MHz. In this regime, the waveguide cross-section is governed by thermal diffusion out of the focal region, producing a much more symmetric RI profile. Eaton *et al.* performed an extensive study of the effects of repetition rate in borosilicate glass [54]. The onset of thermal accumulation depends heavily on the thermal characteristics of the material, and also steers the modification mechanism closer to that of thermally induced changes such as the principle of fictive temperature. Repetition rates in the 0.1 to 2 MHz range generally allow flexible access to different fabrication regimes for a wide range of materials.

In general, there are many fabrication parameters available to tune which allow adjustments to be made to the guiding properties of the waveguides. These are pulse energy, pulse duration, pulse repetition rate, focusing NA, polarisation, translation speed, and in the case of multi-scan fabrication, number of scans and scan separation. Firstly, the laser parameters of pulse energy, pulse duration and repetition rate enable one to access different modification mechanisms such as thermal accumulation, ablation, or nanograting formation. The beam parameters, governed by the NA of the focussing optics allow the size of the modified region to be altered. The translation speed allows one to adjust the energy deposition per unit length, with the multi-scan variables (number of scans and scan separation) allowing fine control of the RI cross-section of the waveguide.

One interesting parameter that affects the inscription process is that of the direction of translation. In centrosymmetric materials this can be caused by pulse front tilt on the beam entering the objective as shown by Kazansky *et al.* in 2007 [55]. A directional effect has also been observed with no tilt in the pulse front by the same researchers in non-centrosymmetric media such as lithium niobate [56]. In this case the process is a new physical phenomenon occurring due to anisotropic heating of the crystal.

An early application of ultrafast laser inscription to producing a practical device was the fabrication of optical amplifiers by fabricating waveguides inside laser

gain media. This was first investigated by Sikorski *et al.* in 2000, with the fabrication of waveguides in a Nd-doped silicate glass [57]. This was extended to Er-doped gain media by Osellame *et al.* at the Politecnico di Milano [58, 59]. The same group later reported on laser action using fibre Bragg gratings (FBGs) either side of the waveguide to form a cavity [60]. In further work by the Milan group a different fabrication laser was employed, operating at a significantly higher repetition rate of 885 kHz than the 1 kHz used previously, resulting in a reduction of the waveguide losses. This allowed the achievement of net gain across the whole of the 'C' telecommunications band spanning 1530-1565 nm [61]. Recently, Raman gain has also been observed in a waveguide inscribed in a potassium-gadolinium-tungstate (KGW) crystal [62].

Waveguide lasers have also been achieved in Nd:YAG crystals. The first report of an Nd:YAG waveguide laser fabricated using ultrafast inscription was from Okhrimchuk *et al.* in 2005 [63]. The RI modification induced by the ultrafast inscription process was found to be negative, so the authors wrote a depressed cladding with the unmodified core region acting as the waveguide. A more recent paper by Torchia *et al.* used so called 'Type II' guiding whereby two damage lines are inscribed with a gap in between [64]. Due to the stress fields induced by the damage lines, the region in between acts as a waveguide. Using this technique, the authors were able to fabricate an efficient single transverse mode laser producing a slope efficiency of 60%.

More conventional passive devices have also been fabricated, with initial basic devices such as directional couplers and cross couplers being produced by Streltsov in 2000 [65] and later Minoshima in 2001 [66]. Both these papers were demonstrations that coupled-mode photonic devices could be fabricated using ultrafast laser inscription. Minoshima extended this work to the fabrication of an MZI in 2002 [67]. This work formed the basis for subsequent work by Florea *et al.* in 2003, showing an optical interleaver based upon an MZI [68]. Liu followed on in 2005 demonstrating a 1 to 4 and 1 to 8 coupler based on cascaded Y-splitters [51]. Extensive work on directional couplers was carried out by Eaton *et al.* in 2006 [69], showing low insertion losses and high coupling ratios up to 99%.

This was extended by the same research group with a paper by Chen *et al.* in 2008 showing broadband operation covering 400 nm [70].

The three-dimensional capability of ULI has also been exploited, initially in the fabrication of a 3D 1 to 3 splitter by Nolte *et al.* in 2003 [71]. A 3D microring resonator and 3D directional coupler were fabricated by Kowalevicz *et al.* in 2005 [72]. Remarkably, the micro-ring resonator was written vertically, with the input/output waveguides in the horizontal plane. Later, Osellame *et al.* showed coupled waveguides fabricated at several depth layers [73]. More recently, Thomson *et al.* demonstrated a 3D interconnect device, allowing efficient and convenient coupling between the cores of a multi-core fibre to a conventional fibre v-groove array [74]. Each of these demonstrations show the potential for ULI in producing novel devices that cannot be fabricated using conventional techniques.

The fabrication of Bragg-grating waveguides was first demonstrated by Marshall *et al.* in 2006 [75]. Initially, a waveguide was inscribed using the slit technique to create a symmetrical waveguide. The slit was then removed and the waveguide was written over at a much faster translation speed. Due to the low repetition rate of 1 kHz used for this fabrication, the fast write stage created a series of spaced modification regions, generating the periodic modulation required for a Bragg structure. This was extended by Zhang *et al.* to be fabricated in a single step, generating an array of RI modified voxels [76]. The method was further refined, allowing high strength Bragg-waveguides to be fabricated for a wide range of resonant wavelengths [77]. A more flexible technique, employing an acousto-optic modulator to create the periodic RI changes was first reported by Zhang *et al.* [78]. This allows a higher repetition rate fabrication laser to be employed, generating higher quality structures. The Bragg-waveguide inscription technique was recently used by Marshall *et al.* to create a monolithic distributed feedback laser in an Er:Yb doped phosphate glass [79] and more recently in a Yb-doped phosphate glass [80].

Various sensor devices have been fabricated using ULI. A simple vibration sensor was fabricated by Kamata *et al.* in 2005, employing a central waveguide

suspended on a beam that is free to move [81]. Any vibration causes excess loss in the system which can be detected by monitoring the amount of transmitted light. A more extensive waveguide sensor device was demonstrated by Zhang *et al.* in 2008 [82]. This device employed several Bragg-waveguides in different axes and at different depths to allow bend and temperature sensing.

In some materials, the irradiated material can have an etch-rate many times faster than the unmodified material. In fused silica, the nanograting formation process described earlier has the important practical side-effect of enhancing the selectivity of this process. The irradiated structure containing nanogratings has an etch rate up to 200 times greater than the unirradiated material. This allows the creation of microchannels and micro-optics using selective etching as demonstrated by Bellouard *et al.* in 2004 [83]. This was exploited to create a microfluidic sensing device by Osellame *et al.* in 2007, through the integration of waveguide and micro-channels [84]. A more complex device was fabricated by Bellouard *et al.*, demonstrating a micro opto-mechanical displacement sensor written entirely in fused silica utilising waveguides and selectively etched springs [85].

Waveguide fabrication has also been carried out in highly nonlinear materials. A considerable amount of research has been carried out into fabricating waveguides in lithium niobate, with applications in frequency conversion and modulation. The first demonstration of telecoms wavelength guiding was carried out by Thomson *et al.* in 2006 [86]. This has culminated in the demonstration of efficient second harmonic generation and the preservation of the nonlinear coefficient by Osellame *et al.* in 2007 [87]. Waveguides have also been fabricated in other nonlinear crystals such as KTP by Campbell *et al.* in 2007 [88].

Nonlinear glasses have also been utilised for waveguide fabrication. Chalcogenide glasses have been extensively studied due to their high third order nonlinearities and high levels of photosensitivity. Waveguides were fabricated in chalcogenide glasses in early ULI work by Miura *et al.* [47]. More recent work by Zoubir *et al.* has demonstrated high refractive index contrasts of up to $\Delta n \sim 10^{-2}$

in As_2S_3 films [89]. Waveguides have also been fabricated in bismuth borate glass by Yang *et al.*, showing low propagation losses of approximately 0.2 dB/cm [90].

Other applications of ULI exist, including high density data storage. This was explored early on in the development of ULI by Glezer *et al.* in 1996 [27]. A storage density of 17 $Gbcm^{-3}$ was achieved, however the practical use of such a system is debatable. This was extended to the creation of re-writable memory using photo-induced changes to the valence state of samarium ions by Miura in 2002 [91]. Bulk gratings have been fabricated using ULI by Florea *et al.* in 2003 [68], and more complicated optical components such as Fresnel lenses have been fabricated by Watanabe *et al.* in 2002 [92].

Overall the ULI process has been demonstrated to be a highly effective and versatile fabrication technology, capable of micro-modifying almost any material. Waveguide devices have been fabricated in a wide range of materials, however much is still left to investigate. The work contained in this thesis seeks to investigate the fabrication of waveguide devices in three distinct, novel substrate materials.

CHAPTER 3 – WAVEGUIDE INSCRIPTION IN OXYFLUORIDE SILICATE GLASS

3.1 INTRODUCTION

As a direct result of the development of the erbium-doped fibre amplifier in the late 1980s and early 1990s, long-haul optical fibre telecommunications has experienced a bandwidth explosion. The ability to exploit convenient semiconductor diode laser pump sources to amplify signals in the 1.5 μm spectral region, where optical fibres exhibit their lowest losses, whilst remaining in the optical domain, has enabled the exploitation of ever larger amounts of the inherent bandwidth available in fibre optical systems.

Currently, the push for greater bandwidth in shorter distance communications networks such as Metropolitan Area Networks (MANs) and Local Area Networks (LANs) will eventually shift these systems into using single-mode optical fibre and therefore require the associated components such as optical amplifiers. These shorter-distance network applications are arguably more cost-sensitive, so great interest exists in fabricating compact cost-effective optical amplifier solutions. The erbium-doped waveguide amplifier (EDWA) as a concept has emerged, offering the same capability as its optical fibre based cousin in a compact, low-cost format.

The work described in this chapter covers the investigation of waveguide fabrication inside Er-doped oxyfluoride silicate glass. All the substrate materials used for this work were designed and fabricated by Professor A. Jha and co-workers at the University of Leeds. The waveguide fabrication work was carried out over the course of several visits to the Politecnico di Milano under a collaborative research project funded by the European Union Centre for Ultrafast Science and Biomedical Optics (CUSBO).

Section 3.2.1 gives an introduction to rare-earth doped materials, followed by a specific discussion of Er-doped systems in Section 3.2.2. Section 3.2.3 introduces oxyfluoride silicate glass as a host for the erbium ion, followed by an overview of

previous work on ULI waveguides in Er-doped substrates in Section 3.2.4. Section 3.2.5 describes the laser system used for the work presented in this chapter. Section 3.3 covers the waveguide inscription and loss characterisation experiments carried out, followed by an extensive gain investigation in Section 3.4. Construction and characterisation of a waveguide laser formed using an ultrafast laser inscribed waveguide is presented in Section 3.5.

3.2 ERBIUM-DOPED GAIN MEDIA

3.2.1 Rare Earth Ions

Rare-earth (RE) doped gain media have been investigated extensively since the 1960s, offering convenient emission in the infrared and visible spectral regions. RE ions are also able to offer laser gain in a wide range of host materials, which has led to RE doped materials becoming the foundation for workhorse laser systems across the entire spectrum of laser applications.

In glass hosts, laser-gain capable RE ions exist in the trivalent state within the host material [93]. Trivalent RE ions possess an unusual electronic configuration that leads to the laser transitions occurring *within* the 4f electronic shell. The 4f shell is shielded from external fields by the outermost shells 5s and 5p, leading to a significantly reduced effect on the laser transitions from the host material. This is in contrast to transition metal doped systems such as Ti:Sapphire, where the laser transitions occur in the outer shell electrons, leading to a strong dependence on the host material, which is significant enough to inhibit laser gain action in all but a few substrate configurations. It is this shielding effect that allows RE ions to exist in gain-capable forms in such a wide range of substrate materials. Whilst relatively small, the weak perturbations induced by the substrate in RE-doped systems have important effects on the amplification behaviour [93].

3.2.2 Erbium doped glasses as gain media

At a fundamental level, a glass is an un-crystallised inorganic solid, possessing a well defined structure at short scales of a few atoms, but is completely random and aperiodic on a larger scale. When a RE ion is introduced into the substrate, the local electric field around the ion known as the crystalline electric field, or 'ligand field', couples to the electrons in the ion resulting in a lifting of the degeneracy of those energy levels. This mechanism, known as the Stark effect, is the electric analogue of the Zeeman effect, whereby energy levels are split in the presence of a magnetic field. The Ligand field varies locally from site to site, causing a random variation in the amount of Stark splitting across the substrate [93]. These random perturbations in the amount of Stark splitting cause spectral broadening to the emission lines of the RE ion, in a process known as *inhomogeneous broadening*. The broad nature of the emission lines of RE ions in glasses is particularly relevant for optical amplifier applications, where increased spectral bandwidth allows more signal wavelengths to be used in WDM systems, multiplying the available data bandwidth in a communications network.

In general, glasses offer a wide range of benefits with respect to crystals for optical amplification applications. Glasses are low cost, easily fabricated, have good optical properties such as low birefringence and can be chosen to have low nonlinearities, which can be detrimental to optical amplifier behaviour. Glasses however tend to have significantly lower stimulated emission cross-sections and have a lower ion quenching concentration [93].

The energy level diagram of Er-doped glass is shown in Figure 3-1. The primary laser gain transition route is using a 980 nm pump wavelength to excite the electrons from the ground state to the $^4I_{11/2}$ pump band as shown as transition 1. A rapid non-radiative decay then occurs due to multi-phonon relaxation to the top of the $^4I_{13/2}$ metastable band, shown as transition 2.

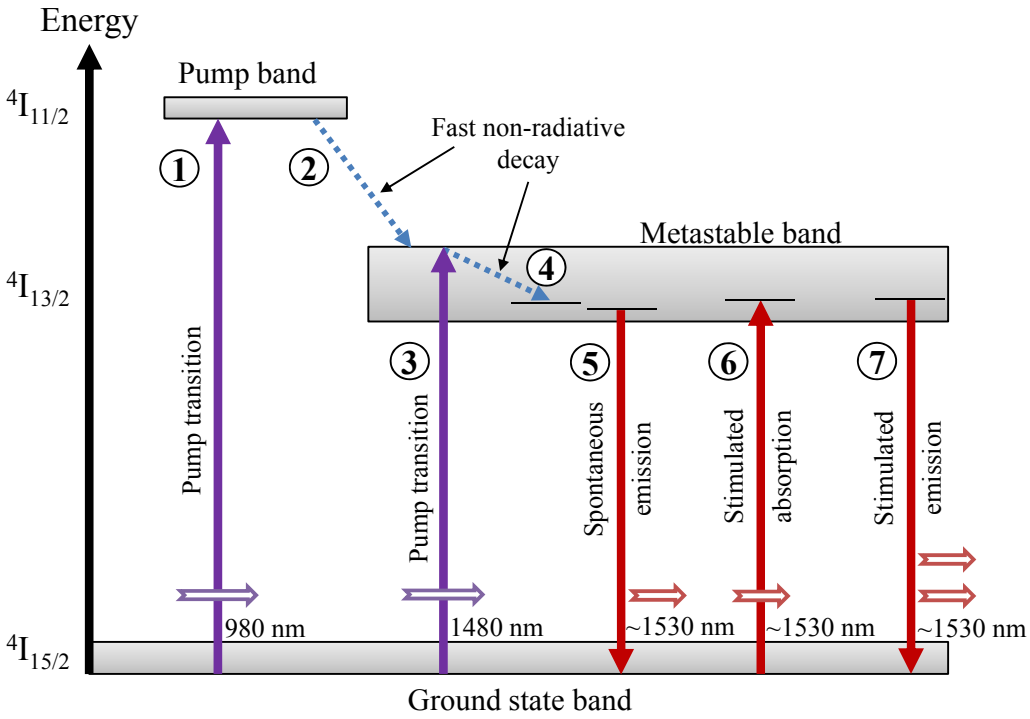

Figure 3-1. Energy level scheme of Erbium ions in a glass substrate [94].

The system can also be pumped as a quasi-two level system at 1480 nm, as shown as transition 3. This is due to a spectral shift in the absorption and emission cross-sections between the $^4I_{13/2}$ and $^4I_{15/2}$ bands, resulting in the absorption cross section being typically three times larger than the emission cross-section at 1480 nm. This allows optical pumping of the $^4I_{13/2}$ state but results in a reduced maximum population inversion of approximately 70%. The quantum defect is considerably lower than when pumping at 980 nm, so less energy is lost to phonons in the process, shown as transition 4.

Spontaneous emission, as shown as transition 5 in Figure 3-1, is the primary source of noise in an Er-doped amplifier. This fluorescence is typically amplified further by the stimulated emission process, to generated amplified spontaneous emission (ASE).

As erbium is a three or quasi-two level system, the stimulated absorption process at the signal wavelength takes place with or without the presence of optical pumping in the system. This Ground State Absorption (GSA), shown as

transition 6, needs to be overcome before any population inversion can be achieved. Any gain achieved above GSA is defined as *internal gain*.

The stimulated emission process that drives optical amplification is shown as transition 7 in Figure 3-1. Stimulated emission occurs when an electron in the metastable band is triggered to drop down to the ground state by a signal photon. As the triggered electron drops down to the ground state, it emits a duplicate of the signal photon, providing amplification.

Several parasitic processes can occur that reduce the amount of pump energy able to generate a population inversion in the metastable band. Excited state absorption (ESA) can take place when an electron in the pump band can absorb a further photon to a higher energy level which has a similar transition energy to the signal or pump photon energies [93]. This can result in nonradiative phonon mediated decay, or in upconversion processes such as the visible green emission as typically observed when Er-doped gain media are pumped. The efficiency of such processes depends on the lifetimes of the upper states, which is affected by the host material.

A major consideration for RE host materials is the ion solubility. At low dopant concentrations, the ions are evenly distributed throughout the glass matrix. The host material has a distribution of sites capable of hosting a RE ion. As the concentration is increased, the distribution can become uneven, resulting in the inter-ionic distance being short enough to enable ion-ion coupling and co-operative energy transfer (CET) [93].

CET can be beneficially exploited in the case of *sensitised luminescence*, whereby resonant cross-transfer of energy can take place between pairs of ions, such as between Er and Yb ions. This is typically used to improve the pump absorption in Er-doped systems, as the absorption cross-section of Yb is approximately 10 times that of Er at 980 nm [95].

The primary detrimental effect of CET is in the form of cross-relaxation. This occurs when neighbouring Er ions couple and energy transfer takes place. This can lead to cooperative frequency upconversion emission in a similar process to

ESA which takes energy away from the primary amplification process. At higher dopant concentrations, the ions form clusters with CET taking place between all ions in the cluster, rapidly decreasing the lifetime of the metastable band. The only way to prevent these occurrences is to limit the Er-doping concentration to low enough levels such that the inter-ionic distances are large [93].

The host material structure has a large effect on the ion solubility. Fused Silica as used in optical fibres is only capable of incorporating a low concentration of RE ions before clustering occurs, resulting in typical active fibre lengths of several meters in EDFAs. For EDWA applications, where the active gain region is of the order of several centimetres, much higher dopant concentrations are required. The introduction of network modifiers such as Al_2O_3 or P_2O_5 to silica based glass compositions allows an improvement in ion solubility by increasing the number of available sites for RE ions to occupy. Other host materials such as phosphates, fluorides and chalcogenides offer considerably higher RE ion solubility than silica based hosts, however such materials may have other detrimental properties, such as reduced physical stability or susceptibility to water absorption.

3.2.3 Erbium doped oxyfluoride silicate glass

Fluoride glasses, which are defined as glasses possessing metal fluorides as network formers have advantageous properties for amplification applications. Their low vibrational frequencies and corresponding low phonon energies reduce intrinsic losses in the infrared region. The low phonon energies also enhance fluorescence properties such as the lifetime of the metastable band, resulting in increased emission efficiency. Fluoride glasses also offer broader emission bands than silica glass, however suffer from fragility and are hydrophilic [96].

In an attempt to combine the beneficial properties of high ion solubility with structural and environmental stability, hybrid multi-component glasses offer one route to a compromise. Oxyfluoride silicate glass (OSG) is an example of such an approach. OSG has been shown to offer considerable performance advantages over other silica based glasses. A comparison of two figure-of-merit (FOM)

quantities is shown in Table 3-1 below [97]. The FOM for gain is defined as the product between the stimulated emission cross-section σ, and the lifetime of the metastable band τ. The FOM for gain bandwidth is defined as the product of the full-width-half-maximum (FWHM) of the gain bandwidth $\Delta\lambda$, and the stimulated emission cross-section σ.

Glass Type	FOM Gain $(\sigma\tau)\times10^{-21}$ cm^{2}ms	FOM Bandwidth $(\Delta\lambda\times\sigma)$ nm$\times10^{-1}$cm^2
Al Silica	57	134
Al/Ge Silica	59	145
Al/P Silica	58	238
OSG	95	283

Table 3-1. Comparison of two figure-of-merits for host gain performance. OSG offers considerable performance advantages over other silica based hosts [97].

3.2.4 Ultrafast laser inscribed waveguides in Erbium doped substrates

As outlined earlier, significant interest exists in the fabrication of compact, low-cost optical amplifier devices for LAN/MAN applications. Ultrafast laser inscription offers a potential route to the fabrication of such devices. As such, the fabrication of active waveguide devices using ULI has been investigated by various groups. The developments in the fabrication of Er-doped waveguide devices have been pioneered by researchers at the Politecnico di Milano, Italy. Initial waveguide fabrication experiments were carried out in Er-Yb doped phosphate glass substrates, with the first demonstration of internal gain published in 2002 [58]. Waveguides were fabricated using a Ti:sapphire laser system emitting 790 nm pulses at a repetition rate of 1 kHz. Relatively high coupling losses of approximately 2.2 dB/facet prevented the group from achieving net gain. This was combined with particularly high amounts of pump absorption due to unoptimised high concentrations of Yb in the substrate material, allowing only a small length of the waveguide to be inverted [58].

In subsequent work by the same group, the coupling losses were improved to approximately 1.2 dB/facet, utilising cylindrical lenses in order to shape the waveguide cross-section, and generate a more symmetric guided mode profile. This enabled the authors to generate a population inversion over a greater length of the waveguide, resulting in internal gain covering the C-band, with a peak internal gain value of 1.4 dB [59].

Further developments occurred with the same group utilising a fabrication laser with a considerably higher repetition rate. In this case, waveguides were fabricated with a diode pumped cavity-dumped oscillator at a repetition rate of 166 kHz. This laser system, along with the use of a high numerical aperture oil-immersion objective, allowed the fabrication of a waveguide which was almost perfectly mode-matched to standard telecommunications single-mode fibre, giving coupling losses of 0.1 dB/facet. This resulted in the achievement of a fibre to fibre *net* gain of 1.2 dB at 1533 nm [98].

Following the achievement of net gain, the same group demonstrated a CW waveguide laser using FBGs to form a cavity either side of the waveguide. For this work, the waveguides were fabricated using the second-harmonic of the laser, enabling an improvement in the amount of net gain achieved to 2.3 dB. An output power of 1.7 mW was achieved with 32% output coupling [60].

The amount of gain produced from a waveguide amplifier was further improved by the Milan group in the publication of an amplifier offering appreciable net gain across the C-telecommunications band (1530-1565 nm). In this case, the waveguide quality was improved further, however this time the waveguides were fabricated using the fundamental wavelength of 1040 nm, combined with a repetition rate of 885 kHz. This enabled a background insertion loss of 1.9 dB to be achieved for a 37 mm long waveguide. A peak net gain of 7.3 dB was achieved [61].

The Milan group progressed the field again in 2006, with the demonstration of a passively mode-locked waveguide laser in a paper by Della Valle [99]. Mode-locking was achieved by the use of a carbon-nanotube (CNT) saturable absorber

placed within a ring-cavity configuration. A bandwidth-limited pulse train of 1.6 ps pulses at a repetition rate of 16.7 MHz was produced from the waveguide laser. The high unsaturable losses of the implemented CNT saturable absorber configuration restricted the exploitation of the full gain bandwidth of the waveguide.

Further work on Er:Yb-doped waveguide lasers by the Milan group has resulted in the demonstration of CW single-longitudinal mode laser emission, by improvements to the FBG based cavity. A maximum output power of 80 mW was achieved, with a maximum of 55 mW being achieved in single longitudinal mode operation [100].

Despite these developments in Er-doped waveguide devices fabricated using ULI, significant interest still exists into producing waveguide amplifiers and lasers in the 1.5 μm region, particularly in interesting glass substrates other than the phosphate glasses used by the Milan group. Waveguide inscription has been carried out in Er-doped OSG by Thomson *et al.*, using a Ti:sapphire laser system operating at a repetition rate of 5 kHz, which is well within the low repetition rate regime [101]. In this case, waveguide losses prevented the achievement of net gain, however subsequent work was able to reduce the insertion losses using the multi-scan technique, enabling internal gain to be demonstrated [102].

Regardless of the developments in active waveguide fabrication using ULI, significant performance advances are still required in order to reach comparable performances to conventional planar waveguide EDWA devices. Once the levels of net gains achieved are close to commercial EDWAs, it will demonstrate to the wider community that the fabrication of active devices using ULI is of commercial interest.

3.2.5 The cavity-dumped stretched cavity oscillator

The fabrication laser used to carry out the work contained within this chapter is considerably different to conventional amplified systems employed in the fabrication of waveguide devices. At its heart is a Yb:glass gain medium, around

which a linear cavity is formed with a Semiconductor Saturable Absorber Mirror (SESAM) utilised at one end of the cavity to form a mode-locked oscillator. The laser central wavelength is 1040 nm with a spectral width of approximately 4 nm. In order to achieve the high pulse energies of hundreds of nanojoules required, and relatively low repetition rates of hundreds of kHz to a few MHz, a stretched cavity configuration is employed. This is achieved by z-folding the cavity in order to reduce the overall footprint of the laser. A Pockels cell is placed within the cavity in order to switch the polarisation of pulses to 'dump' out high pulse energies at a specified pulse repetition rate governed by the signal applied to the Pockels cell [103].

The cavity-dumped oscillator approach has numerous benefits over conventional chirped-pulse amplified systems, particularly in the reduced complexity and footprint. However, significant advances have been made in recent years particularly in mode-locked amplified fibre based systems utilising a master-oscillator-power-amplifier (MOPA) architecture which offer similar benefits. Nevertheless, the use of cavity dumping combined with convenient diode-pumping of a Yb:glass gain medium allows flexible tuning of the repetition rate with little effect on the pulse duration or maximum pulse energy. The laser is air cooled, and uses a single fibre couple diode pump laser, making the system smaller, more reliable and cheaper to run than an amplified Ti:sapphire system.

Figures 3-2 and 3-3 show photographs of the laser used for waveguide inscription experiments. The large number of mirrors used to fold the cavity into a smaller footprint are clearly visible.

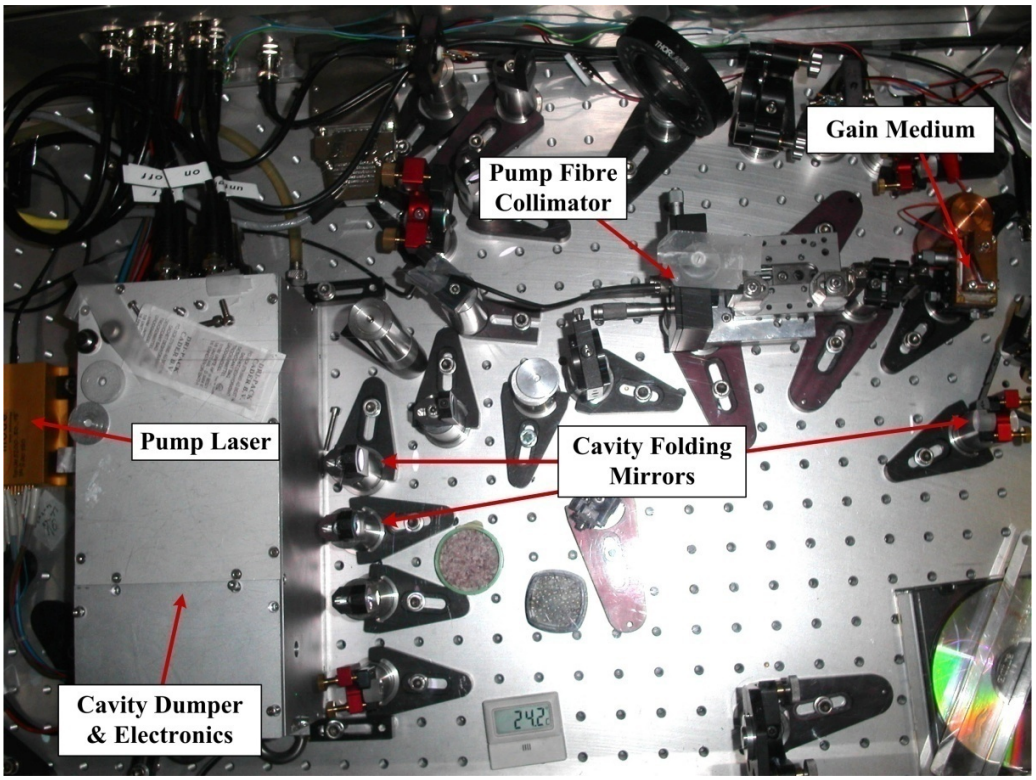

Figure 3-2. Overhead view of the cavity dumped oscillator

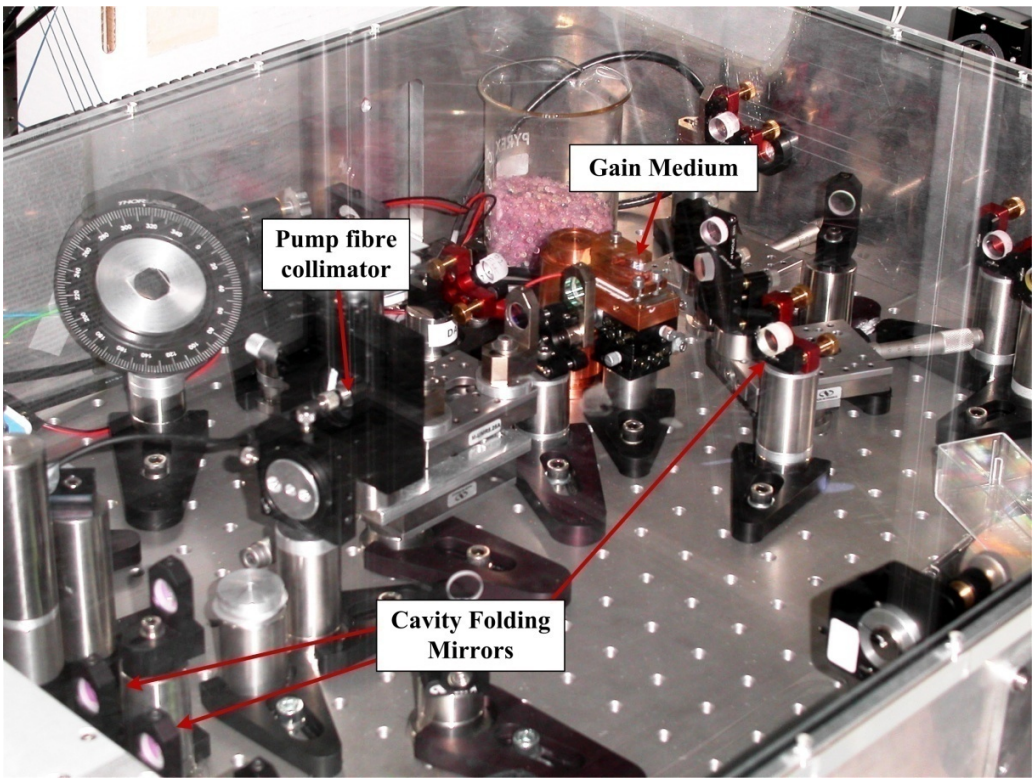

Figure 3-3. Alternate view of the cavity dumped oscillator

The laser in the configuration used for the work presented in this chapter is capable of outputting pulse energies of up to approximately 500 nJ at repetition rates up to 1.3 MHz, with a pulse duration of approximately 350 fs. This allows the system to access the flexible intermediate repetition rate regime, whereby control over thermal accumulation can be employed by tuning appropriate fabrication parameters. The output beam quality is near-diffraction limited, with an M^2 of 1.15.

3.3 WAVEGUIDE FABRICATION IN OXYFLUORIDE SILICATE GLASS

3.3.1 Absorption spectra of OSG samples

The substrate material used for the work contained in this chapter was fabricated using a precursor composition of $61SiO_2$ - $12Na_2O$ - $3Al_2O_3$ - 12LaF - $12PbF_2$ (mol %). The fabrication and spectroscopic optimisation of this glass is described extensively in [97]. Sodium and aluminium are typically used as network modifiers in silica-based glasses in order to increase the RE ion solubility by forming extra sites for RE ions to occupy [93]. A range of samples with different dopant concentrations were provided. A table showing the dopant concentrations of the six samples used for waveguide fabrication is shown in Table 3-2. Erbium ion concentrations of 0.5, 1 and 2 weight % were provided, along with samples containing ytterbium as a co-dopant in a 1:2 ratio of Er to Yb.

Sample	ErF_3 (wt%)	YbF_3 (wt%)
P4	0.5	0
P10	0.5	1
P7	1	0
P11	1	2
P1	2	0
P15	2	4

Table 3-2. List of sample dopant concentrations supplied by Leeds University.

In order to determine the amount of absorption of the $^4I_{13/2}$ to $^4I_{15/2}$ transition, the samples were placed in a Bruker IFS 66V/S FT-IR spectrometer. A background scan with no sample was taken, and then the absorption spectra of the samples were sequentially measured. The observed spectra were normalised to the signal at a wavelength of 1650 nm in order to account for any alignment differences between samples. A wavelength 1650 nm was chosen as it is well outside any absorption bands of the substrate glass. Figure 3-4 shows the absorption spectra of samples P4, P7 and P1, all without ytterbium as a co-dopant.

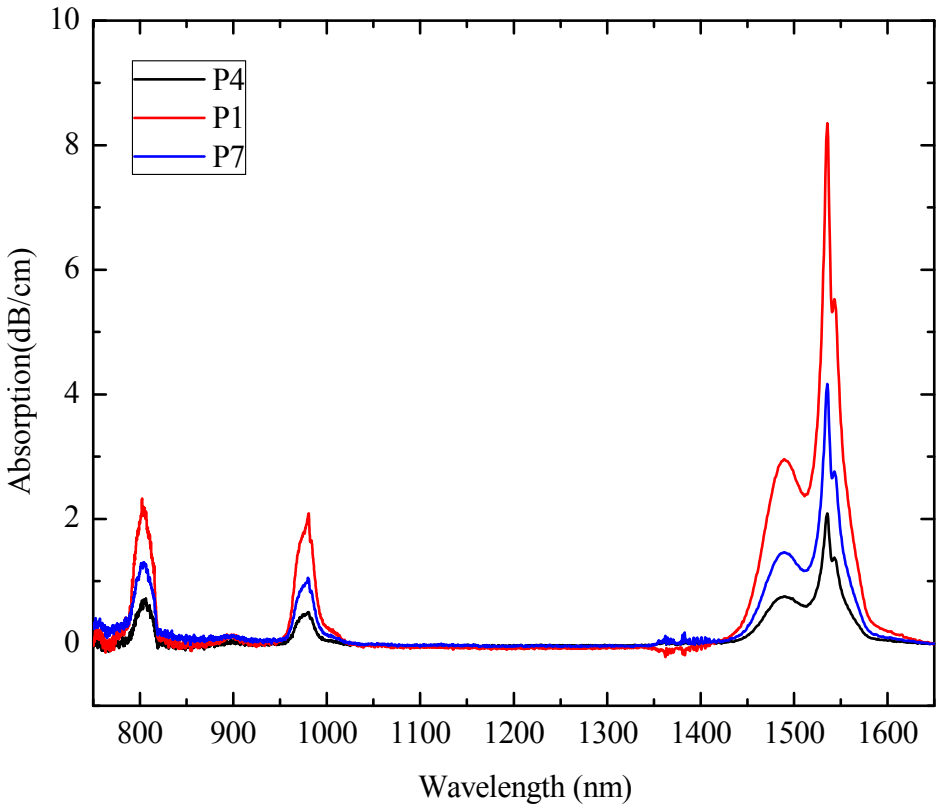

Figure 3-4. Absorption spectra for Er-doped OSG samples P4, P1, and P7.

It can be seen from Figure 3-4 that the amount of absorption of the $^4I_{13/2}$ to $^4I_{15/2}$ transition scales comparably with the amount of Er dopant concentration in the substrate. The Er absorption bands at 800 nm and 980 nm are also clearly visible. Figure 3-5 shows the absorption spectra of samples P10, P11 and P15, all containing Er and Yb in a 1:2 ratio.

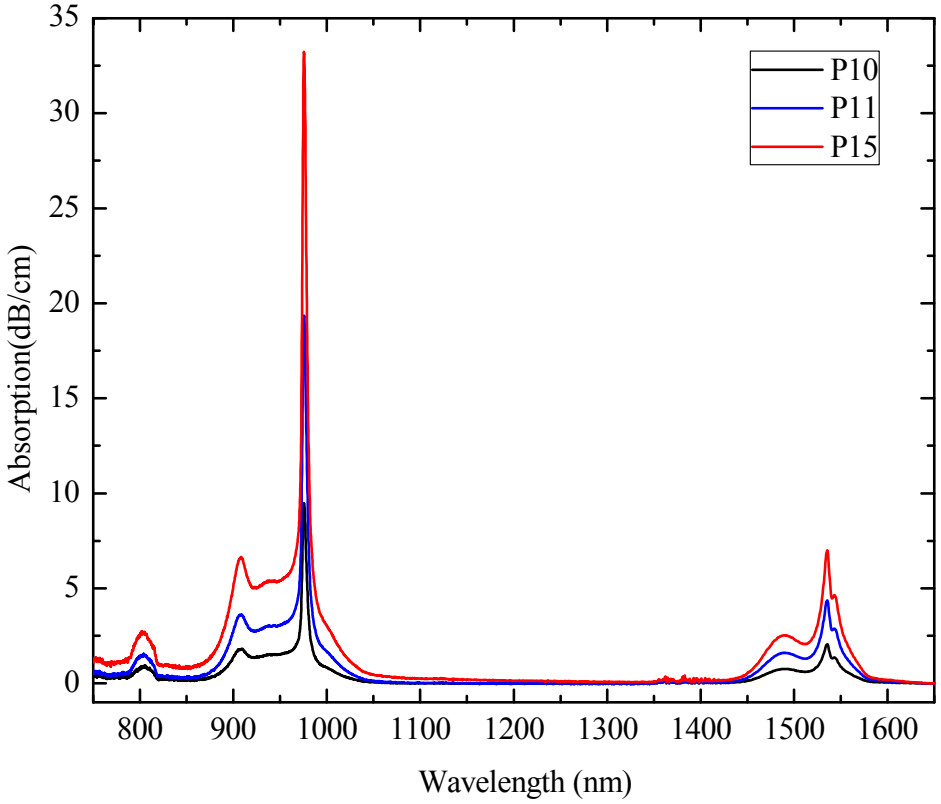

Figure 3-5. Absorption spectra for Er:Yb-doped OSG samples P10, P11 and P15.

The absorption band contributed by the Yb co-dopant is clearly visible in Figure 3-5, with a sharp peak at 975 nm, which is a characteristic of Yb. As seen in Figure 3-4, the amount of absorption of the $^4I_{13/2}$ to $^4I_{15/2}$ transition scales with dopant concentration, however sample P15 appears to have less absorption than expected at both the Er band centred on 1535 nm and the Yb band peaking at 975 nm. This may indicate that the amount of both dopants present in this sample is less than indicated by the supplied concentration information.

The obtained absorption spectra allow the amount of GSA to be calculated, which allows the various contributions to the waveguide losses to be determined. This also enables measurement of the amount of GSA which needs to be overcome in order to achieve internal gain.

3.3.2 Initial waveguide fabrication experiments

In order to achieve a waveguide amplifier, a net signal gain needs to be obtained. As mentioned earlier, in the case of Erbium which can pumped as either a three-level or quasi-two level system, the ground state absorption resulting from the $^4I_{15/2}$ to $^4I_{13/2}$ transition must first be overcome. Once this internal gain condition is achieved, the waveguide coupling and propagation losses must then be overcome in order to achieve net gain. Thus, it is critically important to minimise the waveguide losses in order to achieve net gain in the situation where the internal gain per unit length supplied by the material is close to achievable losses present in the waveguide.

The first task when attempting to inscribe high quality waveguides in any host material is to minimise the waveguide losses. As the form and mechanisms of the refractive index changes induced by ULI are highly material dependant, it is necessary to perform trial and error waveguide fabrication experiments. This allows one to home in on a set of parameters that will generate the optimal waveguiding structures. As the target application for EDWAs is in telecommunications, to achieve low coupling losses the target waveguides should have a mode field diameter (MFD) of standard telecommunications fibre. The waveguides fabricated in this chapter have a target MFD to match that of Corning SMF-28 fibre, which has a MFD of 11.4 μm, defined as the width at which the mode intensity reaches $\frac{1}{e^2}$ of the peak value.

Figure 3-6 shows a schematic diagram of the ULI setup, which is used solely in the transverse writing geometry. The output from the cavity-dumped oscillator was passed through half and quarter wave plates respectively in order to control the polarisation state of the beam. The beam was then passed through a variable neutral density (ND) filter to control the laser power. From the ND filter, the beam was then directed onto the focussing objective by a series of mirrors. The focussing objective was mounted on a micrometer stage to facilitate vertical alignment of the writing plane. The sample was mounted on a set of computer controlled PI (Physik Instrumente) M-511.DD XY motorised translation stages.

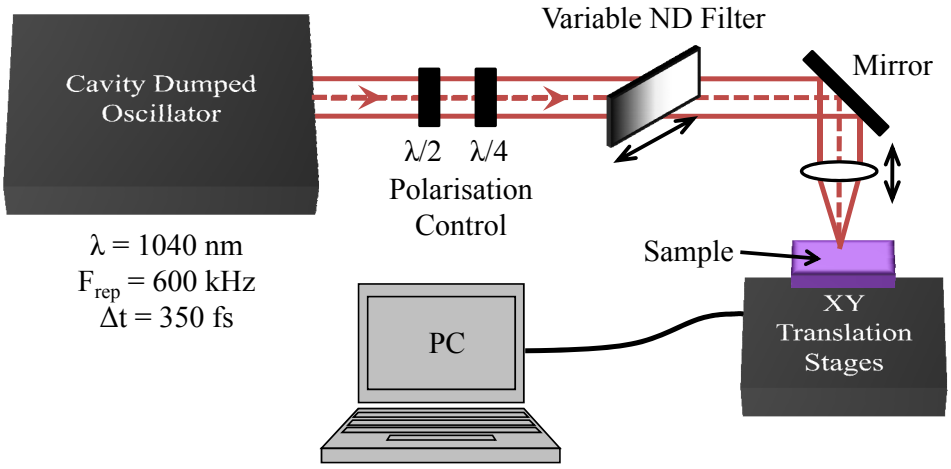

Figure 3-6. Schematic diagram of waveguide fabrication setup

For initial waveguide fabrication experiments, both single and multi-scan fabrication techniques were used. As mentioned in Chapter 2, multi-scan fabrication is a technique for controlling the cross-sectional shape of the induced refractive index change. It relies on building up the refractive index change from multiple passes, each with an incremental movement relative to the previous scan. Figure 3-7 shows a schematic diagram of the multi-scan fabrication technique.

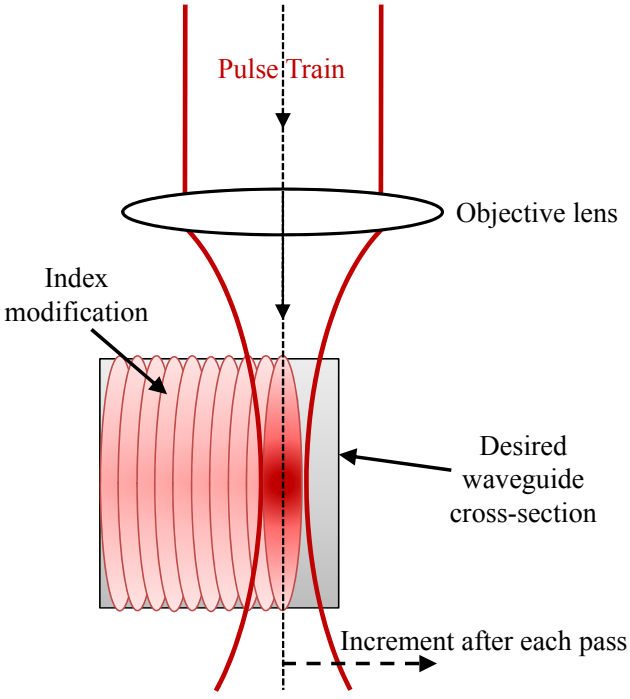

Figure 3-7. Schematic diagram of the multi-scan technique.

As the magnitude of the refractive index change induced by ULI in silica based glasses is typically similar to the index contrast found in telecoms single-mode optical fibres, the multi-scan waveguides were designed to have a cross-sectional size of 8 μm, equivalent to the core diameter of SMF-28 optical fibre. The 8 μm size core was constructed using 20 fabrication scans with 0.4 μm scan separation, and separately using 40 fabrication scans with 0.2 μm separation. The scan separations used are considerably smaller than the writing beam diameter, ensuring a high degree of spatial overlap between successive fabrication passes.

The sample chosen for the initial fabrication trial was sample P1, containing 2wt% ErF_3. A range of pulse energies from 83 to 345 nJ were used, focussed approximately 150 μm below the sample surface using a ×50 0.6 numerical aperture (NA) objective lens. The beam did not fill the full aperture of the lens, resulting in an effective lens $NA_{eff} = 0.3$. Translation speeds of 1 → 4 mm/s were used for the multi-scan waveguides, with the inclusion of 0.5 mm/s for 20-scan waveguides. Single-scan waveguides were written with the same translation speeds. The polarisation of the laser was set to be perpendicular to the laser beam and writing direction. The repetition rate was chosen to be 600 kHz, placing the inscription within the flexible intermediate repetition rate regime. After fabrication, the sample was diced perpendicular to the waveguide axis, and the facet was ground back and polished to an optical finish. The final waveguide length was 16 mm.

3.3.3 Waveguide morphology and guided modes

In order to ascertain which parameters yielded promising structures, microscope images of the waveguide facets were obtained using a conventional white-light brightfield microscope operating in transmission mode. The guiding properties of the structures were then observed by imaging the guided modes at the output facet onto an Electrophysics-7290A IR Vidicon camera, while coupling 1550 nm light from the opposite end using fibre butt-coupling. The obtained images were then

calibrated by imaging a US Air Force (USAF) target identifier containing scaled patterns with defined spatial frequencies.

The fabricated structures showed a wide range of morphological differences. Single-scan structures showed some degree of asymmetry, however not to the same degree as would be expected for structures inscribed at low repetition rates as observed in OSG waveguides inscribed at 5 kHz by Thomson *et al.* [101]. Almost no morphological differences were observed between waveguides fabricated using 20 scans and those fabricated using 40 scans of the same pulse energy and translation speed. This may be an indication that the refractive index modification has reached a saturation point given the amount of scan overlap. Figure 3-8 below shows cross-sectional microscope images and corresponding guided mode profiles at 1550 nm for three multi-scan waveguides fabricated using increasing pulse energies. The waveguide shown in Figure 3-8 a) was fabricated using 83 nJ pulses, a translation speed of 1 mm/s and 40 fabrication scans. 3-8 b) was fabricated using 168 nJ, 0.5 mm/s and 20 scans. 3-8 c) was fabricated using 345 nJ, 2 mm/s and 20 scans.

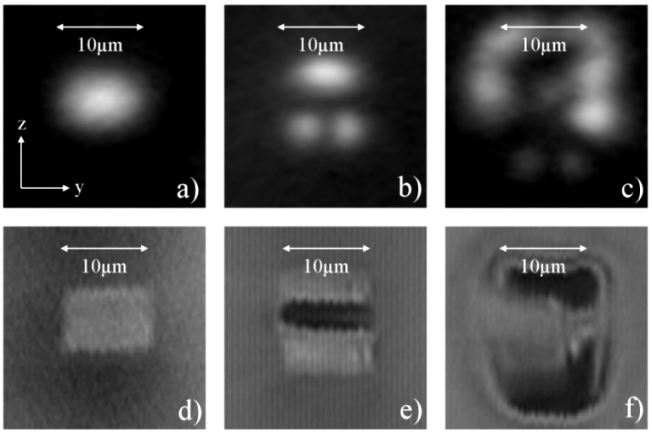

Figure 3-8. a) - c) Guided mode profiles for three multi-scan waveguides. d) - f) Corresponding microscope facet images of the same waveguides.

From Figure 3-8 it can be seen that at the high pulse energy of 345 nJ significant optical damaging is present, characterised by dark structures in f). Guiding is observed around the fabricated structure, a contribution to which may originate from stress induced by the damage. As the pulse energy is decreased, the amount

of damage is reduced. At a pulse energy of 168 nJ as shown in e), only regions close to the peak intensity of the focussed beam are above the threshold for damage formation, and regions above and below show refractive index modification as these regions appear to be below the threshold for the onset of damage. Further reducing the pulse energy generates smooth structures without any visible damage. At a pulse energy of 83 nJ as shown in Figure 3-8 d), a homogeneous smooth refractive index change structure is observed, with single-mode guiding at 1550 nm.

For single-scan waveguides, high pulse energies yield complex structures containing regions of damage and refractive index modification. Figure 3-9 a) and d) show a guided mode profile and corresponding microscope image of a waveguide fabricated using 345 nJ pulses and a translation speed of 4 mm/s. The guided mode profile shows a mixture between several low-order transverse modes. As the pulse energy is reduced, the amount of asymmetry in the cross-section is increased. This effect may be due to the reduced pulse energy not being able to drive significant thermal accumulation at this repetition rate. Figure 3-9 b) and e) show a waveguide fabricated with 168 nJ pulses at 2 mm/s. The mode here is large and poorly confined, thus the waveguide losses are expected to be high due to radiation losses and micro-bends. The guided mode and microscope image of Corning SMF-28 are shown in Figure 3-9 c) and f) for comparison.

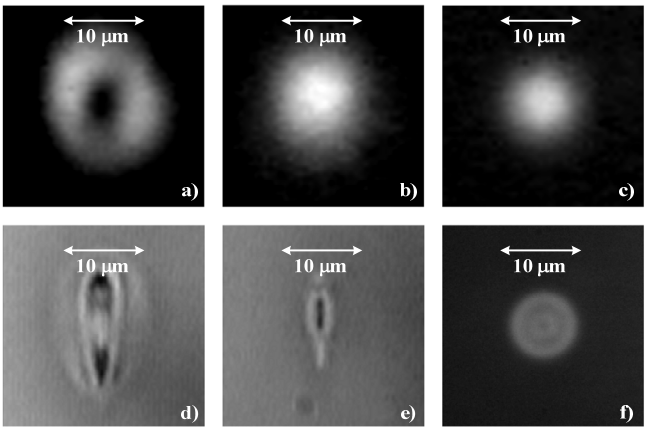

Figure 3-9. a) - c) Guided mode profiles for three single-scan waveguides. d) - f) Corresponding microscope facet images.

3.3.4 Loss characterisation

The waveguide insertion loss (IL) is the most important parameter defining the quality of the fabricated waveguide. IL is defined as the total loss of inserting the device into a fibre-optic test-bed, including coupling loss, propagation loss, and any Fresnel reflections from the optical interfaces. Figure 3-10 shows a schematic diagram of the experimental setup for measuring insertion losses. Initially, a piece of SMF-28 single-mode fibre is fusion spliced to the source and detector sides of the characterisation rig. A reference measurement is then taken for both signal and absolute reference channels, allowing accurate calibration of any subsequent changes in the signal power. The fibre is then broken, cleaved and butt-coupled to the waveguide facets using index matching gel, to remove the contribution from Fresnel reflections. The sample and fibres are mounted on separate high-precision XYZ translation stages with pitch and yaw rotational stages placed on top. The IL is then defined as the minimum difference in the signal observed in dB when subtracted from the reference measurement through the optical fibre. Due to the nature of the measurement, the IL cannot be higher than measured, so any errors would only contribute to the IL being lower.

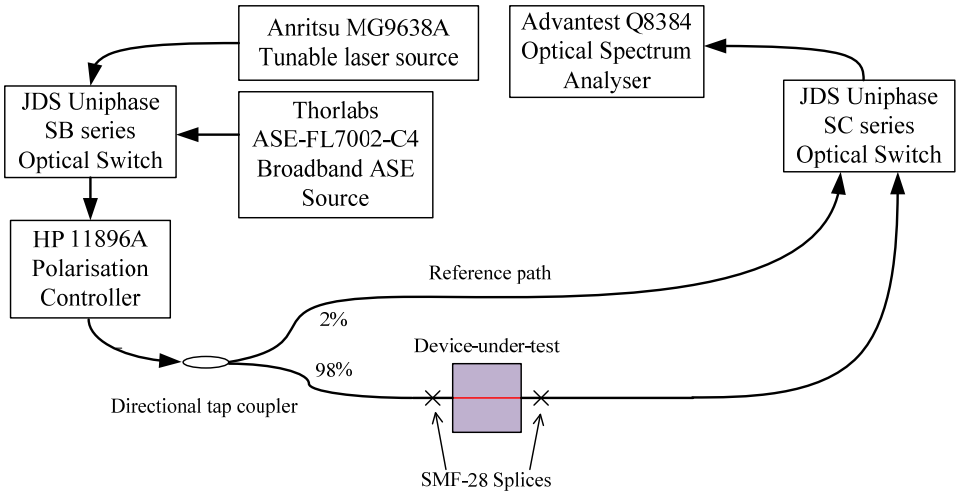

Figure 3-10. Schematic diagram of IL characterisation setup.

In order to extrapolate the relative contributions to the insertion losses from coupling and propagation losses (PL), the coupling loss (CL) from fibre to waveguide was also measured. This can be estimated using the overlap integral,

however a more accurate value can be obtained by measuring the quantity directly. This was achieved by comparing the signal throughput obtained when a single-mode fibre was butt-coupled to the waveguide output, with a highly multi-mode fibre with a numerical aperture of 0.275 ± 0.015 at the waveguide output. The coupling loss between the waveguide and the multimode fibre is negligible due to the vast number of supported modes, leaving the difference between single and multi-mode fibres as the coupling loss per facet to single-mode fibre.

All measurements were carried out for the waveguides with the tunable laser set to a wavelength of 1550 nm. The amount of GSA at 1550 nm was calculated from the absorption spectra shown in section 3.3.1 and subtracted from the total insertion loss.

The possible error in the IL measurements is estimated to be ~0.3 dB due to alignment accuracy. The error in the CL measurement is estimated to be ~±0.2 dB also due to alignment accuracy. The error is the PL measurement estimated to be ~±0.2 dB/cm. The origins of propagation losses can be attributed partly to glass inhomogeneities and partly to non-uniformity in the sample translation movement and scattering or absorption centres present in the modified regions.

Figure 3-11 shows the IL, CL and PL of multi-scan waveguides fabricated using 40 scans. The lines are included as a guide to the eye. It is clear from the morphological studies presented in section 3.3.3 that high pulse energies produce significant optical damaging, with guiding occurring predominantly around the damage structures. For slightly lower pulse energies, the amount of damage is reduced, however the guided modes in this regime have increased overlap with damaged material. This manifests as high propagation losses in the intermediate pulse energy range. The relatively high CL value shown by the 168 nJ 1 mm/s waveguide is due to a defect on the waveguide facet, possibly a polishing artefact.

The lower pulse energies of 83 nJ and 118 nJ do not show any visible damage, and consequently the IL for these waveguides is considerably lower, with little contribution from propagation losses. Clearly there is a low loss regime occurring for these two lower pulse energies.

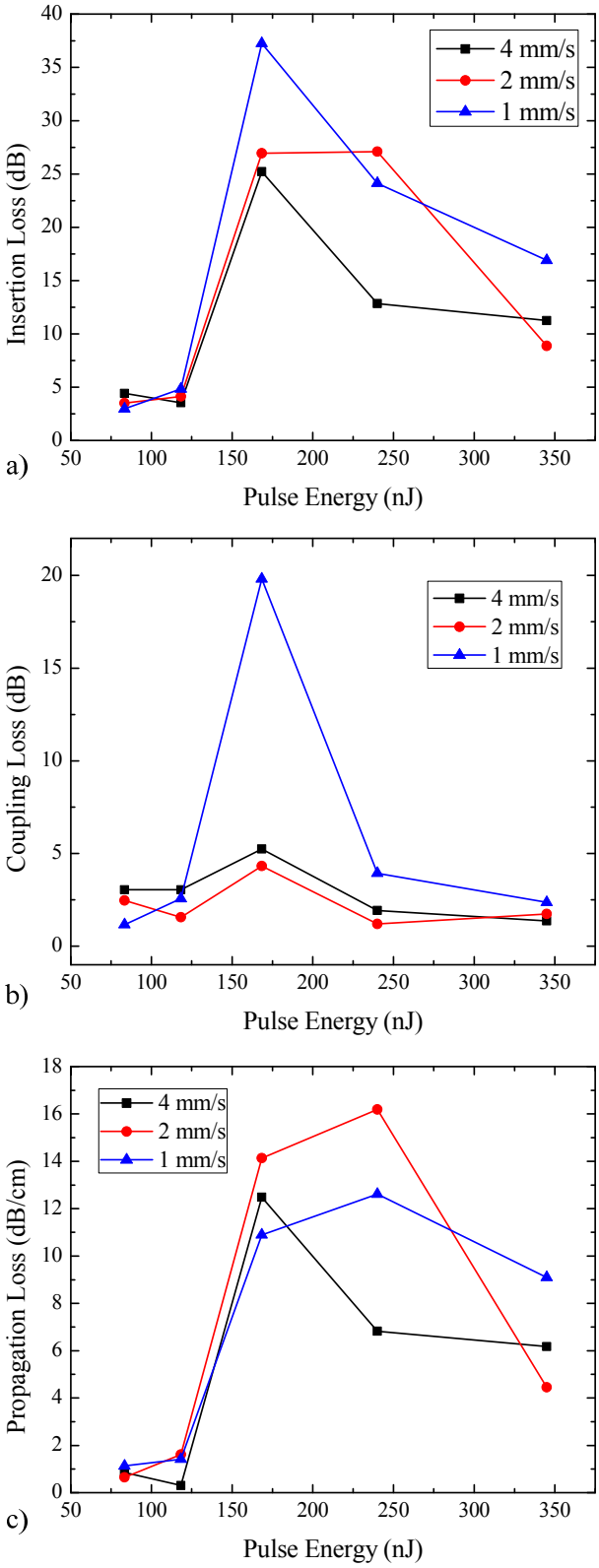

Figure 3-11. Insertion loss, Coupling loss and Propagation loss for 40-scan waveguides.

Figure 3-12 shows IL, CL and PL results for 20-scan waveguides for varying fabrication parameters. The lines are included as a guide to the eye. The observed behaviour is similar to that of the 40-scan waveguides, showing increased losses for intermediate pulse energies where the guided mode overlaps strongly with the damage regions, causing large scattering losses which are observed as propagation loss.

At high pulse energies, the coupling losses are lower due to the presence of a large number of guided modes which can be coupled to individually. For intermediate energies, the coupling losses are higher, reducing again for low pulse energies as the waveguides become single-mode with a more symmetrical mode profile. A low loss window is again observed for the two lowest pulse energies of 83 and 118 nJ, corresponding to the absence of optical damage.

Comparing the 40-scan and 20-scan waveguides, a larger variance between losses is observed for 20-scan waveguides which is indicative of more saturation occurring in the refractive index change for the larger number of scans. This would indicate that 40-scan waveguides may provide a more homogeneous structure which could be advantageous for the fabrication of more high quality waveguides. Both 40 and 20-scan structures show a low-loss processing window at the lowest two pulse energies due to the lack of optical damaging.

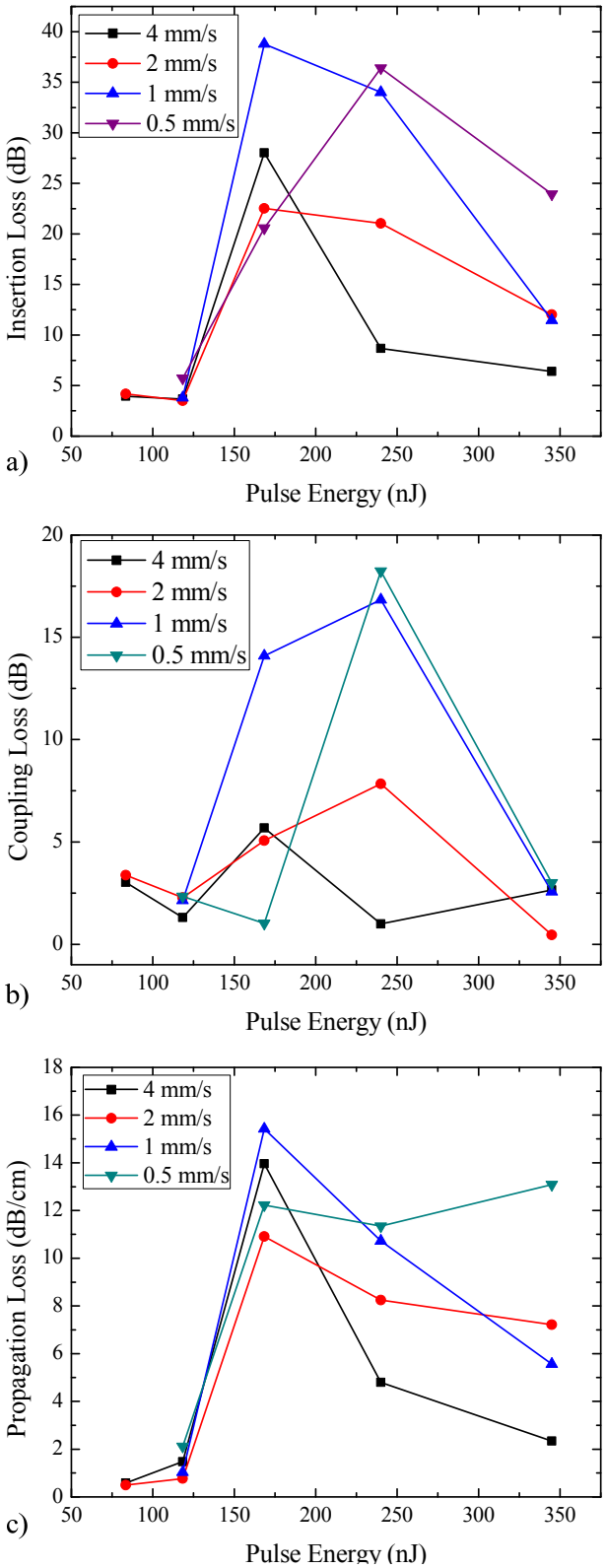

Figure 3-12. Insertion loss, Coupling loss and Propagation loss for 20-scan waveguides.

Figure 3-13 shows the IL, CL and PL for single-scan waveguides for varying fabrication parameters. The lines are included as a guide to the eye.

For the single-scan waveguides, the behaviour is considerably different to that observed for multi-scan waveguides. Low pulse energies yield highly asymmetric, narrow structures with poorly confined guided modes. This can be observed as high CLs due to the poor mode matching between fibre and waveguide.

As the pulse energy is increased, the CLs and corresponding IL decrease due to enhanced confinement, reaching a minimum at high pulse energies for fast translation speeds. The minimum in CL is reached at the lower pulse energy of 168 nJ for the two slower translation speeds, which may be due to the reduced speed inducing more refractive index change, allowing the optimal mode size to be reached at lower pulse energies.

Overall, it is clear that for waveguides fabricated in OSG, considerably lower losses are obtained using multi-scan fabrication. The absence of damage at low pulse energies allows relatively low insertion losses to be obtained. A second round of waveguide fabrication with a much narrower range of parameters was carried out in several samples with varying dopant concentrations.

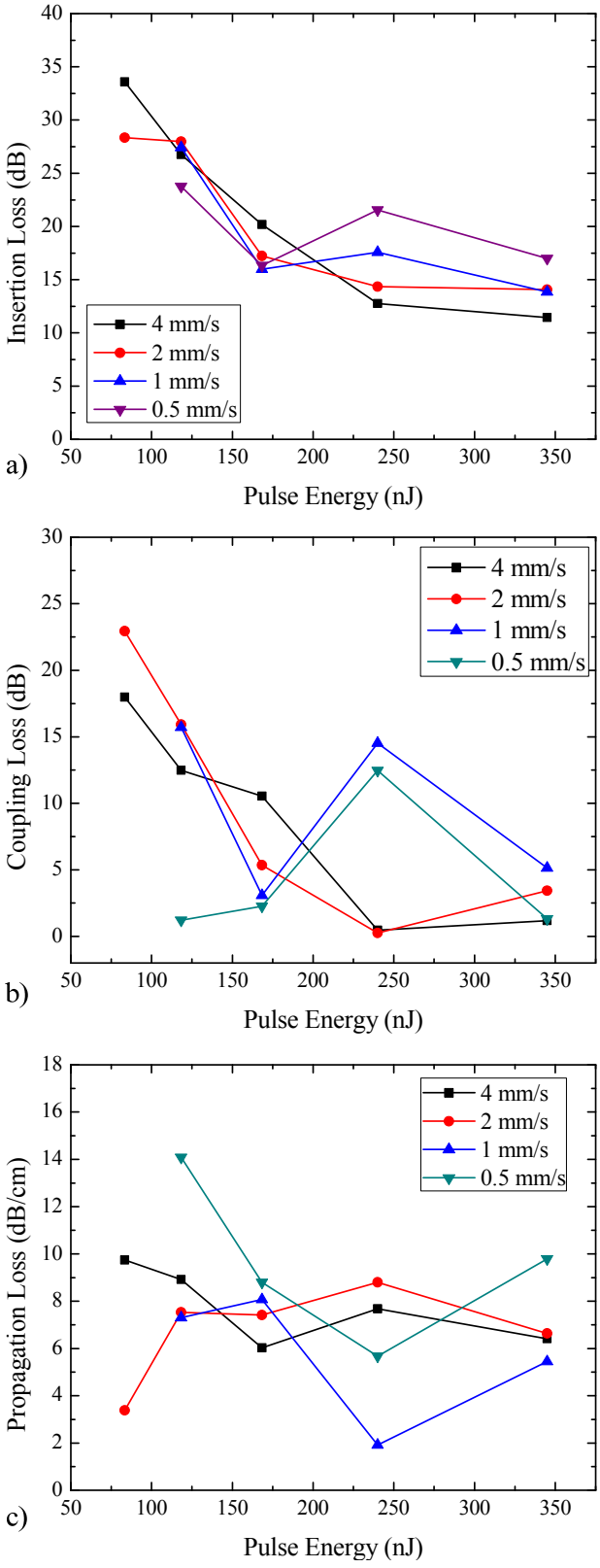

Figure 3-13. Insertion loss, Coupling loss and Propagation loss for single-scan waveguides.

3.3.5 Optimised waveguide fabrication experiments

Given the trends observed in the initial characterisation experiments, a further round of waveguide fabrication was carried out, using only multi-scan fabrication with a considerably narrower range of parameters. With gain measurements in mind, this narrow range of parameters was used to inscribe waveguides in samples containing the range of dopant concentrations as shown in section 3.3.1. Four pulse energies from 80 to 150 nJ were used, along with translation speeds of 1, 2 and 4 mm/s. Multi-scan waveguides with both 20 and 40 scans were fabricated. Waveguides with a 1 mm/s translation speed and a pulse energy of 80 nJ were not inscribed due to the fabrication laser breaking down. Figure 3-14 shows the insertion loss trends for waveguides fabricated in sample P11 with a waveguide length of 10 mm. The lines are included as a guide to the eye.

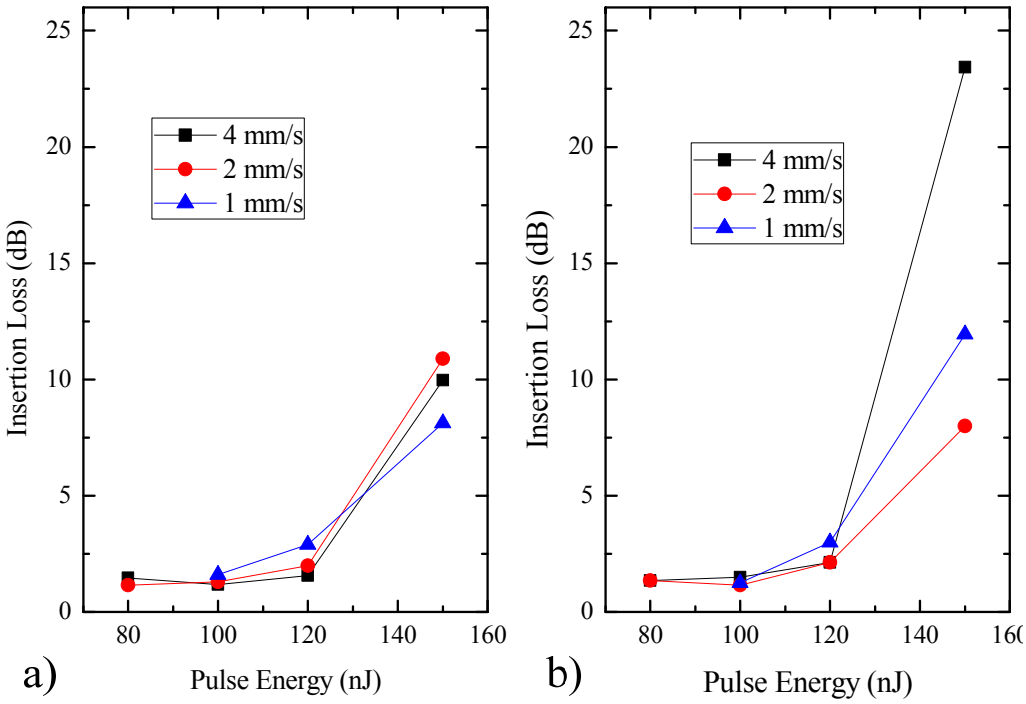

Figure 3-14. a) Graph showing IL results for 20-scan waveguides. b) Graph showing IL results for 40-scan waveguides.

From Figure 3-14, it is clear that the three lowest pulse energies yield the lowest losses. Within the lowest three energies, it appears that for 40-scan waveguides, there is less variance in the ILs between translation speeds, which may be an

indication that the refractive index change is saturated. Indeed, little difference is observed between 20 and 40 scan waveguides, the latter having twice the amount of scan overlap.

The lowest insertion loss obtained was obtained using 80 nJ pulses, a 2 mm/s translation speed and 20 fabrication scans. Figure 3-15 shows a microscope image of the waveguide facet and the corresponding guided mode. The waveguide had a $1/e^2$ mode field diameter (MFD) of 14.5 µm in the y-axis and 12.5 µm in the z-axis. This compares well with the 10.4 µm MFD of SMF-28 at 1550 nm. The error in the MFD measurement was estimated to be ±0.9 µm due to inaccuracies in the focussing. The error in the MFD measurement was evaluated by repeated realignment and measurement of the mode size.

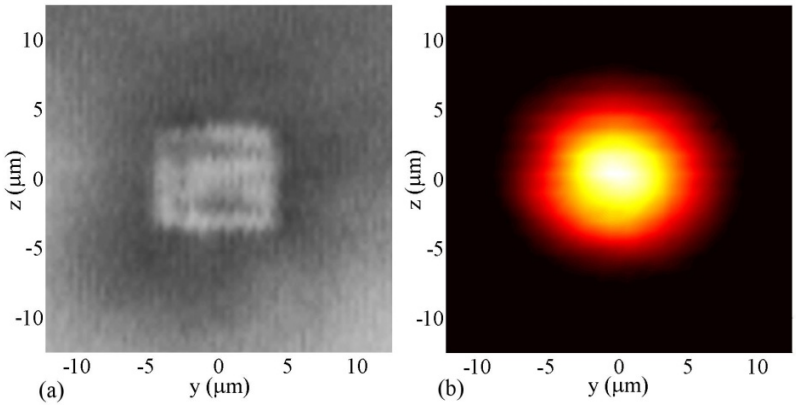

Figure 3-15. a) Microscope facet image of the optimal waveguide. b) Guided mode profile of the optimal waveguide.

The waveguide shown in Figure 3-15 exhibited a total IL of 5.56 dB at 1537 nm, which corresponds to the peak of the absorption spectrum. From the absorption measurements shown in Section 3.3.1, a peak absorption of 4.34 dB was measured, leaving a background IL of 1.22 dB.

The CL at 1550 nm for the waveguide shown in Figure 3-15, was measured to be 0.44 dB/facet, with an estimated possible error of approximately ±0.2 dB due to alignment accuracy. The coupling losses are attributed to the difference in MFD between waveguide and fibre modes, which compares well to an estimation based on the overlap integral between the fibre and waveguide mode, giving a CL value

of 0.3 dB/facet. Given the background IL of 1.22 dB for the waveguide length of 10 mm, the PL was calculated to be approximately 0.34 dB/cm with a possible error of ±0.2 dB/cm.

The polarisation dependent loss (PDL) was measured using a HP11896A polarisation controller and an Anritsu MG9638A linearly polarised tunable laser. The signal was then coupled through the waveguide and into an Advantest Q8384 Optical Spectrum Analyser (OSA). The PDL was measured to be 0.2 dB at 1550 nm, indicating that waveguide birefringence is not significant.

The lowest IL achieved during the second fabrication run could have been further improved, as the coupling losses of 0.44 dB/facet could have been reduced by further optimisation of the multi-scan parameters such as the number of scans. Despite this, the losses achieved were low enough to enable a full gain investigation from the waveguides fabricated in all dopant concentrations.

3.4 GAIN INVESTIGATION OF OSG WAVEGUIDES

3.4.1 Gain measurements

Given the low losses achieved from optimised waveguide fabrication, the gain performance of the waveguides was measured. Figure 3-16 shows a schematic diagram of the experimental setup used to carry out gain measurements. A Thorlabs ASE-FL7002-C4 broadband ASE source and an Anritsu MG9638A tunable diode laser source were connected to an optical switch to be used as the probe signals. The signals were then fed through a HP 11896A polarisation controller and into a 98%/2% broadband directional coupler. A signal reference path was formed from the 2% output in order to monitor any changes in the signal output power. The 98% signal path was then multiplexed with the pump lasers using broadband wavelength division multiplexors (WDMs). A dual wavelength bi-directional pumping scheme was employed, with optical isolators after each pump laser to ensure no damage to the diodes. The outputs from the 980/1550 WDMs were spliced onto SMF-28 fibre and then butt coupled up to the

waveguide using index matching fluid. The signal was then passed into the final optical switch and into an Advantest Q8384 Optical Spectrum Analyser in order to capture the signal power and spectrum.

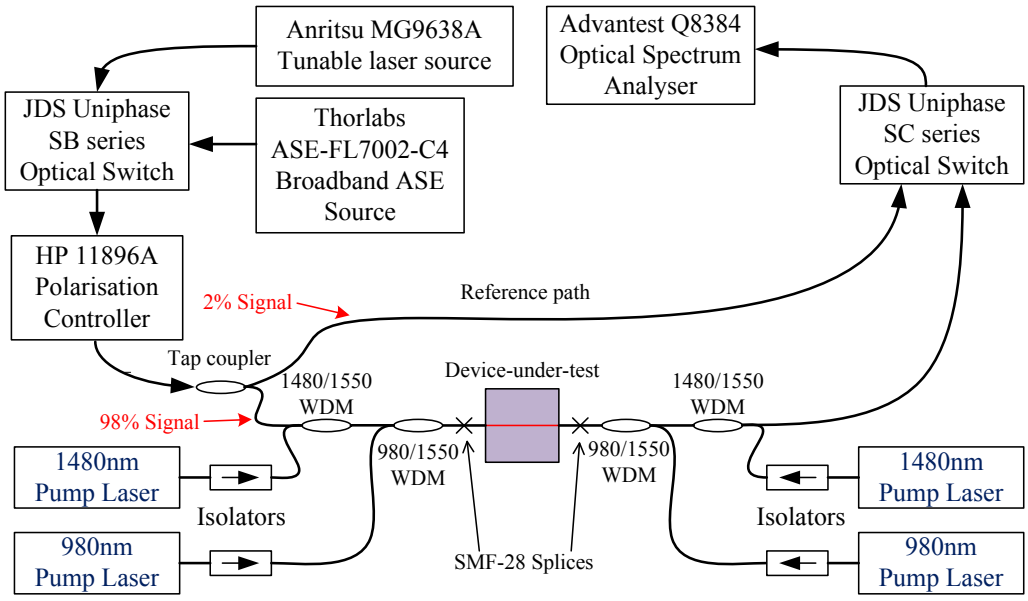

Figure 3-16. Schematic diagram of gain characterisation experimental setup.

The relative gain spectra were measured as follows. Initially, the fibres were accurately aligned to the waveguide using an attenuated broadband ASE source as the signal. The signal spectrum, after travelling through the entire system, is then captured. The pump lasers are then enabled, and the throughput spectrum is again measured, giving the combination of signal, fluorescence and gain. The signal source is then disabled with the pumps remaining on, and the fluorescence spectrum is then recorded. The *relative gain*, which is defined as the change in transmission under pumping is given by equation 3-1.

$$RG_{dB} = \log_{10}\left(\frac{SFG - F}{S}\right) \qquad 3\text{-}1$$

Where RG_{dB} is the relative gain in decibels, SFG is the signal + fluorescence + gain measurement in linear units, F is the fluorescence measurement in linear units and S is the signal measurement in linear units. In order to achieve net gain, the relative gain must exceed the total insertion loss including GSA.

A total pump power of 342 mW at 980 nm and 213 mW at 1480 nm was present at the waveguide facets. After evaluating the relative gain spectra for all samples, only sample P11 showed net gain. Table 3-3 shows a summary of the peak gain results for all samples.

Sample	Er Conc. (wt%)	Yb Conc. (wt%)	Sample Length (mm)	Total Insertion Loss (dB)	Maximum Relative Gain (dB)	Maximum Net gain (dB)
P4	0.5	0	14.0	5.01	3.56	-1.45
P10	0.5	1	14.6	4.59	3.85	-0.74
P7	1	0	12.0	7.40	5.67	-1.73
P11	1	2	10.0	5.56	6.2	**0.64**
P1	2	0	16.0	15.05	11.60	-3.45
P15	2	4	20.5	18.26	12.63	-5.63

Table 3-3. Summary of gain measurement results extracted from the gain spectra at 1537 nm.

Figure 3-17 shows the relative gain spectrum, insertion loss spectrum and net gain spectrum for the optimal waveguide parameters fabricated in sample P11. Maximum gain was achieved under full dual-wavelength pumping. A maximum fibre to fibre net gain of 0.64 dB was achieved using the broadband ASE signal source.

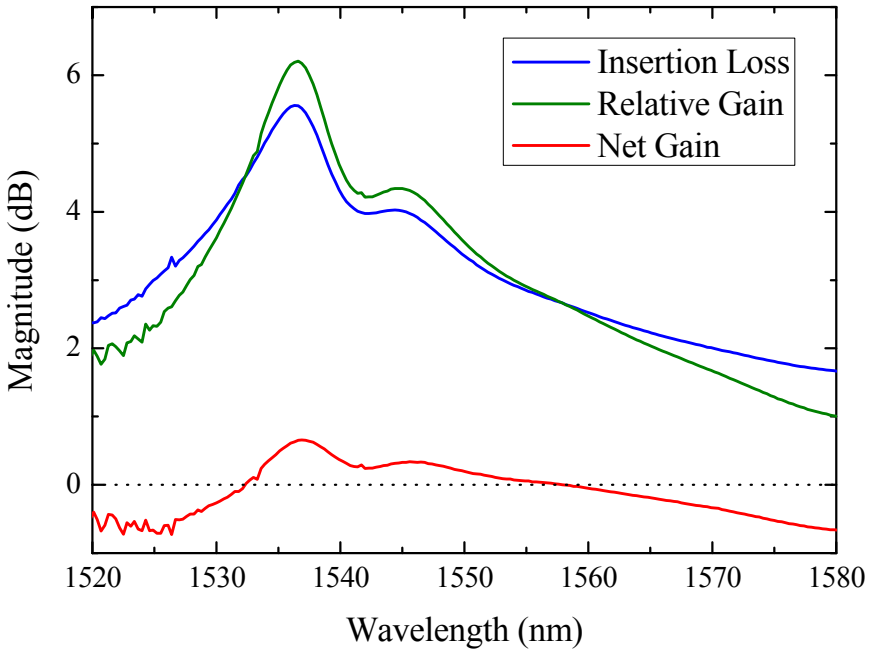

Figure 3-17. Relative gain, total insertion loss and net gain spectra for the optimal waveguide parameters fabricated in sample P11.

In order to avoid spectral hole burning and gain saturation effects, gain versus pump power measurements were subsequently obtained using a tunable laser attenuated to a signal level of -20 dBm. The tunable laser was set to the peak wavelength of the gain spectrum at 1537 nm. Using the tunable laser signal source, a peak net gain of 0.72 dB was observed at 1537 nm. Figure 3-18 shows a plot of the relative gain versus pump power for the same waveguide. In order to confirm the measurements were carried out in the small signal regime, the signal power was increased by 10 dB, with no change to the amount of relative gain observed. To investigate whether polarisation dependant gain (PDG) is significant, the PDL was measured under maximum pumping using the same technique as described in Section 3.3.5. The PDG was measured to be 0.2 dB indicating that polarisation effects are insignificant. As mentioned in Section 3.2.2, pumping at 1480 nm results in a quasi two-level laser system. This results in a non-zero stimulated emission cross-section at the pump wavelength of 1480 nm. Thus, dual wavelength pumping in Er-doped systems can limit the amount of achievable population inversion. Nevertheless a slightly higher relative gain was observed using both pump wavelengths simultaneously.

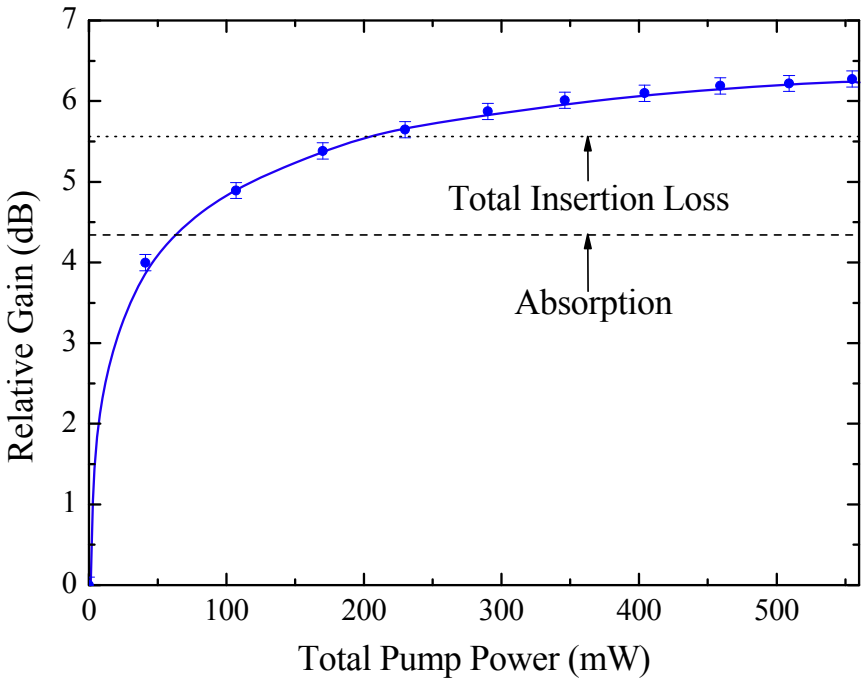

Figure 3-18. Graph showing relative gain *vs* pump power using a tunable laser source as the signal. The line is included as a guide to the eye.

As described extensively in reference [97], the Er-doped OSG substrate material has close to equal stimulated absorption and stimulated emission cross-sections at 1537 nm. Consequently, a saturated relative gain of twice the absorption would be expected for a 100% population inversion. This would yield a relative gain of approximately 8.7 dB. From Figure 3-18, the measured relative gain saturates at approximately 6.3 dB, which would indicate that a total population inversion of approximately 72% was achieved. Given the limited population inversion and clear gain saturation, it can be concluded that significant ion clustering is present at this dopant concentration of 1 wt% Er and 2 wt% Yb. As mentioned in Section 3.2.2, ion clustering leads to CET and upconversion which reduce the amount of achievable gain.

In order to assess the dependence of dopant concentration on the amount of gain, a comparison of the internal gain per unit length achieved for all samples is shown in Figure 3-19. The value of internal gain per unit length allows the insertion losses and varying sample lengths to be compensated for, giving a comparison between sample compositions. All values were obtained under maximum dual

wavelength pump power. The errors were calculated by combining the individual errors in the relative gain (±0.1 dB), total absorption (±0.2 dB) and sample length (±0.01 cm).

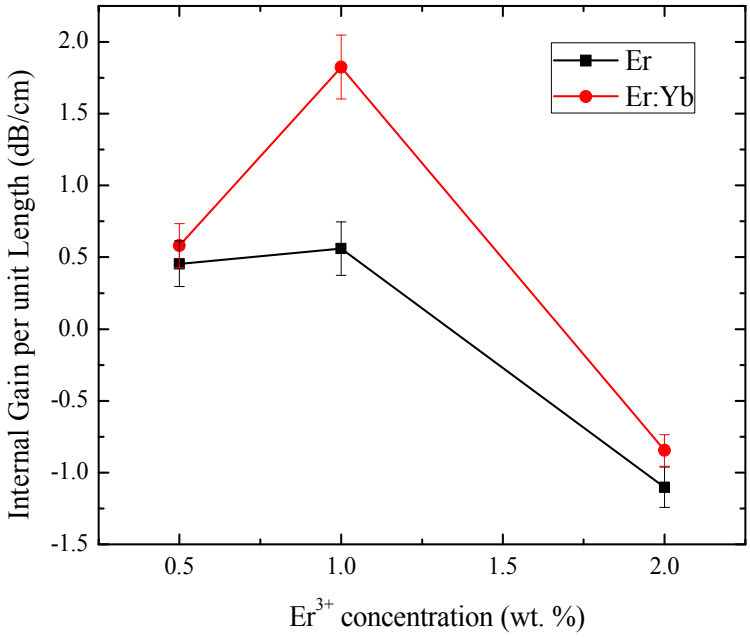

Figure 3-19. Graph showing a comparison of internal gain per unit length for varying dopant concentrations. The line is included as a guide to the eye.

From Figure 3-19 it is clear that the highest dopant concentration of 2 wt% Er yields a large amount of ion clustering, prohibiting the composition from even achieving internal gain. At an Er ion dopant concentration of 1 wt% we achieve the largest amount of internal gain per unit length, allowing the net gain results presented in Figures 3-17 and 3-18. At the lowest dopant concentration of 0.5 wt% Er, internal gain is still achieved, however not enough is present to overcome the waveguide losses and achieve net gain. Interestingly it is clear that the inclusion of Yb boosts the amount of achievable gain for both higher dopant concentrations, however for the lowest Er dopant concentration the improvement is smaller. This may be due to the low concentration reducing the amount of CET between excited Yb ions and ground state Er ions.

Given that evidence of ion clustering is present even in the sample providing the largest gain, further optimisation of the levels of dopant concentration and ratio of

Er:Yb could yield a higher internal gain per unit length. Also, improvements to the waveguide losses and an increase to the total waveguide length would enable a large increase to the achievable net gain. Despite this, it is clear that more significant improvements could be achieved from a more optimised substrate composition able to hold a higher level of doping, or containing larger stimulated emission and absorption cross sections.

3.5 DEMONSTRATION OF LASER ACTION

3.5.1 Formation of a laser cavity using an Er:Yb doped OSG waveguide

Given the net gain results obtained from the waveguides shown in Section 3.4, a proof of principle waveguide laser was constructed. In order to form a cavity, fibre-Bragg-gratings with reflectivities of 99.99% and 99.47% at 1535.8 nm were used to provide the necessary feedback. The reflectivity spectra of the two FBGs were interrogated using a Thorlabs ASE-FL7002-C4 broadband ASE source combined with a circulator in order to separate the reflected signal. The spectra were recorded on an Advantest Q8384 OSA set to give a resolution of 0.01 nm. Figure 3-20 shows the normalised reflectivity spectra of the two FBGs.

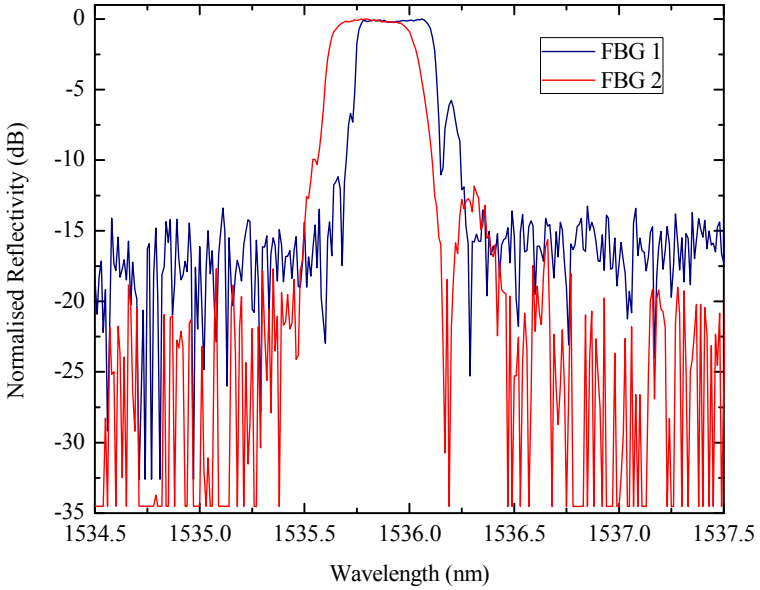

Figure 3-20. Graph showing normalised reflectivity spectra of the two FBGs used to form a laser cavity.

The FBGs were butt-coupled to the waveguide facets using index matching fluid, with the lower reflectivity FBG side forming a 0.5% output coupler. The cavity configuration is shown in Figure 3-21. The waveguide was pumped bi-directionally with up to 342 mW at 980 nm and 213 mW at 1480 nm with a 50/50 power splitting ratio. WDMs were used to multiplex and de-multiplex the pump wavelengths either side of the waveguide. An angle cleaved fibre was used at the 1550 nm port of the non-output side of the configuration in order to remove any reflections from entering into the system. The laser output fibre was spliced to an angle polished pig-tail. The total physical cavity length was 207.5 cm.

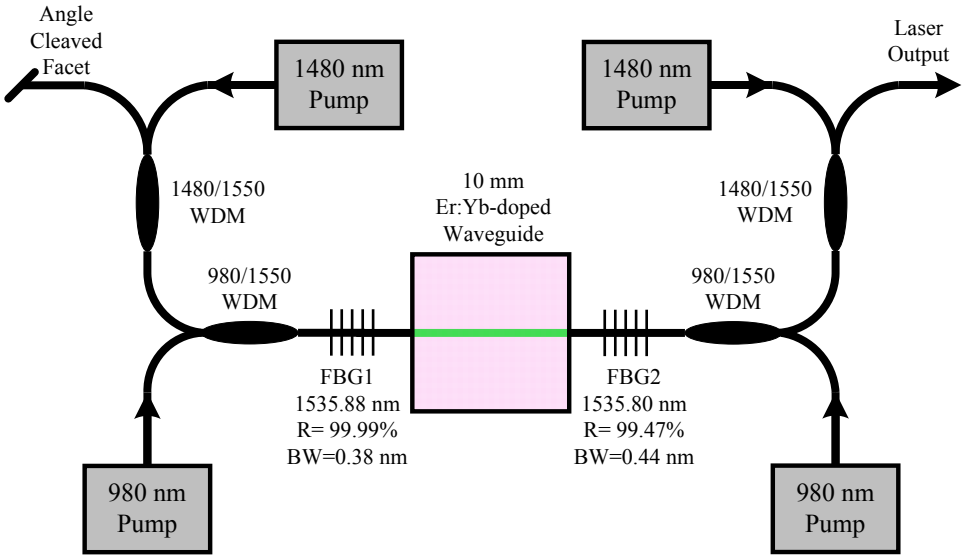

Figure 3-21. Schematic diagram of the cavity configuration used to form a waveguide laser.

3.5.2 Laser emission from an Er:Yb doped OSG waveguide

The output port of the cavity configuration was connected to the OSA, which was set to give a resolution of 0.5 nm. The output spectrum was recorded over a wide spectral region for varying 980 nm pump powers. Figure 3-22 shows the evolution of the laser output spectrum as a function of 980 nm pump power. At low pump powers, a small dip is seen superimposed onto the peak of the fluorescence spectrum due to the FBG resonance. As the pump power is

increased, laser threshold is achieved with a clear lasing peak visible on top of the fluorescence. No change was observed in the ASE spectrum immediately below or at any point above the lasing threshold, which would indicate that spectral hole burning is not an issue for the configuration used.

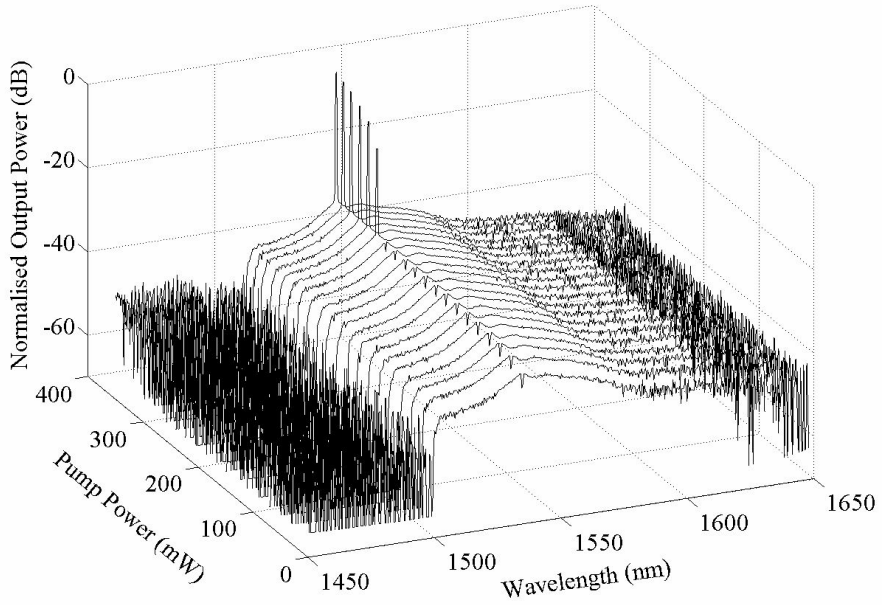

Figure 3-22. Graph showing the evolution of the laser output spectrum as a function of 980 nm pump power.

Laser output power as a function of both 980 nm and dual wavelength pump power was measured at the peak of the laser output spectrum. This was measured by calibrating the OSA set to a narrow wavelength range at the peak of the output spectrum using a calibrated power meter as a reference. The signal power at the OSA was then measured as the pump currents were increased incrementally. For dual wavelength pumping, the power ratio between 980 nm and 1480 nm pumps was approximately constant from a total power of 45 mW upwards. Figure 3-23 shows the laser output power versus pump power for both dual wavelength and 980 nm pumping alone.

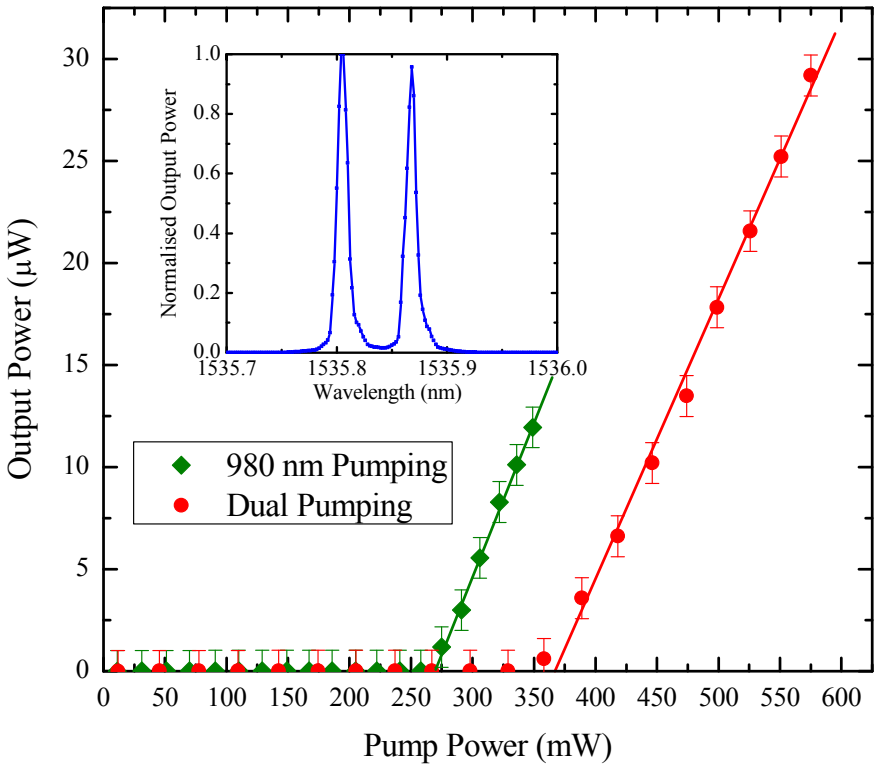

Figure 3-23. Graph showing laser output power versus input pump power for both 980 nm and dual-wavelength pumping schemes. Inset shows the fine laser spectrum at maximum pump power.

Clear lasing threshold behaviour was observed for both dual wavelength pumping and 980 nm pumping alone. A lower threshold for 980 nm excitation of 250 mW was observed compared to the ~325 mW for dual wavelength pumping due to the increased efficiency of pumping at 980 nm. As mentioned in Section 3.4.1, more gain was observed using dual wavelength pumping as there was insufficient 980 nm pump power alone to saturate the relative gain. A maximum output power of 30 μW was achieved measured at the output port, however this could have been improved significantly by using a larger amount of output coupling.

The inset graph presented in Figure 3-23 shows the spectral line shape of the laser output at maximum dual wavelength pump power. This was measured with the OSA set to give a resolution of 0.01 nm. Two clearly defined peaks are observed, which were verified to be in the same polarisation state by passing the signal through a rotating analyser whilst observing the laser output spectrum. The cavity

mode spacing was calculated to be 0.4 pm which is a factor of 160 times closer than the spacing observed. The two peaks in the output spectrum could be due to an etalon formed by the Fresnel reflections at the waveguide facets. As an index matching fluid of refractive index 1.45 was used, the finesse of the etalon would be extremely small, given that the refractive index of the bulk material is approximately 1.65. Despite the low finesse, the strength of the etalon fringes may be enough to preferentially select the longitudinal modes on which the laser oscillates by modulating the intra-cavity loss spectrum. A rough calculation of the wavelength spacing between etalon fringes yields a value of approximately 70 pm, which is very comparable to the ~65 pm observed in the output spectrum. Angle-polishing the waveguide facets would remove any contributions from the Fresnel reflections.

3.6 CONCLUSIONS AND FURTHER WORK

From the work presented in this chapter, several important contributions to the field have been made. Firstly, the feasibility of fabricating EDWA devices using ultrafast laser inscription has been further verified by the second demonstration of net gain from a waveguide fabricated using this flexible technique. Furthermore, the multi-scan fabrication technique has been shown to be an invaluable method for tailoring the waveguide cross-section in materials whereby a single un-modified scan approach may not have been able to achieve low waveguide losses. The demonstration of a waveguide laser formed using FBGs as a cavity, albeit with modest output powers, has been the first demonstration of waveguide lasing action in a non phosphate based host. Finally these results prove that Er doped oxyfluoride silicate glass is a viable gain material for producing EDWA and waveguide lasers.

Future progressions for this work can take several routes. Firstly the amount of achievable net gain could be increased by further optimisation of the waveguide fabrication parameters in order to achieve lower losses, along with fabricating waveguides in a longer substrate. This would allow some improvement to the

amount of gain, however much greater progress could be achieved by further optimisation of the substrate composition and dopant concentrations.

Once considerably higher gains are achieved, a wider range of active devices could be fabricated such as high power waveguide lasers, mode-locked waveguide lasers and loss-less splitters.

Overall the work presented has formed the basis for a proof of principle demonstration of the potential for inscribing active devices in Er doped oxyfluoride silicate glasses.

CHAPTER 4 – WAVEGUIDE INSCRIPTION IN BISMUTH DOPED GLASS

4.1 INTRODUCTION

Whilst Rare-Earth ions are able to provide efficient optical gain across many parts of the visible and near IR spectral regions, several large gaps remain which cannot be easily accessed. One particular region that is poorly served by conventional gain media is the spectral region around 1.3 μm. This range is of particular interest for optical telecommunications due to the presence of the natural zero dispersion point of silica fibre. Some RE emission bands do occur in this region such as the $^1G_4 \rightarrow {}^3H_5$ transition in Praseodymium and $^4F_{3/2} \rightarrow {}^4I_{13/2}$ transition in Neodymium, however providing broadband gain in this region is difficult to achieve experimentally.

Bismuth doped glass has emerged as an interesting gain medium, capable of providing an ultra-broad bandwidth of several hundred nanometres in the 1.3 μm region. Combined with the ability to use convenient diode pump laser wavelengths, wide potential exists for the fabrication of a range of active devices based upon this new material. In particular the broad nature of the emission has the potential to greatly increase the data bandwidth available in telecommunications systems, or to provide high brightness broadband light for a wide range of applications such as 3D biomedical imaging using optical coherence tomography. The fabrication of compact integrated active devices based on Bi-doped glass has the potential to offer a low cost approach to broadband optical communications and broadband light sources in the 1.3 μm region.

The work described in this chapter presents an investigation of active waveguide fabrication in Bi-doped glass using ultrafast laser inscription. The substrate material for the initial experiments was designed and fabricated by Professor A. Jha and co-workers at the University of Leeds, and the substrate provided for the latter section of work was developed and fabricated by Dr Y. Fujimoto and co-

workers at the University of Osaka. The waveguide fabrication work was carried out during visits to the Politecnico di Milano under a collaborative research project.

Section 4.2.1 introduces Bi-doped glass as a gain medium, covering the initial work in the field and the origins of the luminescence. This is followed by Section 4.2.2 which details the active devices fabricated using Bi-doped glass as an active medium. Section 4.3 covers the initial waveguide fabrication experiments in a multi-component Bi-doped silicate glass and the subsequent characterisation results. Section 4.4 covers waveguide fabrication and active characterisation work on Bi-doped silica glass provided by the University of Osaka.

4.2 BI-DOPED GLASS AS A GAIN MEDIUM

4.2.1 Origins of luminescence

Fluorescence emission in bismuth doped glasses has been studied extensively in the UV and visible spectral regions [104], however ultra-broadband near infrared luminescence spanning several hundred nanometres in the 1300 nm region from Bi-doped glass was first demonstrated by Fujimoto *et al.* in 2001 [105]. As the spectroscopy of the glass was observed to be considerably different to that of previously investigated materials, the particular form of Bismuth present in the substrate was reasoned not to be due to Bi^{2+} or Bi^{3+} as observed in earlier work. The Bi^{5+} valence state was suggested as a possible candidate for the fluorescence emission.

Further work by the Qiu group was able to demonstrate broadband emission from a wide range of host compositions, such as borosilicates [106], barium-aluminium-borates [107], alumino-phosphates [108] and germanates [109, 110]. In these materials, the authors argued that the luminescence should be due to the low valence states Bi^{+} or Bi^{2+}. This argument was postulated due to the observation of a reduction of the luminescence intensity as the basicity of the host was increased, which is known to follow the trend of the ions preferring higher valence states as the basicity is raised.

Fujimoto *et al.* demonstrated in 2006 the importance of aluminium in the formation of active Bi-centres through structural studies carried out using nuclear magnetic resonance (NMR) techniques [111]. In particular, aluminium in a corundum structure was shown to not only aid the generation of fluorescence through energy coupling, but also to help the incorporation of the Bi into the surrounding glass matrix. The authors observed that at least the two ionic states of Bi^{3+} and Bi^{5+} were present.

A more recent paper by Xia *et al.* in 2006 provides further evidence for the Bi^{5+} valence state as the source of the luminescence [112]. The authors fabricated substrate compositions which preferentially promote the formation of Bi^{5+} valence states by introducing various components such as yttrium and barium into the glass composition. Increasing concentrations caused a corresponding increase in the luminescence.

Fujimoto *et al.* later demonstrated a dramatic 26.3 fold enhancement of the fluorescence intensity in 2007 with the inclusion of a small amount of germanium into the substrate [113]. This suggests that the inclusion of Ge effectively promotes the formation of active Bi centres.

Further work by Okhrimchuk in 2008 demonstrated broad luminescence around 1080 nm in a Bi doped $RbPb_2Cl_5$ crystal [114]. Due to the nature of the crystal, the Bi can only exist in the monovalent form, and so the luminescence is attributed to the Bi^{+} ion. Further support of Bi^{+} as being responsible for the luminescence was shown by Ren in 2008 where comparisons were shown between Bi^{+} and Pb^{0} separately doped into substrates with the same composition [115]. Pb^{0} has the same electronic configuration as Bi^{+}, and correspondingly shows a similar broad emission band in the 1.2 μm region.

More recently, a paper by Sokolov *et al.* in 2008 proposed a radically different form of Bi as responsible for the luminescence [116]. Negatively charged bismuth dimer molecules coupled with six member rings composed of alternating SiO_4 and AlO_4 tetrahedra are put forward as a possible source of emission. Modelling of the structures predicts broad luminescence in the correct spectral

region however further investigation is necessary to fully determine if these structures exist in the substrate.

A recent paper by Peng *et al.* in 2009 proposed that the near-IR luminescence is from an entirely different mechanism. The authors observed that when Bi nano-particles are formed in bismuthate glass, broadband emission in the same spectral region is observed and was suggested to be due to transitions within elementary Bi centres [117]. This adds a further possible mechanism, however whether this mechanism is occurring, or whether nano-particles are present in other Bi-doped substrates remains to be seen.

It is clear that the mechanism for the generation of the broad near infrared emission is currently the subject of considerable debate, and it is possible that several of these forms of Bi are present and are contributing to the observed luminescence.

4.2.2 Active Bi-doped devices

Despite the lack of a fully comprehensive understanding of the luminescence mechanism in Bi-doped glass, several groups have been quick to explore the potential for applications of this novel gain medium. Shortly after the discovery of the near-IR luminescence, in 2003 Fujimoto *et al.* demonstrated bulk gain at 1300 nm from Bi-doped alumino-silica glass when pumped at 810 nm [118]. This was followed in 2005 by the first demonstration of a Bi-doped fibre laser by Dianov *et al.* operating between 1150 and 1300 nm when pumped with a Nd:YAG laser operating at 1064 nm [119]. A demonstration of gain at multiple telecommunications wavelengths around 1300 nm in a bulk sample was shown by Seo *et al.* in 2006 [120], followed by the simultaneous amplification of two wavelengths in a 6.5 cm Bi-doped silica glass rod by the same group in the same year [121].

Dianov *et al.* further demonstrated a high power Bi-doped alumino-silica fibre laser in 2007 giving an output of up to 15 W in the 1150-1215 nm region [122]. The same group in the same year also presented a pulsed fibre laser using Bi-

doped fibre as a saturable absorber for a Yb-doped fibre laser [123]. This unexpected saturable absorption behaviour could open up wider applications of Bi-doped media. A fibre laser with up to 24% slope efficiency was demonstrated by Razdobreev *et al.* in 2007 [124]. Fibre Bragg gratings were used to provide a cavity at 1200 nm.

The first demonstration of gain in a non alumino-silica substrate was demonstrated in 2007 by Ren *et al.* [125]. In this case, a Bi-doped germanate glass was used, providing gain when pumped at the convenient pump diode wavelengths of 808 nm and 980 nm separately. This was followed by the demonstration of gain from a bismuth-doped strontium germanate glass by the same group in the same year [126].

An optical fibre amplifier with 9.6 dB gain at 1310 nm was demonstrated by Seo *et al.* in 2007 [127]. Interestingly the fibre was only 5 cm long, and a total pump power of 100 mW at 810 nm was used. This level of performance is a milestone in the verification that Bi-doped technology has the potential to be used in telecommunications systems.

Further developments in Bi-doped fibre lasers by Dianov *et al.* have demonstrated lasers operating in the 1300-1470 nm region [128], and the 1470-1550 nm region [129], further asserting the versatility of Bi-doped glass to offer such broadband gain in the near infrared.

Mode locking of Bi-doped fibres was first shown by Dianov *et al.* in 2007 [130]. A SESAM was used as one end of a linear cavity in order to provide mode-locking, with a narrow bandwidth FBG forming the other end of the cavity. A train of 50 ps pulses was produced at a repetition rate of 13 MHz. The narrow bandwidth of the FBG limited the authors from achieving shorter pulses. A further paper by the same group in 2008 was able to demonstrate 0.9 ps pulses through the use of a fibre loop mirror instead of the FBG, again with a SESAM providing mode-locking [131]. Most recently the same group employed a chirped FBG in order to provide broadband reflection and dispersion compensation over a 30 nm range, achieving 1.9 ps pulses [132].

These demonstrations confirm the potential for novel active devices based upon Bi-doped substrates. The extreme bandwidths attainable in the near IR combined with the ability to use convenient diode pump wavelengths has wide applications in telecommunications, sensing and imaging.

4.3 WAVEGUIDE INSCRIPTION IN BI:LAZS

4.3.1 Initial fabrication experiments

Samples for waveguide inscription experiments were provided by the University of Leeds Institute for Materials Research. The precursor composition of the glass, known as LAZS, was $50.9SiO_2$ - $25.5Al_2O_3$ - $17Li_2O$ - $5.7ZnO$ - $0.9Bi_2O_3$ (mol %). The fabrication of this host material is described extensively in [133], however the authors incorrectly identified the near IR emission as due to Cr^{4+} ions, when in fact the Bi also present in the sample was responsible. This was highlighted in a comment by Peng *et al.* [134]. In the comment, the same substrate composition was fabricated, both with and without the inclusion of chromium, with both samples showing the same luminescence spectrum. The inclusion of Li_2O and ZnO into the substrate composition was primarily in order to reduce the melting temperature of the glass so that it could be fabricated more easily.

The laser used for the fabrication of waveguides in the Bi-doped LAZS glass was the same cavity-dumped system as described in Section 3.2.5. To fabricate waveguides, the pulse train was focused inside the glass sample to a depth of approximately 150 μm below the surface using a ×50, 0.6 NA microscope objective. The sample was mounted on a set of computer controlled PI (Physik Instrumente) M-511.DD XY motorised translation stages. The sample was then translated in the direction perpendicular to both the laser polarization and propagation direction. The experimental arrangement used for inscribing waveguides was the same as shown in Section 3.3.2. As the optimal fabrication conditions for this substrate material were unknown, a wide parameter range was taken. Pulse energies from 92 to 492 nJ and writing speeds of 3 to 12 mm/s were investigated. Both single and multi-scan fabrication techniques were employed in

order to ascertain which method was most suitable for this substrate composition and fabrication laser. As described in Section 3.3.2, the multi-scan technique is able to correct asymmetry in the waveguide cross-section by building up the refractive index change through multiple passes, each with an increment in position relative to the last. The number of scans and scan spacing for our multi-scan waveguides were chosen in order to fabricate a waveguide approximately 8 μm wide, the same diameter as a standard telecom single-mode SMF-28 fibre. For each pulse energy and writing velocity, waveguides were fabricated using 40 scans with a 0.21 μm separation, 20 scans with a 0.42 μm separation, and a solitary single scan of the same parameters. This enabled the observation of the modification building block that is sequentially written in order to build up the waveguide.

Using equation 4-1 for calculating the Gaussian beam waist of the focussed fabrication beam as shown in [135]:

$$w_y = 2M^2 \frac{\lambda_w n}{\pi NA} \qquad 4\text{-}1$$

where w_y is the beam waist, M^2 is the beam quality parameter, λ_w is the wavelength of the fabrication laser, n is the refractive index of the substrate material, and NA is the numerical aperture of the focussing objective. With M^2 = 1.15, λ_w = 1040 nm, $n \approx 1.5$, and NA = 0.6, the beam waist of the laser beam inside the substrate was calculated to be 2.0 μm. This value is almost 5 times the maximum scan separation used for multi-scan fabrication, therefore ensuring a high degree of overlap between modified regions induced by each successive scan. After fabrication, the sample was diced and polished perpendicular to the waveguide axis, giving a final length of 17 mm.

4.3.2 Waveguide morphology and guided modes

In order to assess the morphology of the fabricated structures, the waveguide cross-sections were imaged on an optical microscope in transmission mode. Figure 4-1 shows facet images of pairs of singlescan and multi-scan waveguides written at the same pulse energy and a translation speed of 3 mm/s.

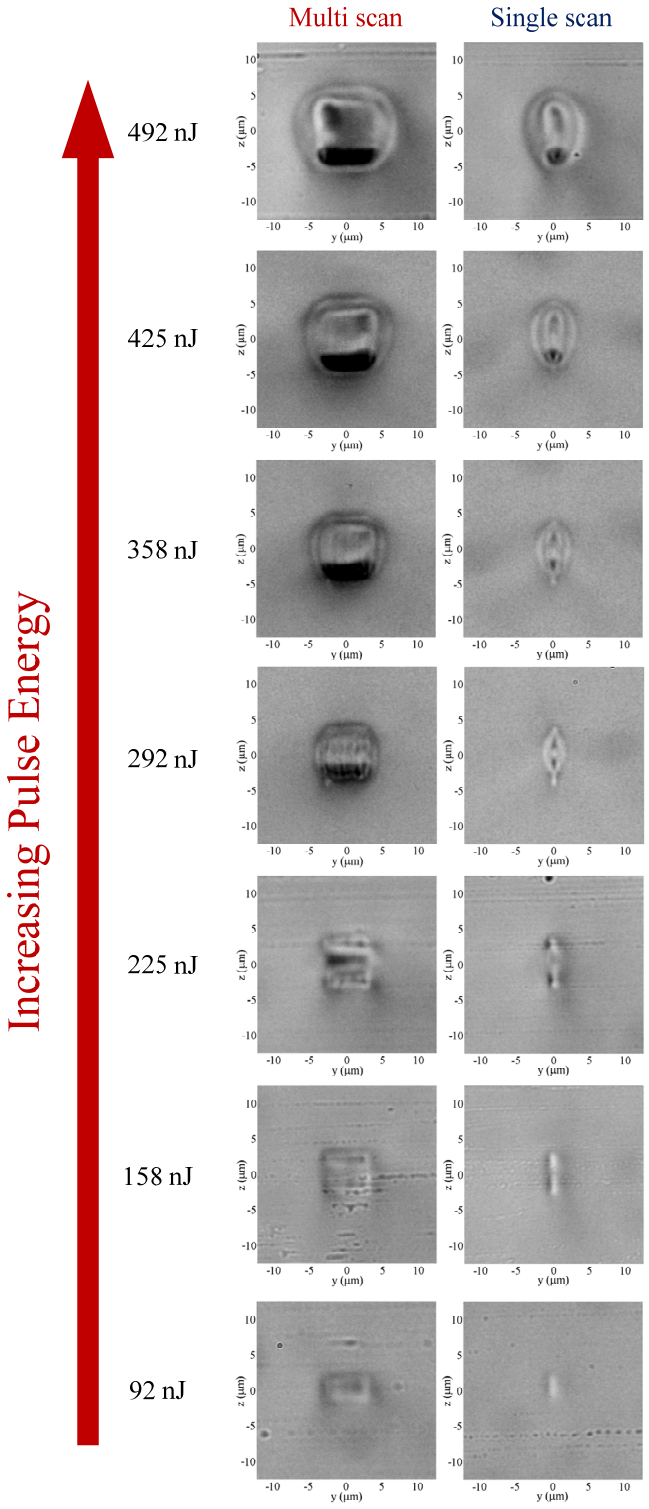

Figure 4-1. Microscope facet images showing the evolution of the waveguide cross section as a function of pulse energy for both single and 20-scan waveguides.

At the lower pulse energies of 92 and 158 nJ, the shape of the single-scan modification was highly asymmetric indicating that minimal thermal accumulation was present. Multi-scan waveguides at the same pulse energies showed a uniform rectangular shaped cross-section. As the pulse energy was increased to 225 nJ, the single scan structure evolved into a shape containing two lobes, with the peak intensity region in the centre capable of driving the thermal accumulation process, facilitating the formation of a wider structure in the centre. Multi-scan waveguides at this pulse energy showed two lobes of smoother index contrast at the top and bottom, with a more weakly modified region in the centre where the thermal accumulation has taken place.

As the pulse energy was increased to and beyond 292 nJ, the waveguide cross-section became dominated by thermal accumulation, generating a much more symmetrical shape with extra internal structure. Multi-scan waveguides at high pulse energies showed significant amounts of optical damage indicated by dark regions on the waveguide cross-sectional image. At the higher pulse energies, the waveguide cross-section becomes considerably wider due to the larger amount of heat deposited through accumulation.

The near-field guided mode profiles of the waveguides were imaged using a fibre coupled super-luminescent light-emitting-diode (SLED) source operating at central wavelength of 1320 nm. The output fibre from the SLED was directly butt-coupled to the waveguide, with the opposite facet imaged onto an Electrophysics 7290A Vidicon camera which was connected to a frame grabber card. The images were gamma corrected and normalised due to the nonlinear response of the Vidicon camera.

Figure 4-2 shows a comparison of the waveguide facet and the near-field guided mode profile at 1320 nm for various multi-scan (a, c, e) and single-scan (g, i) waveguides. A microscope image and near-field guided mode profile of SMF-28 fibre is shown for comparison.

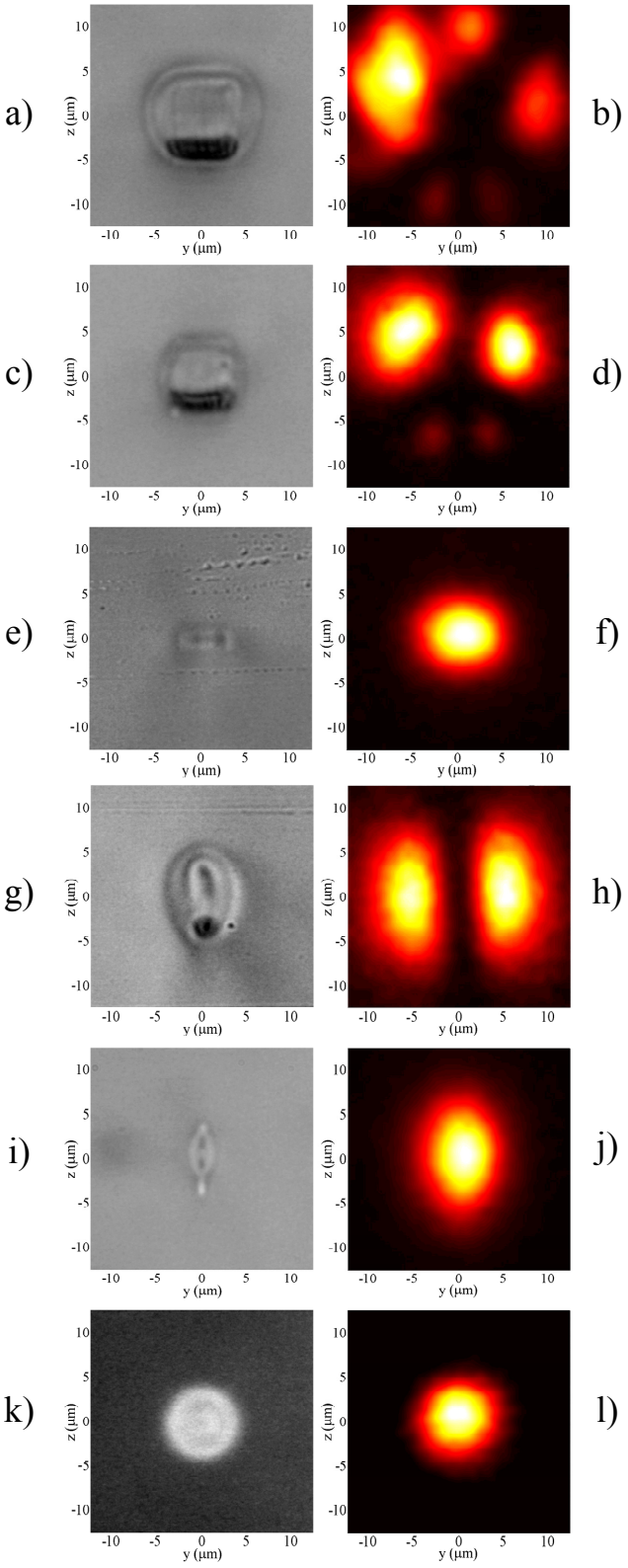

Figure 4-2. Waveguide facet and corresponding guided mode images for various waveguides. SMF-28 fibre is shown for comparison in k) and l).

For high pulse energy single-scan structures, as shown in Figure 4-2 g) and h), a mixture of positive and negative index changes are present, leading to multimode guiding across the entire structure. Several guided mode configurations can be obtained by adjusting the input fibre position, demonstrating a complex refractive index profile. This is in agreement with work carried out by Eaton *et al.*, when fabricating waveguides at similar repetition rates in Corning Eagle-2000 glass [54]. The authors provide measured refractive index profiles for waveguides with very similar shapes and sizes to that shown in Figure 4-2. A sharp and complex combination of positive and negative refractive index changes are shown for such structures.

At lower powers, the single scan waveguides shown in Figure 4-2 i) have too small a refractive index contrast and size to observe the fine guiding features using 1320 nm light, as the structure is single-mode with fairly large and poorly confined mode as shown in Figure 4-2 j).

For multi-scan waveguides, high pulse energies yield a guiding structure that has considerable amounts of negative index change in the centre, surrounded by a ring of positive refractive index change. This can be clearly seen in Figure 4-2 a) to d), where the complex refractive index cross-section allows strong guiding around the structure but none in the centre. At lower pulse energies as shown as e) and f), a single-mode structure is produced, guiding across the whole of the modified region.

From the observed guided mode profiles and microscope images, it appears that for multi-scan waveguides, low pulse energies generate smooth, well structured refractive index profiles suitable for low-loss guiding. For single-scan structures, a relatively high pulse energy regime appears to be more optimal. Pulse energies between those observed in Figure 4-2 g) and i) would enable well-confined single-mode guiding without any fine modal structure from the complex refractive index profile.

4.3.3 Loss characterisation

The insertion losses of the fabricated waveguides were measured using the same technique as described in Section 3.3.4. The characterisation was carried out using an Exalos SLED source operating at a central wavelength of 1320 nm. The sample was mounted on an x-y-z translation mount with tip and tilt angular control. A reference measurement was taken through a signal path composed of a single SMF-28 fibre, which was connected to an Advantest Q8384 optical spectrum analyser. The fibre was broken, cleaved and butt-coupled up to the waveguide under test using index matching fluid. The total insertion loss (IL) is defined as the difference between the reference measurement through the fibre and the signal through the waveguide. As unlike in Er-doped substrates, Bi-doped glass does not have any ground state absorption in the near infrared, the CL and PL can be simply obtained from the IL.

Waveguide coupling losses (CLs) were measured as described in Section 3.3.4. The CL is defined as the difference between the signal obtained when a multi-mode fibre is used to collect the output of the waveguide, to a single-mode fibre at the output. The propagation loss (PL) is defined as the total coupling losses subtracted from the total insertion loss divided by the sample length. Figure 4-3 shows the IL, CL and PL for single-scan waveguides. The lines are included as a guide to the eye.

The possible error in the IL measurements is estimated to be ~0.3 dB due to alignment accuracy. The error in the CL measurement is estimated to be ~±0.2 dB also due to alignment accuracy. The error is the PL measurement estimated to be ~±0.2 dB/cm. The origins of propagation losses can be attributed partly to glass inhomogeneities and partly to non-uniformity in the sample translation movement and scattering or absorption centres present in the modified regions.

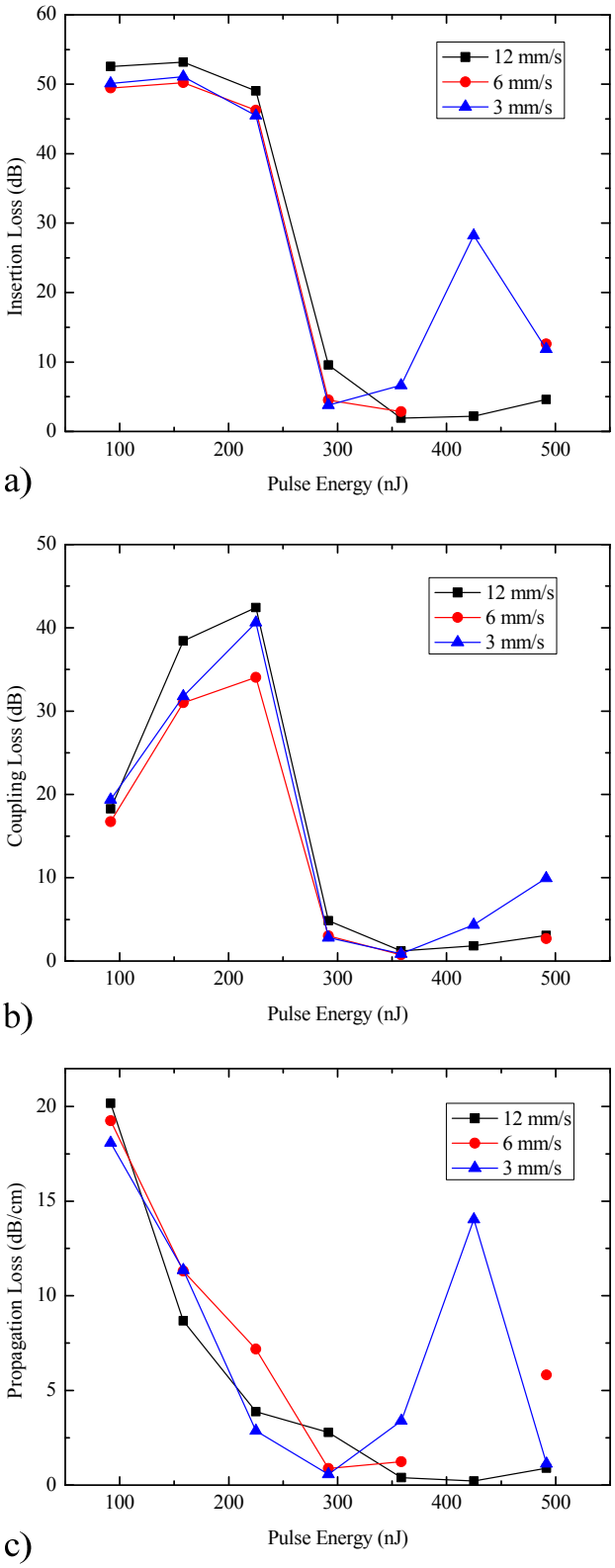

Figure 4-3. Loss measurements for single-scan waveguides. a) Insertion loss, b) Coupling loss per facet, c) Propagation loss per unit length.

From Figure 4-3 a), it is clear that higher pulse energies demonstrate a regime of low insertion loss guiding. At the lowest pulse energy of 92 nJ, the mode supported by the waveguides is poorly confined, suffering from very high PLs due to radiation losses and micro-bending. As the pulse energy is increased to 158 nJ and further to 225 nJ, the guided mode becomes more well confined, however due to the highly asymmetric cross section in this regime, the CLs are high. At higher pulse energies, the waveguide cross section is much more symmetrical, with enough refractive index change to support a well confined mode, resulting in low ILs. The CL rises at very high pulse energies combined with slow speeds due to a large waveguide cross-section combined with a large index change. This results in multi-mode guiding, and a corresponding increase in the CL. The point missing in the 6 mm/s plot and anomalous point in the 3 mm/s plot in Figure 4-3 are due to disruptions in the waveguides caused the presence of a bubble in the substrate. Figure 4-4 shows the IL, CL and PL for 40-scan waveguides. The lines are shown as a guide to the eye.

From the ILs shown in Figure 4-4 a), a low insertion loss regime is present at low pulse energies. At the highest pulse energies, strong guiding occurs around the modified region resulting in low CLs, however significant amounts of optical damage is present resulting in high PLs due to scattering. Little variance is observed between translation speeds in the low IL region, indicating that refractive index saturation has occurred, with slower speeds unable to induce a higher index change.

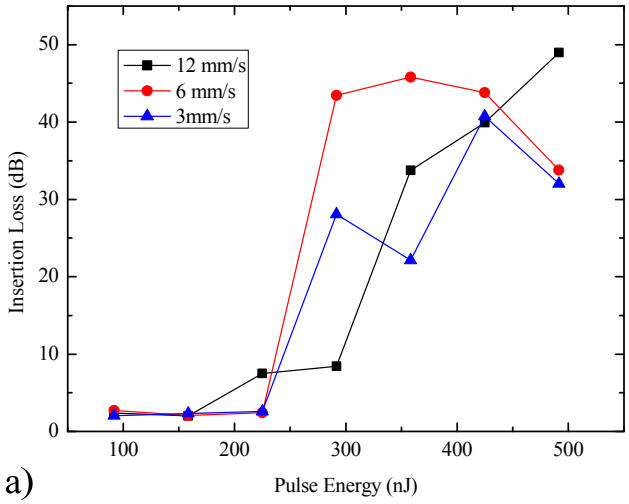

a)

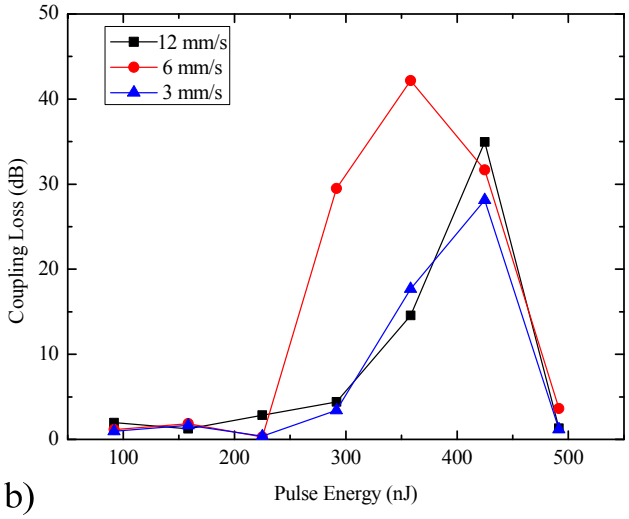

b)

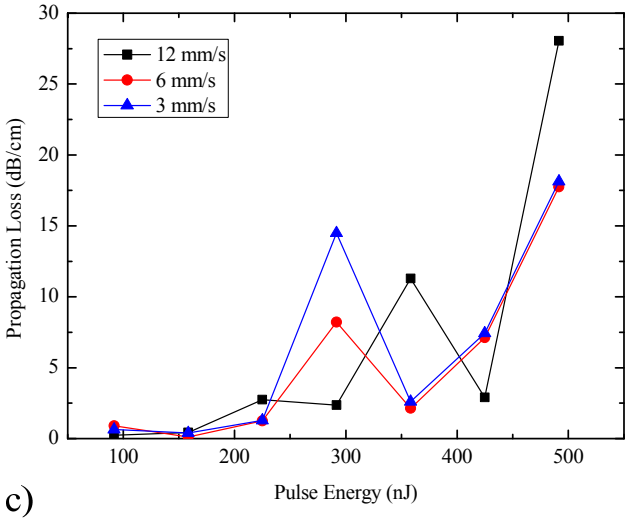

c)

Figure 4-4. Loss measurements for 40-scan waveguides. a) Insertion loss, b) Coupling loss per facet, c) Propagation loss per unit length.

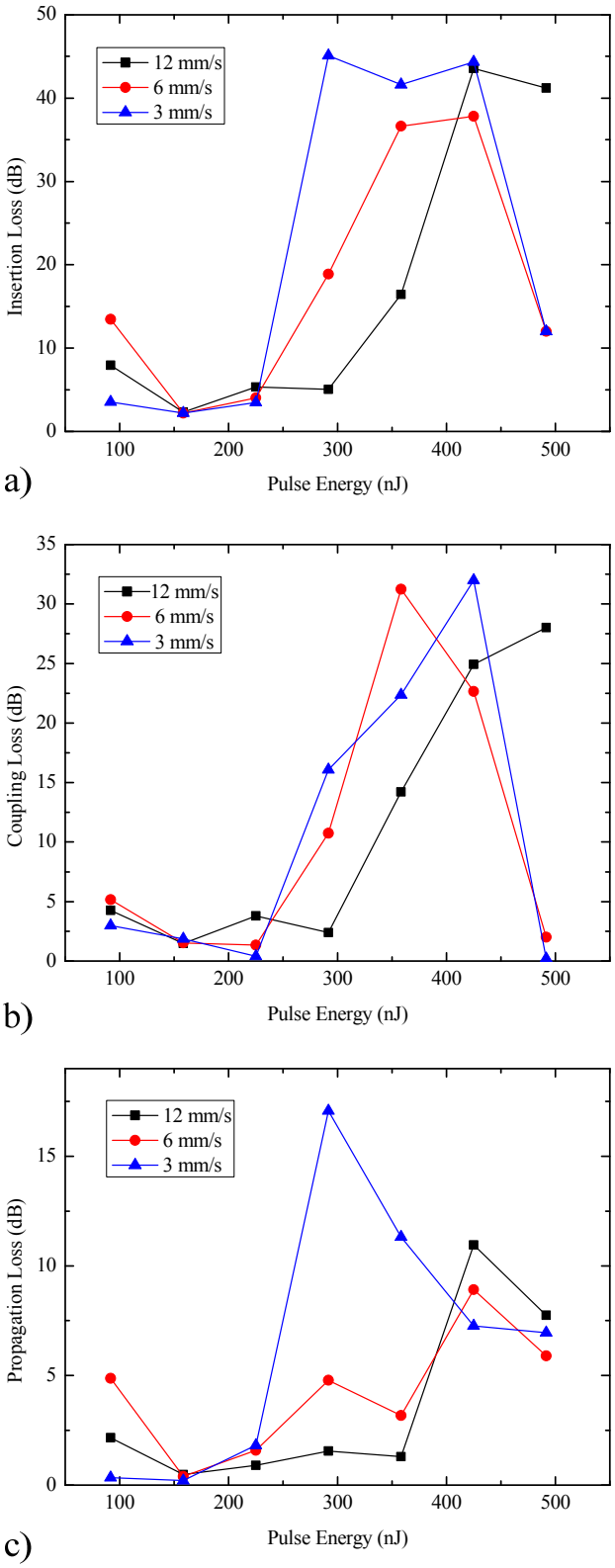

Figure 4-5. Loss measurements for 20-scan waveguides. a) Insertion loss, b) Coupling loss per facet, c) Propagation loss per unit length.

Figure 4-5 shows the IL, CL and PL for 20-scan waveguides. The lines are shown as a guide to the eye. The IL results shown in Figure 4-5 present a slightly different picture to waveguides fabricated with 40-scans. Again, a low loss regime is present at lower pulse energies, particularly at a pulse energy of 158 nJ. In contrast to the trend observed for 40-scans, a large variance is visible between translation speeds indicating a lower amount of saturation in the refractive index change. At very high pulse energies, low coupling losses are observed for slow translation speeds due to strong guiding around the damage regions. Propagation losses for the slowest translation speed of 3 mm/s are particularly high in the intermediate pulse energy regime. This is due to a large amount of optical damage present, combined with a high amount of mode overlap with this damaged region.

Overall it was found that both single- and multi-scan fabrication were capable of producing low loss waveguides. The lowest loss single-scan waveguide yielded a total fibre to fibre insertion loss of 1.9 dB, with a coupling loss of 0.6 dB/facet, and a propagation loss of 0.4 dB/cm. The lowest loss multi-scan waveguide had a total insertion loss within error of the single-scan waveguide, with an IL of 2.0, a CL of 0.6 dB/facet and a PL of 0.3 dB/cm. The Polarisation dependant loss (PDL) was measured for the optimal multi-scan and single-scan waveguides, using a HP 11896A polarisation controller and a linearly polarised 1320 nm laser source. The PDL was measured to be 0.4 dB and 0.6 dB for the optimal single-scan and multi-scan waveguides respectively. The PDL values are small enough to indicate that the waveguide birefringence is insignificant.

4.3.4 Refractive index profiling

In order to gain further insight into the waveguide structure, the refractive index profiles were measured using the refracted near-field (RNF) technique. The RNF technique was initially developed for providing refractive index profiles of optical fibres and performs [136]. The technique involves focusing a beam onto the waveguide facet with a high numerical aperture. Light that is not guided by the

waveguide refracts out of the surrounding substrate and is captured onto a detector which has a half-disk shaped mask placed in front. Figure 4-6 shows a schematic diagram of the RNF technique, adapted for obtaining refractive index profiles of silica-on-silicon waveguides [137].

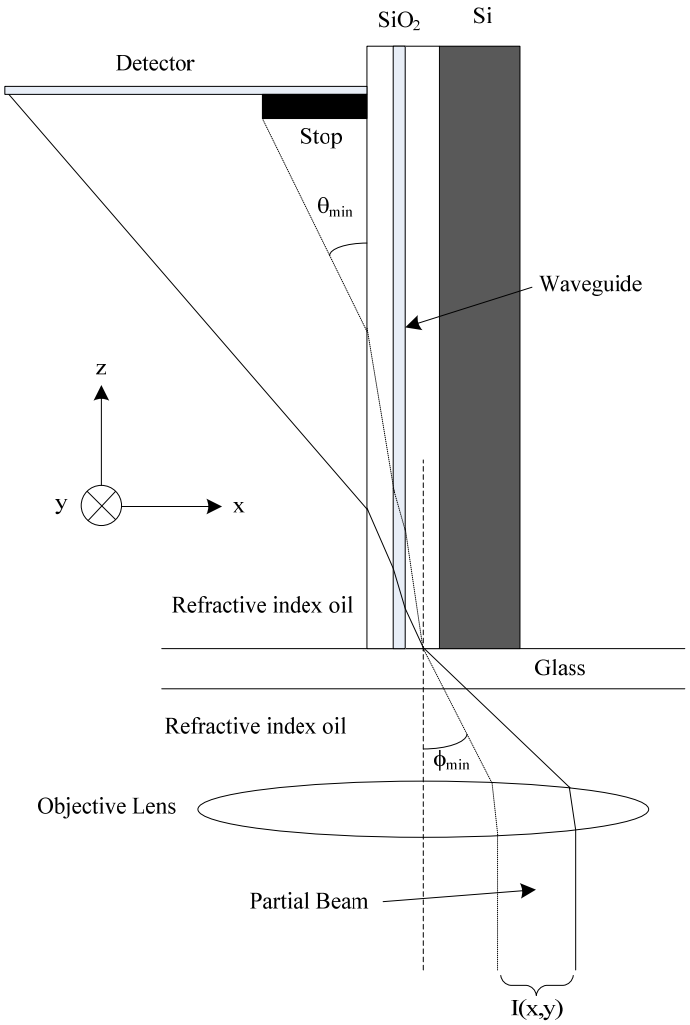

Figure 4-6. Schematic diagram of RNF profilometry, adapted for profiling silica-on-silicon waveguides [137].

The sample and detector assembly is placed on a computer controlled translation stage, allowing the focus to be scanned across the sample. A detector is placed behind a half-disk shaped beam stop, allowing the measurement of the amount of light refracted through the sample at an angle greater than θ_{min}. The minimum incident angle reaching the detector φ_{min} and therefore the amount of light

measured by the detector is dependent upon the refractive index at the focus, allowing the refractive index profile to be obtained by scanning the focus across the waveguide facet.

The RNF profiler used to analyse the waveguides was a commercial system (Rinck Electronik, Germany), utilising a laser wavelength of 658 nm. The system has a spatial resolution of 0.5 μm and a refractive index resolution of 10^{-5}. The system is also capable of working at a wavelength of 1550 nm, however the spatial and index resolution are significantly compromised, so the visible wavelength was used. The lowest insertion loss single-scan and multi-scan waveguides were aligned and profiled using the Rinck system. Figure 4-7 shows microscope facet images, refractive index profiles and near field guided mode images of the two waveguides.

From Figure 4-7, the shape of the refractive index profile can be seen to follow the general form of that visible on the microscope images, however some distortion to the shape is present due to refractive index inhomogeneities in the substrate. As the light reaching the detector in the RNF profiler has to first pass through significant amounts of substrate material, any refractive index inhomogeneity present will cause a shift in the diverted angle and therefore in the amount of light reaching the detector. Despite the slight distortion to the shape, the peak magnitude of the refractive index change was measured to be considerably higher for the single-scan waveguide ($\Delta n = 4.3\times10^{-3}$) compared to the multi-scan waveguide ($\Delta n = 2.6\times10^{-3}$). This difference in magnitude may be due to the large difference in fabrication pulse energy between the optimal single-scan waveguide (358 nJ) and optimal multi-scan waveguide (158 nJ). The index contrast for the optimal multi-scan waveguide appears to be saturated, as the insertion loss for the waveguide fabricated using the same pulse energy and translation speed, but with only 20 fabrication scans was merely 0.3 dB greater.

The small decrease in insertion loss by using 40-scans may be the result of a more homogeneous cross section as a result of either or both increased overlap between successive modified regions or a reduction in scattering centres as a result of increased annealing by successive scans. The higher pulse energy used during the

single-scan fabrication may induce a different index modification regime, whereby the high pulse energy can cause greater modification effects such as considerably stronger thermal gradients.

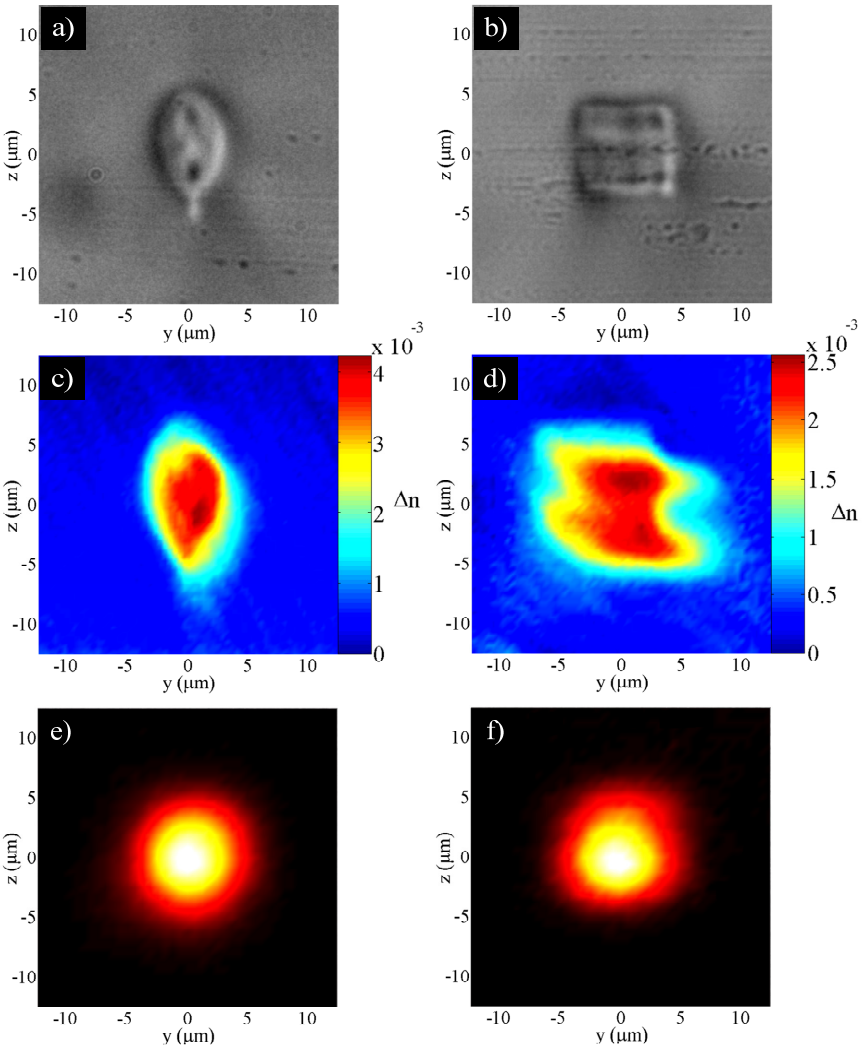

Figure 4-7. a), b) Optical microscope images of waveguide facets taken in transmission mode, c) d) refractive index profiles, e) f) near field guided mode profiles taken at 1320 nm. a) c) e) Lowest insertion loss single-scan waveguide, b) d) f) Lowest insertion loss multi-scan waveguide.

Interestingly, the refractive index profile of the multi-scan waveguide shows a peculiar shape with two lobes above and below. The refractive index profile of the single-scan building block used to fabricate the multi-scan waveguide was

measured using the same experimental setup. Figure 4-8 shows the microscope facet image and corresponding refractive index profile of the building block.

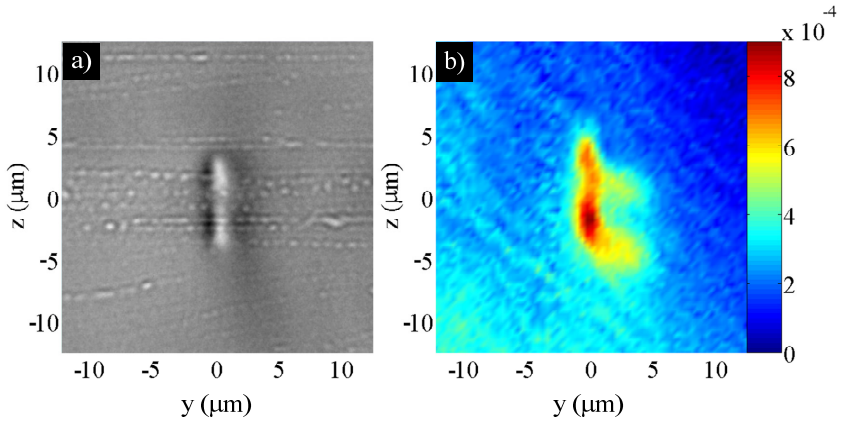

Figure 4-8. a) Optical microscope image of the waveguide facet, b) refractive index profile.

From Figure 4-8, the building block of the multi-scan waveguide can be seen to show the same two lobed appearance. This is likely due to the onset of some thermal accumulation at the region with highest intensity during fabrication, showing similar behaviour to that observed in Figure 4-1 earlier. At a slightly lower pulse energy, the two lobed structure would form a single line of refractive index modification. The magnitude of the index contrast for the building block is measured to be relatively small at $\Delta n = 9\times10^{-4}$, however due to convolution effects of the point spread function of the focussed laser beam in the profilometer, the index contrast may well be slightly greater than measured. The dimensions of the building block are approximately 10 μm in the z-axis, and 2.5 μm in the y-axis. These values are considerably larger than the quoted spatial resolution of the Rinck profiler, however the material inhomogeneities present may reduce the effective spatial resolution.

4.3.5 Fluorescence measurements

In order to assess the active capabilities of the waveguides fabricated in the Bi-doped LAZS glass supplied by Leeds University, the fluorescence emission of the

waveguides was measured. The fluorescence was measured by pumping the waveguide under test using a fibre coupled single-mode 810 nm pump laser emitting up to 60 mW, and separately using a 980 nm single-mode pump laser with up to 220 mW of output power. Upon pumping, a clear orange-yellow emission was visible along the length of the waveguide. Figure 4-9 shows a photograph of the lowest insertion loss multi-scan waveguide pumped from the right hand side with 220 mW at 980 nm. This orange-yellow upconversion could be due to emission from Bi^{3+} ions present in the material, which are known to give fluorescence in the visible spectral region [104].

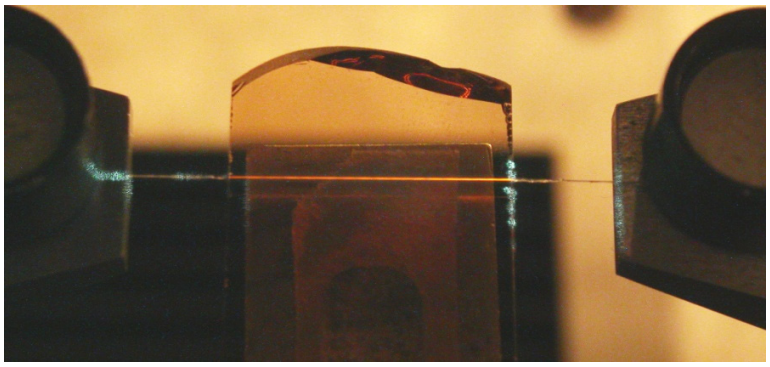

Figure 4-9. Photograph of visible upconversion visible from the waveguide under pumping.

Fluorescence measurements were conducted by optically pumping the waveguide under test with either the 980 nm light or the 810 nm light, using direct fibre-waveguide butt-coupling. The generated fluorescence was then collected at the opposite end of the waveguide using an SMF-28 fibre directly butt-coupled to the waveguide facet. The collected light was then collimated and passed through two silicon pump blocking filters and refocused back into an SMF-28 fibre, which was then connected to an Advantest Q8384 optical spectrum analyser with a resolution set to 0.5 nm. The two pump blocking filters were necessary to completely block the pump light. Figure 4-10 shows the fluorescence emission observed for both the lowest insertion loss single-scan waveguide and multi-scan waveguide at both 980nm and 810 nm pumping.

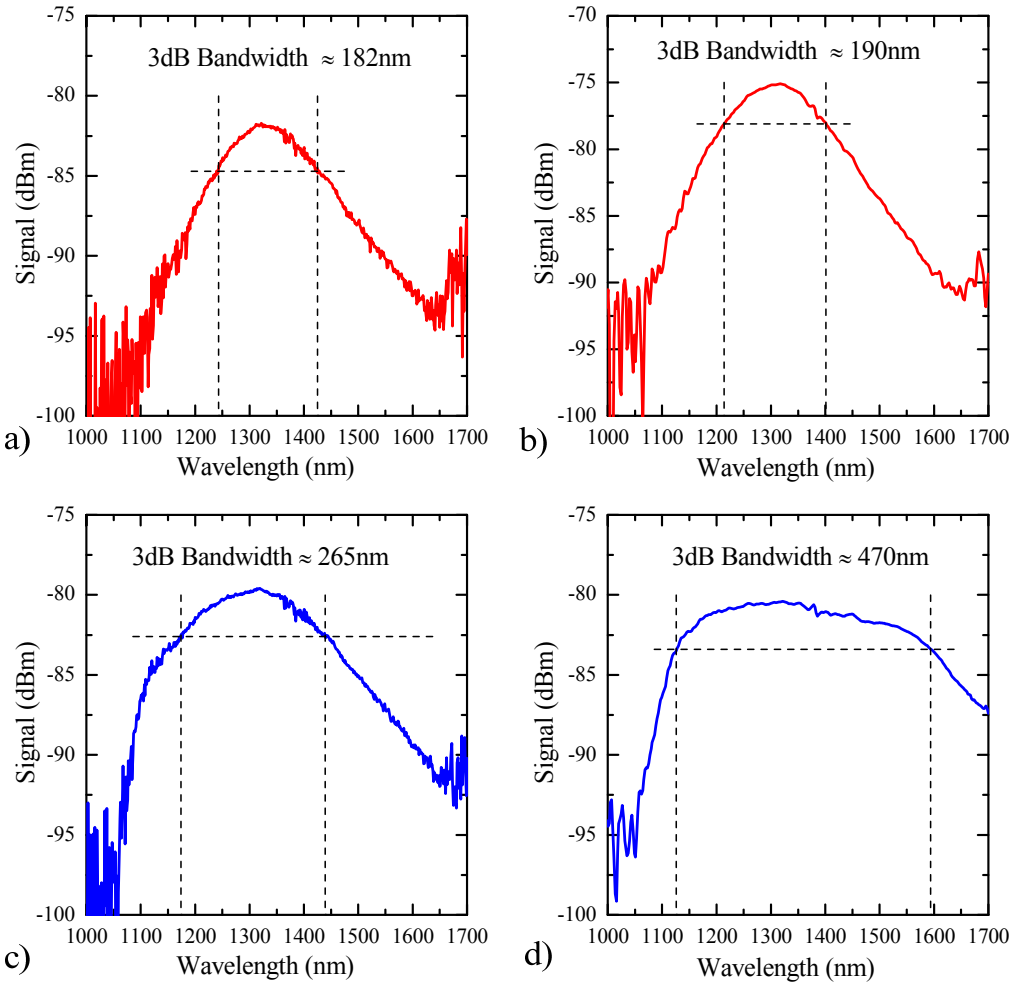

Figure 4-10. a), c) Fluorescence emission for the lowest IL multi-scan waveguide. b), d) fluorescence emission from the lowest IL single-scan waveguide. a) and b) were pumped with 60 mW at 810 nm, c) and d) were pumped with 980 nm.

From Figure 4-10 it can be seen that a maximum 3 dB fluorescence bandwidth was measured to be approximately 470 nm under 980 nm pumping. The shape of the fluorescence emission when pumped at 810 nm is similar for both the single- and multi-scan waveguides, however when pumped at 980 nm, the single-scan waveguide shows a much broader bandwidth. This may be due to the stronger refractive index change allowing stronger guiding of longer wavelengths, resulting in more signal being guided and detected on the OSA.

Currently, the origin of the fluorescence broadening is not fully understood, and is the topic of considerable debate. The shape, width and spectral position of the fluorescence spectra measured are considerably different to that observed in other work. The peak position of the fluorescence has also been shown to change for different pump wavelengths as shown in [107] and [138]. For example, Suzuki *et al.* in [138] observed a shift in the peak from 1250 nm when pumped at 800 nm to 1100 nm when pumped at 974 nm, and a decrease in the bandwidth from 440 nm under 800 nm pumping, to 290 nm under 974 nm pumping. In stark contrast to this report, the observed fluorescence spectra are unchanged in the peak position of 1320 nm for both 810 nm and 980 nm pump wavelengths, and an increase in bandwidth was observed from 200 nm under 810 nm pumping, to approximately 500 nm under 980 nm pumping for the single-scan waveguide, and an increase from 182 to 265 nm for the multi-scan waveguide at 810 and 980 nm respectively.

4.3.6 Gain measurements

The fluorescence bandwidth observed when the waveguides were pumped is particularly promising for the fabrication of optical amplifiers and lasers, however in order to fully quantify the device performance, measurements of the gain are required. Figure 4-11 shows the setup used to carry out gain measurements. The gain was measured using two Exalos SLED sources operating at 1320 nm and 1410 nm. The SLEDs were connected to an optical switch and into a 90/10 directional coupler to provide a 10% tap in order to monitor the signal powers. The 90% port was fed into an 810/1300 nm wavelength division multiplexor (WDM) and then directly butt coupled to the waveguide under test. The output was connected to a second 810/1300 nm WDM through which the 170 mW pump laser was coupled. The 1300 nm port of the WDM was fed into an optical switch and then into an Advantest Q8384 optical spectrum analyser. The relative gain was measured using the same technique as described in Section 3.4.1. Initially, the fibres were accurately aligned to the waveguide. The signal spectrum after travelling through the entire system is then captured. The pump laser was then enabled, and the throughput spectrum is again measured, giving the combination

of signal, fluorescence and gain. The signal source is then disabled with the pumps remaining on, and the fluorescence spectrum is then recorded.

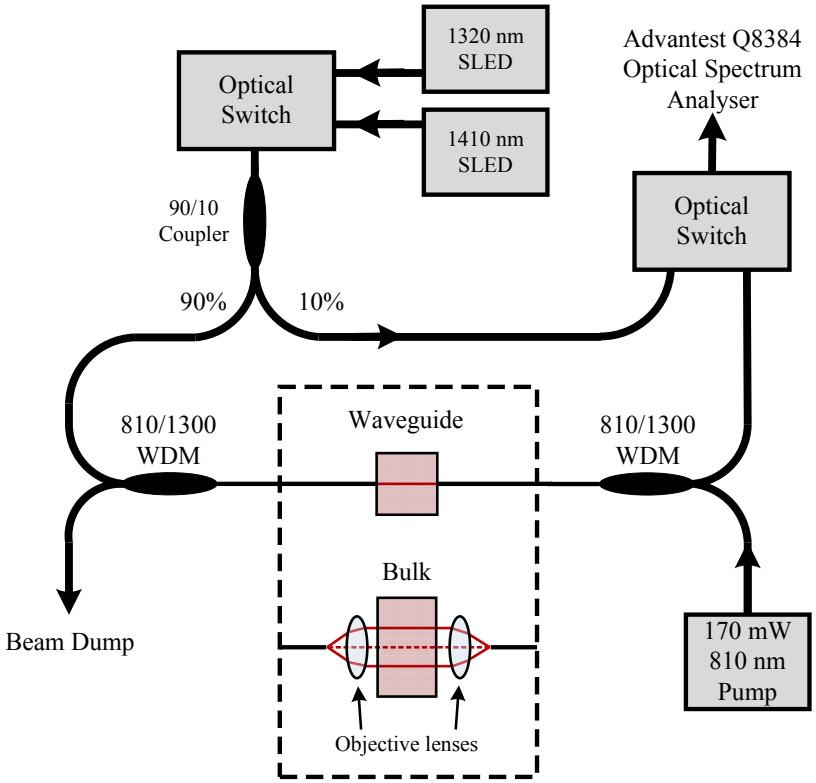

Figure 4-11. Experimental setup for gain measurements.

No relative gain could be measured from the waveguides. This may be due to the inscription process itself modifying the gain properties of the substrate, or alternatively the substrate itself may not be capable of providing gain. In order to fully ascertain the origin of this phenomenon, a gain measurement of the bulk material was carried out as a direct comparison. Figure 4-11 also shows the experimental arrangement used for bulk gain measurements. Two microscope objective lenses were used in order to collimate and refocus the light back into the fibre after passing through the sample. Figure 4-12 shows a comparison of the fluorescence and relative gain results for the optimal single-scan waveguide and the bulk when pumped at 810 nm. Index matching fluid could not be used for the direct fibre butt-coupling, due to the high absorption at 170 mW of 810 nm pumping, causing total destruction of the fibre end from the rapid heating.

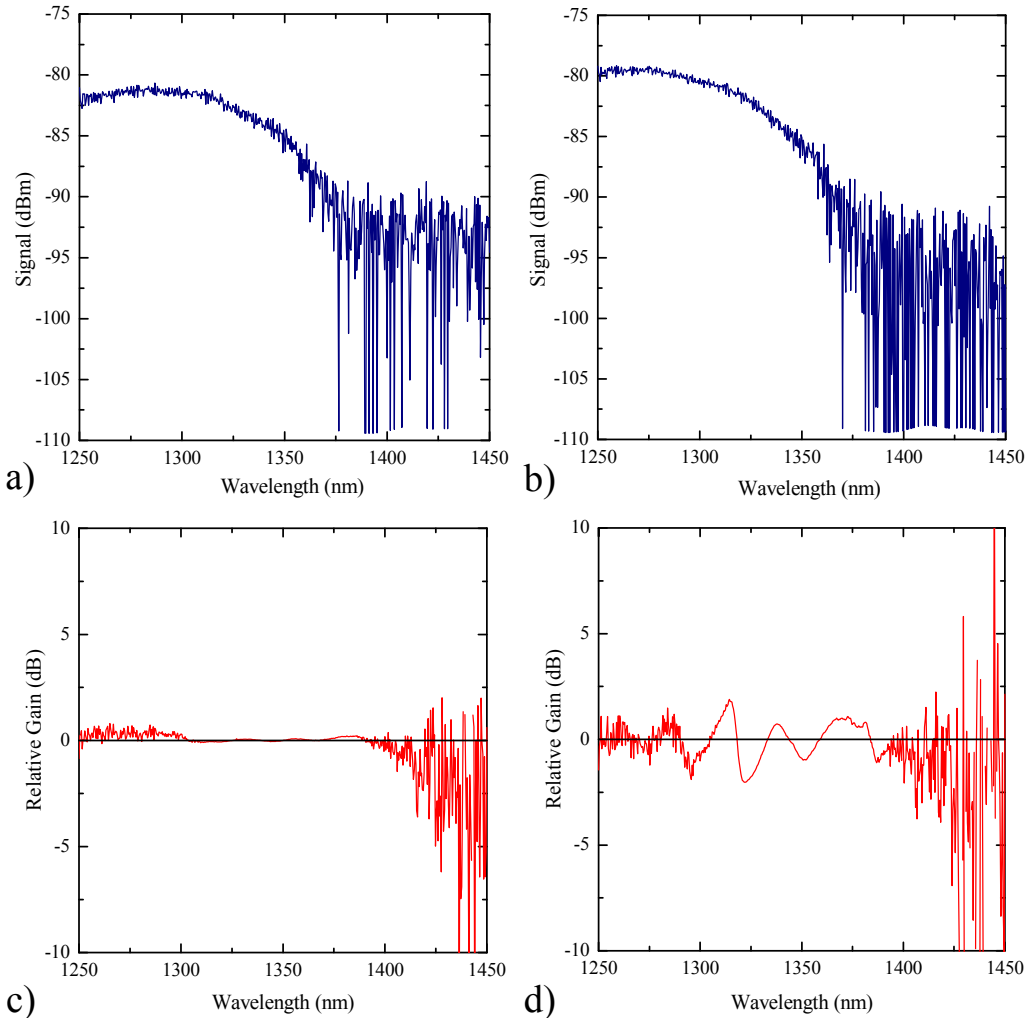

Figure 4-12. Comparison of the fluorescence - a) & b), and relative gain - c) & d) for the bulk sample - a) & c), and lowest IL single-scan waveguide - b) & d).

From Figure 4-12, it is clear that no gain is observed for both waveguide and bulk, yet the fluorescence is preserved. The lack of index matching fluid is responsible for the fringes observed in Figure 4-12 d), due to a small thermally induced change in the fibre to waveguide distance when the pump laser is enabled. The lack of gain yet preservation of fluorescence would indicate that the substrate material is incapable of providing gain. Interestingly, a publication by Zhou *et al.* in Applied Physics Letters, published after this work was carried out, provides interesting insight [139]. As a small addition to the publication, the authors fabricate Bi-doped LAZS substrates and perform gain measurements on the substrates. In agreement with the measurements shown here, no gain was

observed from the bulk substrates. The authors state that the inclusion of the alkaline oxides ZnO and Li_2O, which are present to reduce the glass melting temperature, effectively destroy the gain properties of the material. The authors suggest the mechanism is due to the inclusion of these components increasing the basicity of the glass, which reduces the efficient formation of low-valence state ions indicating that a reduction in Bi^+ centres could be occurring. Nevertheless from a device perspective, the lack of achievable gain is catastrophic and in order to fabricate a working Bi-doped waveguide amplifier, the material composition needs to be modified.

4.4 WAVEGUIDE INSCRIPTION IN BI:ALUMINO-SILICA

4.4.3 Substrate material provided by Osaka University

In view of the lack of gain available from the Bi:LAZS substrate material presented earlier, a proven material was sought. A simpler glass composition without the alkaline oxide modifiers was provided by the University of Osaka. The glass used was that shown by Y. Fujimoto to give the first demonstration of optical gain from a Bi-doped glass in 2003 [105]. The precursor composition of the substrate glass was $92.0SiO_2$ - $7.0Al_2O_3$ - $1.0Bi_2O_3$ (mol%). The mixture was sintered at a temperature of 1760^{o}C, slightly higher than the 1600^{o}C used in the preparation of Bi-doped LAZS glass. The sample provided was diced and polished to give a final sample length of 5 mm.

In order to study the fluorescence emission of the bulk glass, the fluorescence spectra of the sample was measured. This was carried out by pumping the sample with 190 mW at 810 nm and separately with 600 mW at 980 nm. Both pump lasers were single-mode fibre delivered, with the fluorescence emission collected with a 100 μm core multimode fibre at 90 degrees to the input fibre. The output from the multi-mode fibre was connected to an Ando AQ6317 Optical Spectrum Analyser. Figure 4-13 shows the obtained fluorescence spectra.

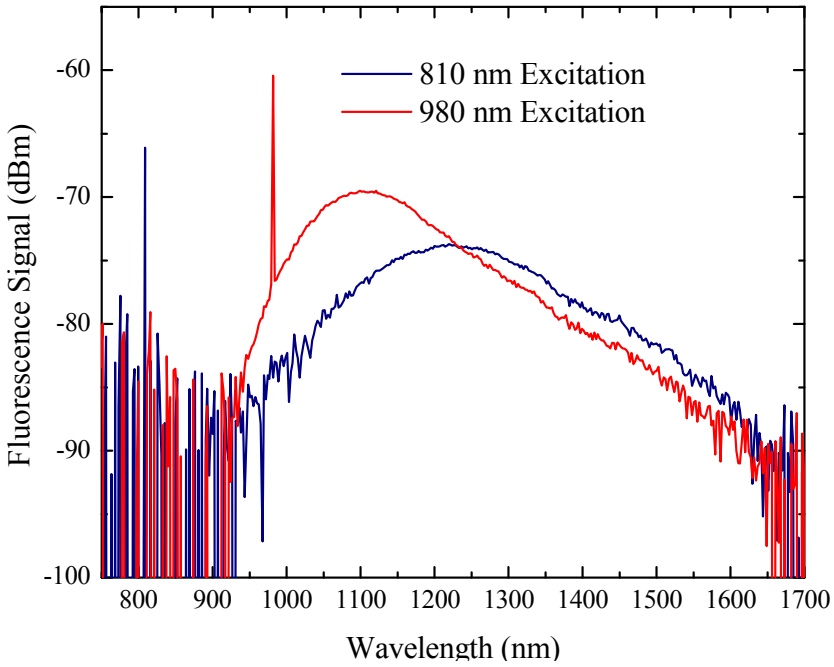

Figure 4-13. Bulk fluorescence spectra for Bi-doped alumino-silica glass pumped with up to 190 mW at 810 nm and 600 mW at 980 nm.

From Figure 4-13 the fluorescence emission band is located at shorter wavelengths for pumping at 980 nm compared to 810 nm excitation. The bandwidth of the emission is also narrower at approximately 180 nm for 980 nm pumping compared to approximately 250 nm for 810 nm pumping which is in sharp contrast to the trend observed in Bi-doped LAZS glass.

4.4.4 Waveguide fabrication

The laser system used for waveguide inscription was the same Yb-doped cavity dumped oscillator used in the previous substrates, however the phosphate glass gain medium had been replaced with an Yb-doped KGW tungstate crystal. This allowed an increase in the total available pulse energy to approximately 1.5 μJ whilst maintaining the same pulse duration of 300 fs and the same repetition rate capabilities. As the optimal parameters for this substrate material were unknown, a very wide range was taken with pulse energies of 108, 180, 300, 500, 681 and 851 nJ. Both single and multi-scan fabrication methodologies were investigated,

with translation speeds of 1, 3 and 9 mm/s for multi-scan and 0.1, 0.3, 1, 3, and 9 mm/s for single-scan waveguides. For multi-scan waveguides, 20 fabrication scans were used due to the small variance between 20 and 40 scan waveguides observed in previous substrate materials. A scan spacing of 0.4 μm was employed in order to build up a waveguide with an approximate diameter of 8 μm. After fabrication, the waveguide facets were ground back and polished to an optical finish.

4.4.5 Waveguide morphology

After fabrication, the waveguides were observed on an optical microscope in transmission mode. Waveguides fabricated using pulse energies of 108 and 180 nJ did not show any visible modification under the microscope indicating that a threshold for strong modification exists between 180 and 300 nJ. Figure 4-14 shows microscope facet images for various structures. All structures fabricated with a pulse energy of 300 nJ and above show some damage present, indicated by dark regions on the microscope facet images.

At the lowest visible pulse energy of 300 nJ, the single-scan structure shown in Figure 4-14 b) has the form of a single line of modification, with damage present at the top of the structure. The multi-scan structure of the same parameters shown in Figure 4-14 a) shows the same pattern, with strong damage present at the top of the structure and some refractive index modification below. As the pulse energy is increased to 500 nJ as shown in c) and d), the aspect ratio of the single-scan is reduced, indicating the onset of some thermal accumulation, however the amount of damage occurring is also increased dramatically. As the pulse energy is further increased to 681 and 850 nJ, the structure becomes predominantly dark damaged regions. The aspect ratio of the single-scan structure is also reduced due to greater thermal accumulation, however this is of limited used due to the amount of damage present.

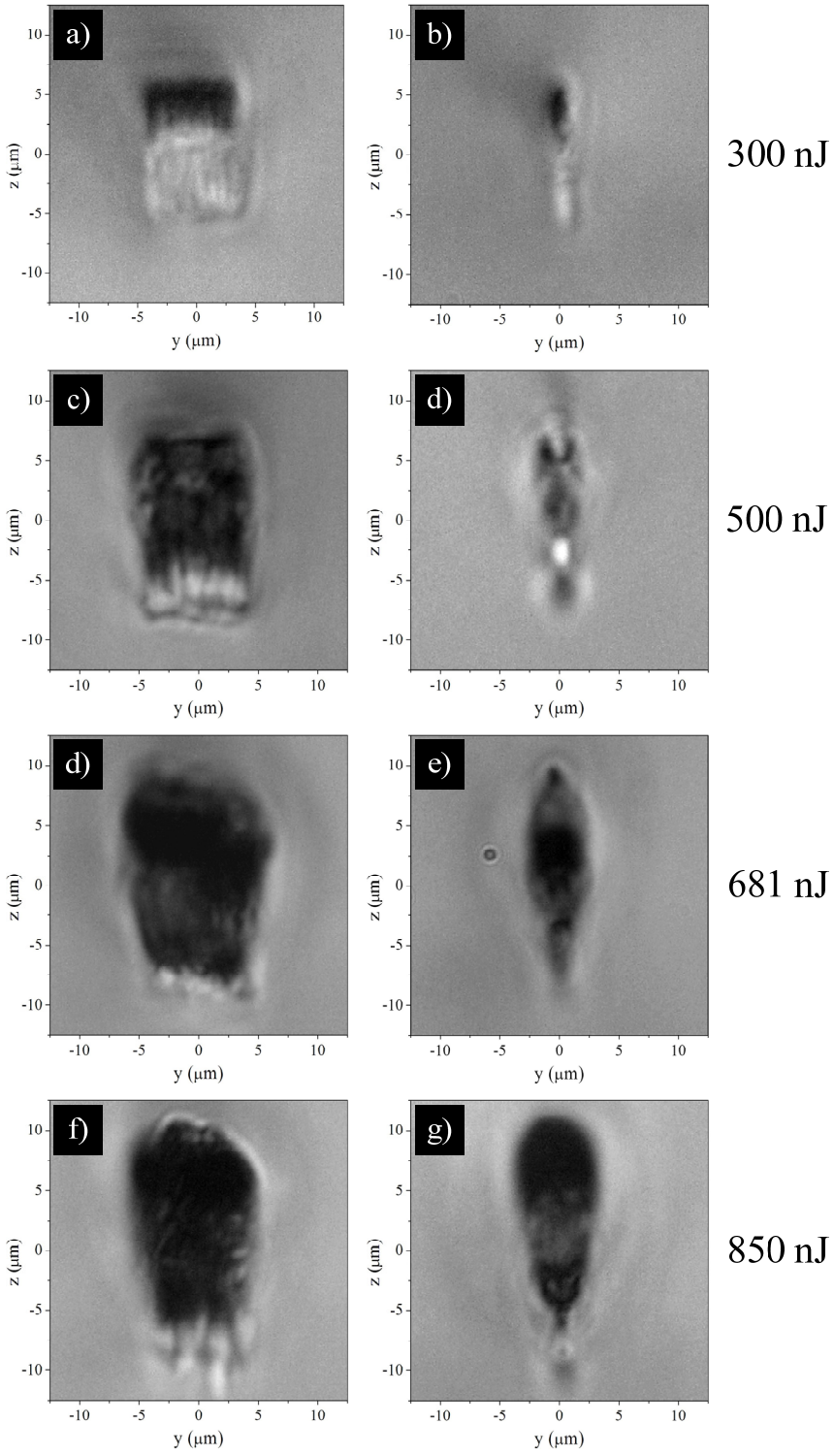

Figure 4-14. Microscope facet images for various structures. The left column shows multi-scan structures, the right column single scan structures for the same pulse energy and translation speed. All structures shown were fabricated with a translation speed of 1 mm/s.

The form of the dark regions induced at high pulse energies may be from the combination of micro-voids, strong absorption from colour centres and some negative refractive index changes. The effect of changing the translation speed is considerably less pronounced than altering the fabrication pulse energy, however less modification is observed for higher translation speeds.

4.4.6 Guided mode profiles

The near-field guided mode profiles of the waveguides were observed by coupling 1320 nm light from a broadband fibre coupled SLED into the waveguide and imaging the exit facet with a 0.65 NA microscope objective mounted on an Electrophysics 7290A Vidicon camera which was connected to a frame grabber card. The images were gamma corrected and normalised due to the non-linear response of the Vidicon camera. Figure 4-15 shows microscope facet images and corresponding near-field guided mode profiles of the waveguides at 1320 nm.

Due to the large amount of damage present on the fabricated structures, only a few waveguides were able to guide enough light to be clearly visible on the camera. Of the waveguides that were visible, strong refractive index changes were observed. The form of the induced refractive index changes may include negative as well as positive changes, indicated by the shape and size of the guided mode relative to the microscope facet image as observed in Figure 4-15 a) and b).

Only a couple of multi-scan waveguides were capable of guiding enough light to be visible on the camera. Very weak guiding was observed from the multi-scan waveguide fabricated with a pulse energy of 180 nJ and the slowest translation speed of 1 mm/s, even though this structure was not visible on the microscope. This is indicative of the very small refractive index change induced at this pulse energy. The guiding was not strong enough to capture a reliable image, however guiding was present as observed later. The presence of a refractive index change at this low pulse energy may indicate that damage free guiding may be obtainable with a slow enough translation speed and a more refined pulse energy.

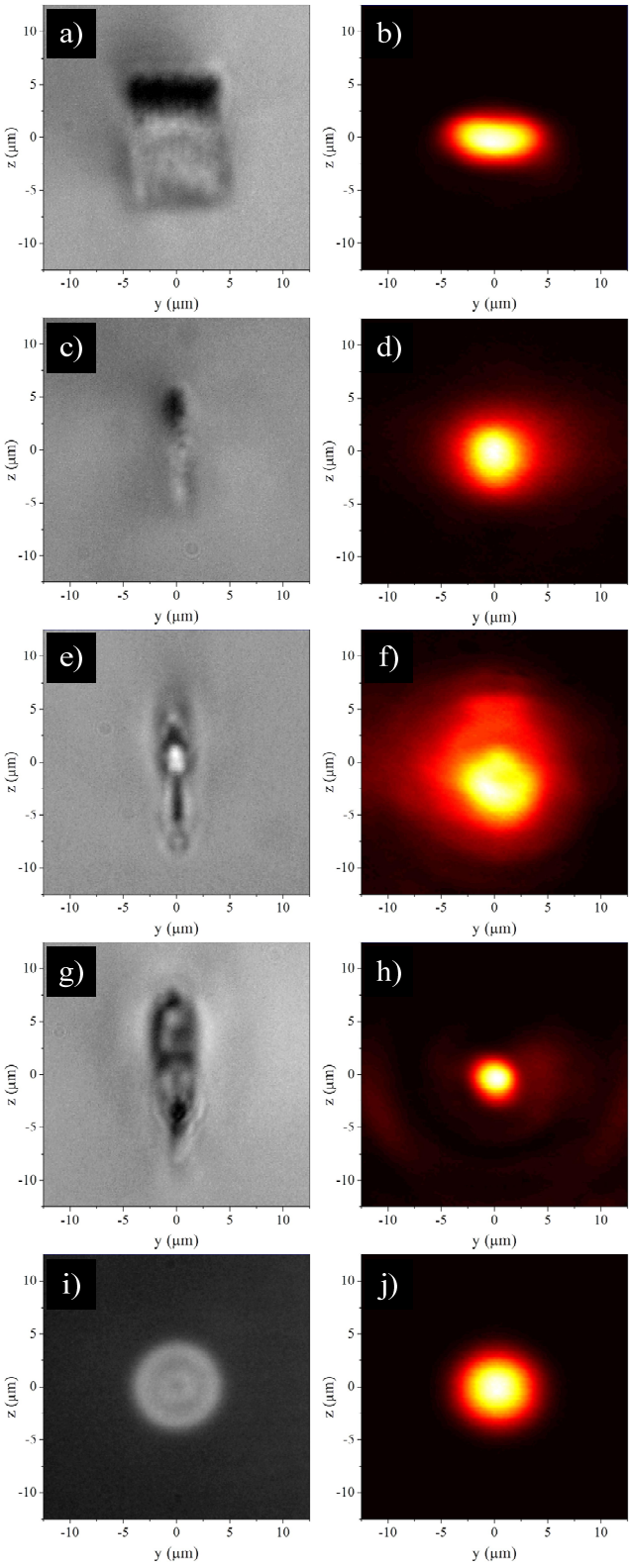

Figure 4-15. Microscope facet images and corresponding guided mode profiles of various waveguides. SMF-28 fibre is included for comparison in i) and j).

The single-scan structure shown in c) and d) is able to guide, however the mode is not well confined, with considerable amounts of the mode present outside the modified region. As the pulse energy is increased to 500 nJ as shown in e) and f), the larger structure induced is able to guide over a larger area and indeed is slightly multimode in the vertical axis, however it also not well confined in the horizontal axis with a significant amount of light outside the modified structure. As the pulse energy is increased to 681 nJ as shown in g) and h), considerable amounts of damage prohibits strong guiding over much of the structure, however a region of very high refractive index change is observed, indicated by the presence of a very small single-mode which is considerably smaller than the 9.2 μm guided mode of SMF-28 at 1320 nm, shown in j). The pulse energy of 851 nJ did not show any guiding due to the extreme level of damage present.

4.4.7 Gain measurements

In order to ascertain whether the waveguides were able to provide gain, the waveguides were pumped with up to 190 mW at 810 nm and up to 600 mW at 980 nm. Both insertion loss and gain were measured simultaneously using the same experimental arrangement as described previously. Figure 4-16 shows the experimental setup used to measure the gain and insertion loss. As carried out earlier, a reference measurement for the insertion loss was carried out by using a piece of SMF-28 fibre spliced to the WDMs. This fibre was then broken, cleaved and butt-coupled to the waveguide under test. 810/1300 and 980/1300 nm custom WDMs, provided by SIFAM fibre optics, enabled the pump wavelength to be multiplexed/de-multiplexed with the signal wavelength.

A minimum insertion loss of 4 dB was measured for a single scan waveguide fabricated using 300 nJ pulses and a 1 mm/s translation speed. This is particularly high considering the 5 mm waveguide length, and is likely to be due to scattering losses from the damage present in the fabricated structure. No gain was measured from this waveguide, indeed out of all the structures capable of guiding at 1320 nm, only two waveguides provided gain.

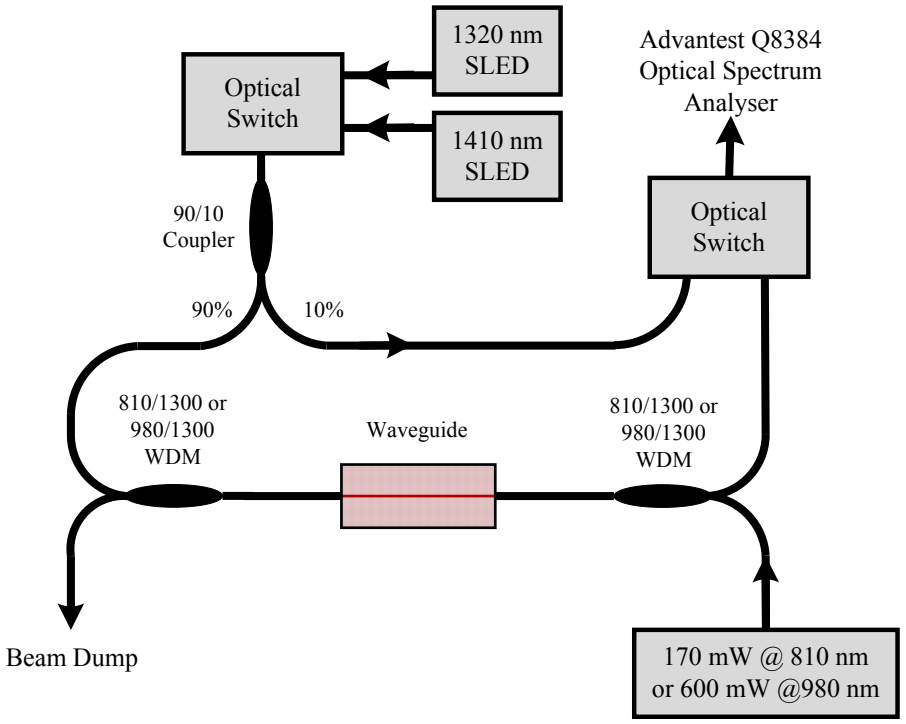

Figure 4-16. Experimental setup for insertion loss and gain measurements.

The first waveguide capable of providing gain was the weakly guiding slow translation speed multi-scan fabricated with 180 nJ pulses as detailed earlier, which is now denoted G1. This waveguide exhibited an insertion loss of 22 dB at 1320 nm due to the poor confinement and high coupling losses. The guided mode was barely visible on the vidicon camera, and no modification was visible under the microscope due to the small refractive index change, and large amount of visible absorption in the substrate glass due to the Bi-doping. Figure 4-17 shows the relative gain spectrum for waveguide G1 under 810 and 980 nm pumping.

When the waveguide was pumped with 190 mW at 810 nm, a peak relative gain of 3 dB was observed. As mentioned earlier, in Bi-doped glass, no absorption bands lie within the signal region, therefore all relative gain observed is in fact *internal* gain. Due to the weak mode confinement, the waveguide did not guide at longer wavelengths provided by the 1410 nm SLED.

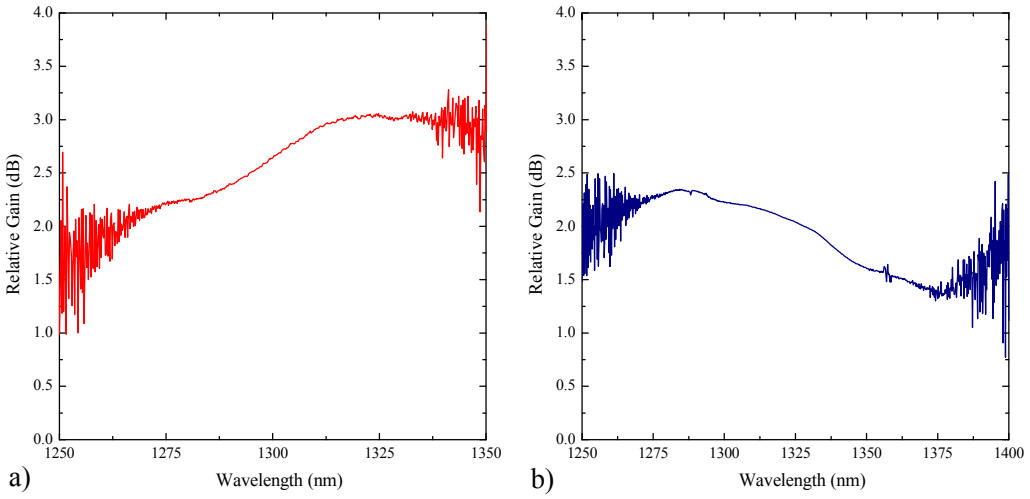

Figure 4-17. Relative gain spectra for waveguide G1. a) 810 nm pumping, b) 980 nm pumping.

The 3 dB gain measured under 810 nm pumping yields an internal gain per unit length of 6 dB/cm, which is particularly high compared to the values typically obtained in commercial EDWAs of around 2 dB/cm. Under 980 nm pumping, a smaller amount of gain is observed, with the gain spectrum appearing to tend towards a peak at shorter wavelengths. This is in accordance with the bulk fluorescence line-shape as measured earlier and shown in Figure 4-13. It is possible more gain may be measured at considerably shorter wavelengths given a suitable source and WDMs in this region.

The second waveguide to demonstrate gain was a single-scan waveguide fabricated with 300 nJ pulses and a 3 mm/s translation speed, which is now denoted G2. This waveguide exhibited an insertion loss of 9 dB at 1320 nm. The waveguide facet image and guided mode profile are shown in Figure 4-15 c) and d). Under pumping, a large amount of scattering was observed from a CCD camera viewing the waveguide from above, indicating that the dark damage structures observed in the facet images are indeed scattering centres at least partially due to micro-voids. Figure 4-18 shows the relative gain spectra for G2 when pumped at 810 nm and 980 nm. The 810/1300 nm WDMs were not particularly broad-band, which prohibited gain measurements at longer wavelengths for 810 nm pumping. The peak relative gain observed at 810 nm

pumping was approximately 1 dB, which is considerably lower than the 3 dB observed from waveguide G1, however the large amount of scattering present may considerably reduce the amount of pump absorption.

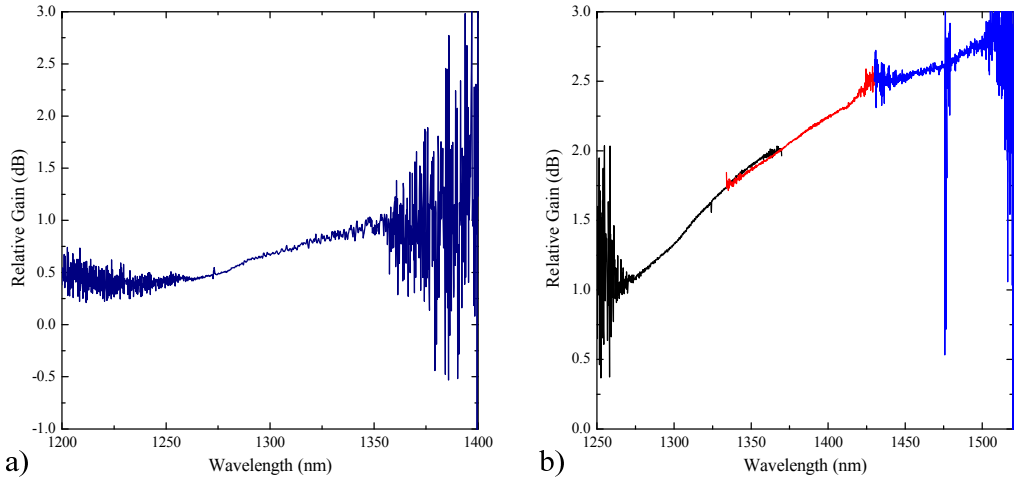

Figure 4-18. Relative gain spectra for waveguide G2. a) 810 nm pumping, b) 980 nm pumping.

Under 980 nm pumping, an extremely broad gain bandwidth of greater than 200 nm was observed. Indeed the gain bandwidth appears considerably larger than measureable using the experimental setup. As the gain bandwidth was clearly larger than the signal coverage provided by the two SLEDs, a longer wavelength broadband source was obtained by utilising a 1480 nm pump laser, operated below threshold. The sharp noise peaks observed at around 1480 nm are due to the presence of the external FBG used to stabilise the wavelength of the pump laser. Beyond 1500 nm, very little signal was present through the system, preventing the observation of gain beyond this wavelength. The spectral position of the gain bandwidth observed here is particularly interesting considering the bulk fluorescence spectrum under 980 nm excitation peaks around 1150 nm. This change in the spectral position may be due to considerable modification to the form of the active bismuth centres in the substrate glass due to fs-irradiation.

Indeed, the lack of gain provided by all but two of the waveguides indicates that the inscription process itself has detrimentally modified the gain capabilities of the substrate material. Possible mechanisms for this could be photo-induced

changes in the valence state of Bi-ions, or changes in the local structure around the Bi-centres. The formation of low order Si-O ring structures in silica glass under fs-irradiation has been well documented [34]. These low order structures could disrupt the Al-Si rings suggested to be essential in the formation of active negatively charged bismuth dimer molecules [116].

Recently, the modification of the luminescence properties of Bi-doped glasses using fs-irradiation has been reported by Zhou *et al.* [140]. The authors report the observation of dramatic changes in the visible and infrared absorption bands for irradiated regions compared to the bulk glass. This confirms that the lack of gain observed in all but two waveguides is due to modification of the active bismuth centres. The two waveguides that provide gain both have considerable mode-overlap with unmodified material, and therefore may be achieving gain from these regions.

The lack of achievable gain in most waveguides, combined with the high insertion losses measured indicates that an alternative approach is required in order to achieve a bismuth-doped waveguide amplifier using ULI. As the waveguides that supplied gain may have provided this from the mode overlapping with unmodified material, the flexibility of ULI could allow a waveguiding structure to be fabricated that allows the combination of low-losses and gain. Alternatively the material could be engineered such that the bulk material produces the correct form of bismuth centres upon fs-irradiation. Such an approach could also have benefits in high-power laser applications, where cladding pumping could be employed with an effectively un-doped cladding inscribed using different fabrication parameters. Preliminary work on fabricated such materials has recently been reported [141]. The authors have reported the fabrication of a Bi-doped mesoporous glass, whereby the space-selective fabrication of luminescence centres can be created by fs-irradiation. Waveguide fabrication in such materials has not yet been investigated.

The large red-shifting of the gain band observed in waveguide G2 under 980 nm excitation is particularly promising for the fabrication of extremely broad amplifiers if net gain can be achieved. The ability to tune the position of the gain

bandwidth by altering the ULI fabrication parameters could be extremely useful and would allow Bi-doped glasses to become highly flexible gain media. The amount of gain demonstrated is also particularly high, with an internal gain per unit length of 6 dB/cm. This could potentially allow very compact high-gain devices to be fabricated.

4.5 CONCLUSIONS AND FURTHER WORK

From the work presented in this chapter, several important contributions to the field have been made. The initial work carried out in LAZS glass was the first demonstration of a waveguide fabricated in Bi-doped glass. The ultra-broad fluorescence emission provided the largest fluorescence bandwidth emission ever obtained from a waveguide fabricated using ULI. Despite the lack of gain, such fluorescence could be used as a source for optical coherence tomography whereby larger bandwidths allow higher resolution images to be obtained. The gain results provided by the waveguide fabrication in Bi-doped alumino-silica glass provide interesting insight into the mechanism of emission from bismuth centres which is poorly understood within the academic community.

The achievement of large amounts of internal gain from the Bi-doped alumino-silica glass is a testament to the potential for compact high-gain Bismuth doped waveguide amplifiers. The ability to tune the spectral position of the emission may allow Bi-doped amplifiers to cover all telecommunications bands simultaneously.

The work presented in this chapter could be progressed in several ways. Firstly, due to the inherent flexibility of ULI, a waveguiding structure could be fabricated that allows significant mode-overlap with unmodified material. This could be achieved by fabricating two closely spaced regions of refractive index modification. Given the correct index contrast and spacing, a guided mode covering the entire two structures could be produced, with the peak intensity in the central region occupying unmodified material. Alternatively, a tapered

structure with varying waveguides cross section could be fabricated, providing good coupling to the fibres at either end of the structure, and gain in the centre.

An alternative approach could be to engineer the substrate material so that upon irradiation with femtosecond pulses, the correct luminescent form of Bismuth is produced. This could enable the activation of a gain capable substrate by ultrafast laser irradiation. This approach has begun to be investigated by Zhou *et al.*, with the fabrication of a Bi-doped mesoporous glass that does not contain luminescent Bi-centres, however upon irradiation exhibits luminescence in the irradiated regions [141].

Overall the work presented in this chapter has shown that Bi-doped substrates have considerably potential for fabricating Bismuth-doped waveguide amplifiers and waveguide lasers, however further work is required in order to exploit this potential.

CHAPTER 5 – WAVEGUIDE INSCRIPTION IN CHALCOGENIDE GLASS

5.1 INTRODUCTION

Chalcogenide glasses have been studied extensively over the past 50 years due to their well established infrared transmission [142]. More recently, their strong third-order optical nonlinearities have been exploited in a wide range of nonlinear optical applications such as optical switching or supercontinuum generation [143]. Guided-wave nonlinear optical devices enable the exploitation of nonlinear behaviour at relatively low optical powers due to the inherent high intensities achieved in optical fibres or waveguides.

Mid-infrared waveguide devices are of particular interest for sensing applications due to the presence of many fundamental absorption lines of a wide range of molecular species [144]. The broad transmission bandwidth of chalcogenide glasses in this spectral region could enable the fabrication of new forms of integrated optical sensor devices in a compact and low cost format.

The work described in this chapter covers the investigation of waveguide fabrication inside a germanium sulphide based chalcogenide glass. The substrate material provided for this investigation was designed and fabricated by Prof A. Jha and co-workers at the University of Leeds. The waveguide fabrication work was carried out during visits to the Politecnico di Milano under a collaborative research project funded by the European Union Centre for Ultrafast Science and Biomedical Optics (CUSBO).

Section 5.2.1 introduces chalcogenide glasses followed by a discussion of the applications in Section 5.2.2. Section 5.3 introduces the waveguide fabrication experiments carried out in the chalcogenide glass and morphological studies on the fabricated structures. Section 5.4 presents results of supercontinuum generation experiments on the fabricated waveguides.

5.2 CHALCOGENIDE GLASSES

5.2.1 Introduction to chalcogenides

Chalcogenide glasses are inorganic glassy solids comprised of one or more of the chalcogen elements S, Se or Te, excluding O. The chalcogen elements are then combined with some network forming element which is most commonly As or Ge [142]. Many other elements may also be used as network formers for example P, Sb, Bi, Si, Sn, Pb, and Lanthanides. Chalcogenides are bound by covalently bonded molecules, not ionic bonds as with most other glasses and are referred to as molecular solids [145]. Both hetero-polar (eg Ge-S) and homo-polar (eg Ge-Ge) bonds can form allowing a very flexible local electronic configuration to form within complex compositions [142]. The ratio of constituent elements can be varied dramatically whilst remaining a glassy solid, for example in the case of As-S systems, the atomic ratio of As to S can be varied from 1.5 to 9 [145].

This wide range of compositional components, ratios of those components, and bond configurations allow the properties of chalcogenide glasses to be broadly tuned. The linear refractive index of chalcogenide glasses is particularly high, ranging from 2 to over 3 [145]. Chalcogenide glasses possess high nonlinear refractive indices, with nonlinear refractive index values of several orders of magnitude greater than for fused silica. Values up to 1000× fused silica have been reported for Ge-As-Se based systems [146].

Chalcogenide glasses exhibit a plethora of photo-induced phenomena such as photo-crystallisation (or amorphisation), photo-polymerisation, photo-decomposition, photo-contraction (or expansion), photo-vaporisation, photo-darkening, photo-bleaching, photo-dissolution of metals, and photo-induced changes in the local atomic configuration [147]. Such changes also affect the optical properties of the material such as the size of the bandgap, the refractive index and the absorption coefficient [147].

Chalcogenide glasses have low maximum phonon energies, which makes them particularly useful for doping with rare-earth ions. The low phonon energy effectively activates many IR transitions in rare-earth ions which would be

phonon quenched in other hosts [148]. The low phonon energies also contribute to the wide infrared transmission of chalcogenide glasses, with sulphide glasses typically transmitting up to 12 μm, selenide glasses up to 15 μm and tellurides up to 20 μm [142]. Impurities significantly affect the IR transmission, in particular hydroxide contamination creates absorption bands in the 2-5 μm region, and oxide contamination in the 6-15 μm region [142].

5.2.2 Applications of chalcogenides

Chalcogenide glasses were first explored for mid-IR transmission in the 1950's [142], however more recently the nonlinear behaviour of chalcogenide glasses has been widely exploited. Fabricating guided-wave devices significantly enhances the nonlinear behaviour due to the high intensities achieved during confinement. A measure of the effective nonlinearity of a guided wave nonlinear medium is the effective nonlinear parameter γ, which is defined as [149]:

$$\gamma = \frac{2\pi n_2}{\lambda A_{eff}} \qquad 5\text{-}1$$

where n_2 is the nonlinear refractive index, λ is the wavelength, and A_{eff} is the effective mode area of the guided mode. Clearly the effective nonlinearity can be increased by reducing the size of the mode or increasing the nonlinear refractive index of the material. Typical values of γ for standard telecommunications fibres are approximately 3 $W^{-1}km^{-1}$, however highly nonlinear chalcogenide fibres have been produced with γ values of approximately 1300 $W^{-1}km^{-1}$ [150].

Fabricating optical fibres using chalcogenide glass has led to the demonstration of optical switching using the nonlinear optical loop mirror technique (NOLM). This was demonstrated by Asobe *et al.* in 1996, with all-optical switching with gate peak powers as low as 0.4 W, enabling the de-multiplexing of a 40 GHz pulse train to 4 GHz [143]. Other all-optical signal processing demonstrations such as frequency conversion using cross-phase modulation have been demonstrated in chalcogenide fibres [151], as well as 2R optical regeneration [152]. Raman

amplification has also been demonstrated in chalcogenide fibres with Thielen demonstrating more than 20 dB of gain in an As-Se fibre [153].

Significant interest exists in the fabrication of compact nonlinear optical devices. In particular photonic chip-scale devices for all-optical signal processing. Conventional waveguide devices using thin-film deposition followed by lithography and etching have been produced by Viens *et al.* in 1999 [154]. More recently, Madden *et al.* fabricated a 22.5 cm long serpentine S-shaped chalcogenide waveguide demonstrating losses as low as 0.05 dB/cm [155], and an effective nonlinearity value γ of 2080 $W^{-1}km^{-1}$ [150]. The same group were able to demonstrate a whole host of all-optical signal processing techniques such as error free wavelength conversion using cross-phase modulation [156], all-optical time division de-multiplexing at 160 Gbits/s [157], supercontinuum generation in a tapered rib waveguide [158], net gain from an optical parametric amplifier [159], and most recently a breakthrough switching speed of 640 Gbits/s for optical time division de-multiplexing [160].

ULI has also been used for the fabrication of waveguides in chalcogenide glasses. The wide range of photo-sensitivities displayed by chalcogenide glasses make them ideal candidates for the inscription of waveguides using ultrafast lasers. The first demonstration of waveguide fabrication in chalcogenide glass was shown early on in 1997 by Miura *et al.* in the second paper to be published in the field of ULI [47]. Waveguides were fabricated using a Ti:sapphire laser with a repetition rate of 200 kHz, however no guiding was shown from chalcogenide glasses.

A subsequent paper by Efimov *et al.* in 2001 fabricated waveguides in As-S chalcogenide bulk glasses with a high repetition rate Ti:sapphire oscillator using a maximum pulse energy of 4 nJ [161]. A change in the bandgap was observed due to photo-darkening along with a corresponding refractive index change of approximately $\Delta n = 5\times10^{-4}$. Raman spectroscopy carried out on the modified regions revealed an increase in the formation of homopolar As-As and S-S bonds. The mechanism for modification was suggested to be either two-photon absorption or supercontinuum generation providing linear absorption at the short wavelength side of the broadened spectrum of the writing laser.

A more recent paper by Zoubir *et al.* in 2004 demonstrated large refractive index changes of up to $\Delta n = 8\times10^{-2}$ (~4%) in As_2S_3 thin films [89]. Waveguides were fabricated using an extended cavity Ti:sapphire laser with a repetition rate of 25 MHz, a pulse duration of 30 fs and a maximum pulse energy of 20 nJ. In contrast to the Raman spectroscopy results observed in the Efimov paper, a reduction in homopolar bonds was found. The refractive index change was found to be mainly due to photo-darkening as revealed by absorption measurements.

Waveguide fabrication in a Ga-La-S based system was demonstrated by Hughes *et al.* in 2007 [162]. GLS glass offers potential benefits as an optical switching medium due to its low multi-photon absorption co-efficient and relatively high nonlinearity. A relatively weak refractive index contrast was observed, along with small changes in the Raman spectrum, indicating that any structural modifications were small.

A paper discussing the mechanisms of photo-induced modifications from ultrafast laser irradiation of chalcogenide glasses was published by Petit *et al.* in 2008 [163]. In particular Ge-S based systems were fabricated, analysed and discussed. A negative refractive index change was observed in Ge-S based films, along with a corresponding large photo-expansion. Raman spectroscopy studies reveal that the types and amounts of new bond formation depends heavily on the ratio of compositional elements in the substrate. Interestingly, the inclusion of modifiers such as gallium to the chalcogenide glass were shown to increase the amount of photo-expansion, however less structural variation in the bonds was observed by Raman spectroscopy.

A subsequent paper by Anderson *et al.* in 2008 investigated ultrafast laser irradiation of Ge-S based thin films, using both a low repetition rate 1 kHz chirped-pulse-amplified Ti:sapphire laser and a high repetition rate 80 MHz Ti:sapphire oscillator [164]. A strong negative refractive index change was observed at high repetition rates, along with a strong corresponding photo-expansion. Interestingly, no refractive index modification was observed with the low repetition rate system.

These studies on ultrafast laser inscribed structures in chalcogenide glasses form an interesting foundation for work to be carried out. In particular the very high refractive index changes demonstrated of up to ~4% are considerably higher than the values typically achieved in silicate glasses of ~0.3%. This large Δn leading to a strong confinement, along with the high nonlinearities of chalcogenide glasses could enable a whole host of highly nonlinear integrated optical devices to be fabricated.

5.3 WAVEGUIDE FABRICATION IN CHALCOGENIDE GLASS

5.3.1 ONL2 glass

The substrate material used for waveguide fabrication work was a Ge-S based glass fabricated by the University of Leeds. The precursor composition of the substrate glass was $79GeS_2$ - $15Ga_2S_3$ - 6CsI. The inclusion of the network modifiers Ga_2S_3 and CsI serve to increase the bandgap, reducing the multi-photon absorption (MPA) coefficient whilst maintaining the nonlinear refractive index n_2. The fabrication and nonlinear characterisation of this substrate material, known as ONL2, is described extensively in reference [165]. The nonlinear refractive index n_2 for this material was measured using the z-scan technique by Bookey [166], and was found to be 6×10^{-19} m^2W^{-1} at 1550 nm. This value is approximately 22× the n_2 value of fused silica. The bandgap of the substrate was 2.69 eV, which corresponds to a band-edge wavelength of 459 nm. The linear refractive index n_0 was 2.2.

The absorption spectrum of the glass was measured using a Bruker IFS 66V/S FT-IR spectrometer, which operates between 700 and 5000 μm. A background scan with no sample was taken, and then the absorption spectrum of the sample was measured. The spectrum was then normalised to the signal value at 2.5 μm in order to discard any alignment affects of the sample mounting in the spectrometer. Figure 5-1 shows the obtained absorption spectrum.

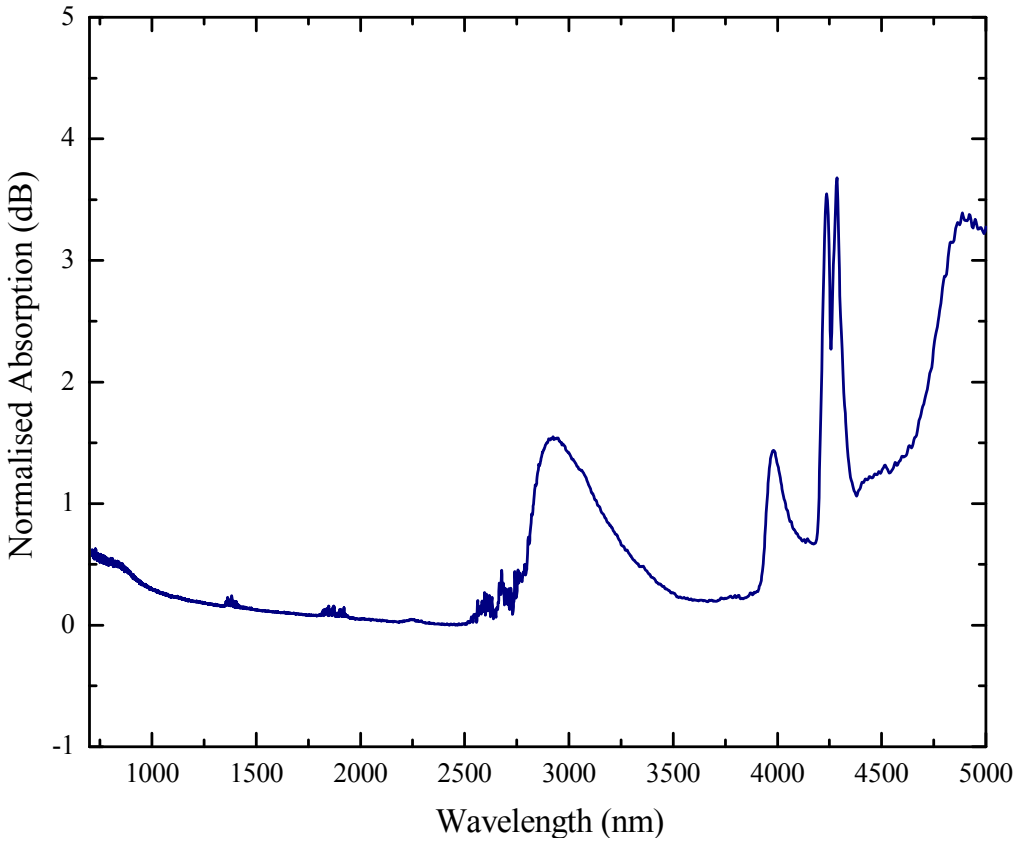

Figure 5-1. Absorption spectrum of ONL2 chalcogenide glass.

The obtained spectrum shows clear absorption bands in the mid infrared region. These bands are almost certainly due to impurities in the substrate material. According to Seddon, the absorption bands in the 2.5 to 3.5 μm region is due to H_2O impurities and the corresponding O-H bond, and the bands occurring in the 4 to 5 μm region are due to the S-H bond [142]. Both of these are a direct result of water contamination in the fabrication of the material. In the absence of impurities, sulphide glasses transmit well up to 12 μm, and so the presence of these absorption bands in ONL2 glass may well limit its uses for long wavelength applications.

5.3.2 Waveguide fabrication

The laser used to inscribed the waveguides was the same cavity dumped Yb:glass oscillator described in Section 3.2.5. The laser outputs 350 fs pulses with a

maximum pulse energy of 500 nJ at repetition rates up to 1.5 MHz. The central wavelength of the laser was 1040 nm. The sample was mounted on a set of computer controlled Physik Instrumente M-511.DD XY motorised translation stages. The pulse train was focused to a depth of approximately 200 μm below the sample surface using a ×50, 0.6 NA microscope objective, however the beam did not fill the full aperture of the lens, resulting in an effective $NA_{eff} \approx 0.3$. The repetition rate of the laser was set to 600 kHz and the polarisation set to perpendicular to the laser beam and writing direction. A wide range of fabrication parameters were investigated with pulse energies from 83 to 492 nJ and translation speeds from 250 to 4000 μm/s. As previous work has shown particularly strong material modification, only single-scan fabrication was investigated. After fabrication the waveguide facets were cut and polished to give a final sample length of 8.4 mm.

5.3.3 Waveguide morphology

After fabrication, the waveguide facets were observed on a microscope operating in transmission mode. Figure 5-2 shows cross-section microscope images of the fabricated structures for varying pulse energies and translation speeds. The fabricated structures exhibit a characteristic tear-drop shape, with a strongly modified elongated central region, accompanied by an outer ring. The shape of the structure is dominated by thermal accumulation effects, and is similar to that observed by Eaton *et al.* in Eagle 2000 borosilicate glass [54]. The low phonon energies of chalcogenide glasses combined with the relatively low glass transition temperature T_g of approximately 400 °C [142] may explain the dominance of thermal accumulation effects. The central elongated modified region was suggested by Eaton *et al.* to be due to high temperature impacts from the pulse absorption in the focal region, and the surrounding ring due to slow thermal diffusion, with highly non-uniformal cooling rates providing a non-uniform structure [54]. This suggestion does not account for the long elongation of the central region, which in the case of the waveguides shown here may contain a significant contribution from the formation of a plasma filament.

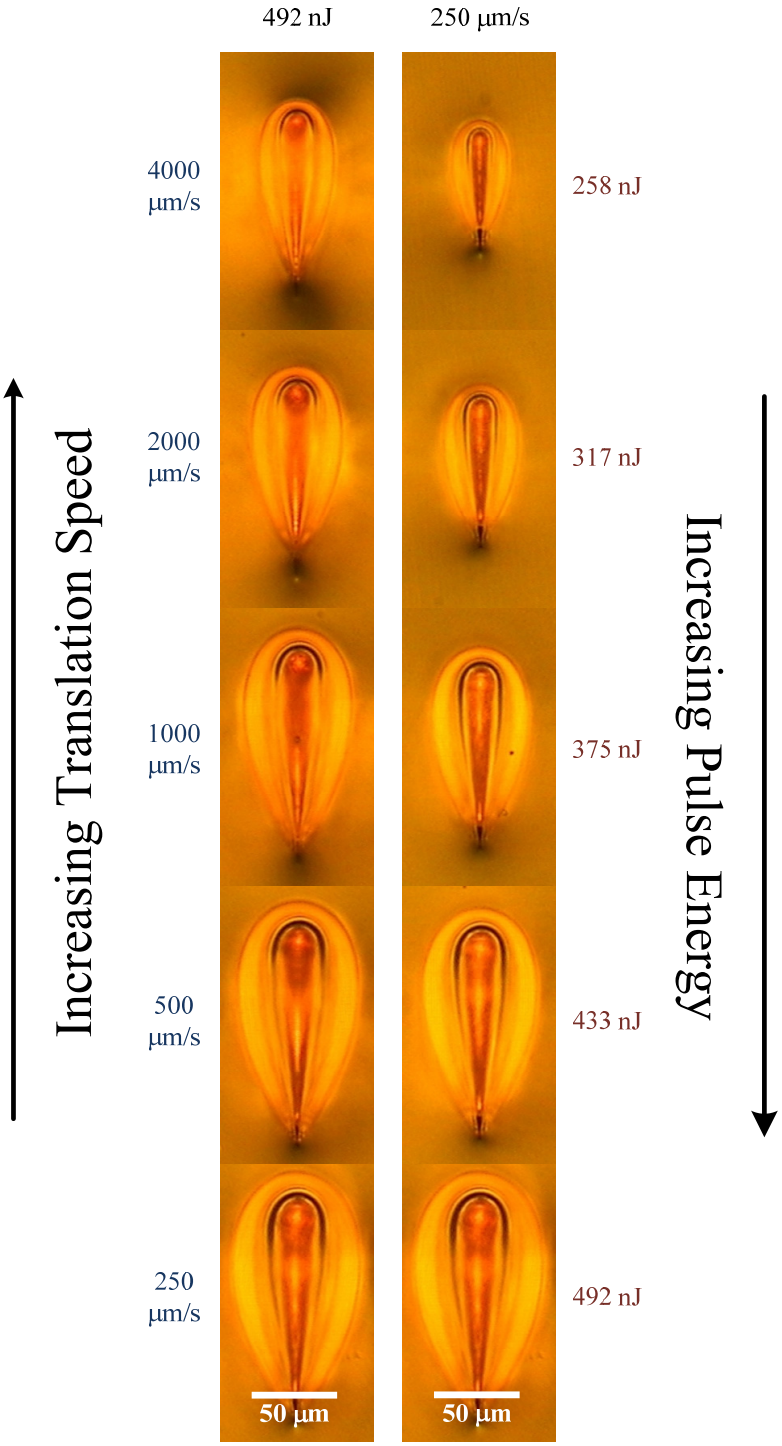

Figure 5-2. Microscope cross-sectional facet images of waveguides, showing scaling with both translation speed and pulse energy. The left column shows waveguides with a pulse energy of 492 nJ and varying translation speed, and the right column shows waveguides written with a 250 µm/s translation speed and varying pulse energy. The bottom two images show the same waveguide.

The general form of the modification remains largely unchanged with variations in fabrication parameters, however the size of the structure scales strongly with both translation speed and pulse energy. According to Eaton *et al.*, the scaling of the waveguide diameter with varying translation speed is an immediate indication of the presence of thermal accumulation and not simply thermal diffusion [54]. Figure 5-3 plots the variation in both vertical and horizontal sizes of the entire structure as a function of pulse energy for different translation speeds.

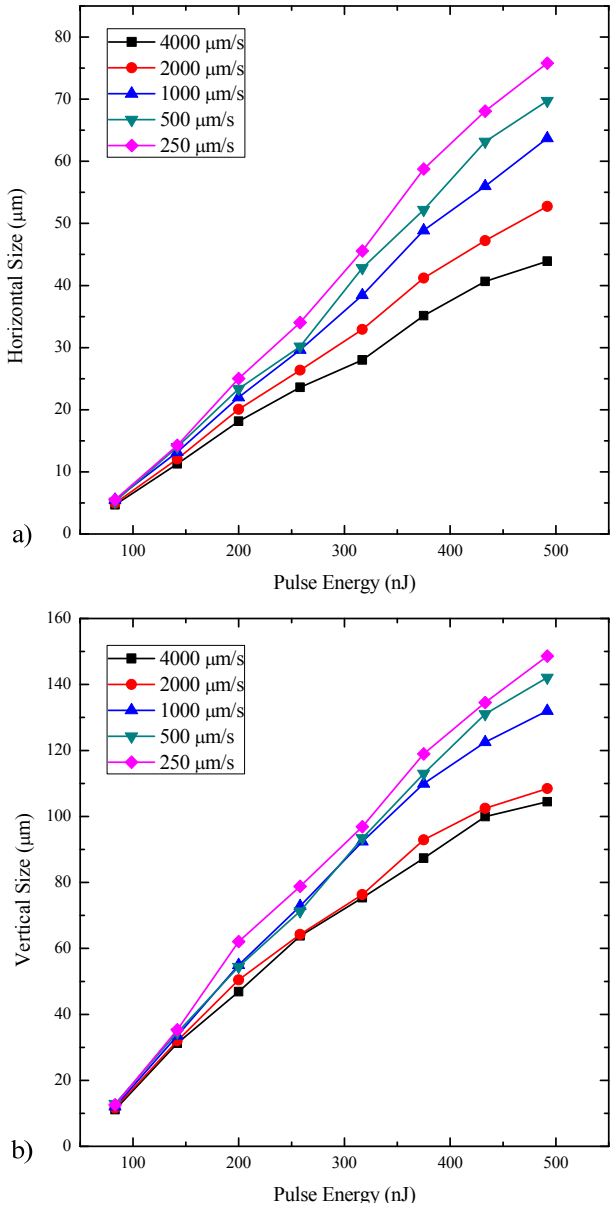

Figure 5-3. Graphs showing size variations of the fabricated structures. a) Horizontal size, b) Vertical size. The lines are included as a guide for the eye.

From Figure 5-3 it is clear that higher pulse energies lead to larger structures with an almost linear dependence. The effect of slower translation speeds on the size of the structure is much more pronounced for higher pulse energies, particularly in the horizontal direction. A variation of almost a factor of approximately 1.7 is present in the horizontal size for the highest pulse energy of 492 nJ, compared to approximately 1.2 at the lowest pulse energy of 83 nJ. This may indicate that thermal accumulation has a more dominant effect over the width of the structure at higher pulse energies.

The vertical size of the structures is more strongly dependent upon pulse energy than the horizontal size. The vertical size also scales with a variation in translation speed, however the dependence is weaker than for the horizontal size. This may be evidence that filamentation is playing a significant role in the formation of the central elongated region, the intensity and length of which is highly dependent on the pulse energy. Interestingly, for pulse energies above 200 nJ the vertical size of the two fastest translation speeds of 4000 μm/s and 2000 μm/s are relatively close and diverge away from the slower translation speeds. The gradient of the pulse energy dependence as a function of pulse energy also appears to reduce for higher pulse energies and is stronger for faster translation speeds. This may indicate a reduction in the dominance of thermal accumulation in the high pulse energy high translation speed regime.

Figure 5-4 shows the aspect ratio of the fabricated structures as a function of the fabrication parameters. The inset image shows how the measurements were taken. It is clear that the slowest translation speed of 4000 μm/s has the largest aspect ratio, and slower translation speeds yield a more symmetrical structure due to the slower speed driving an increased contribution from thermal accumulation. Higher pulse energies also allow more symmetrical structures, however the dependence is not as strongly defined as for translation speed. The pulse energy dependence is more pronounced for slow translation speeds, which is further evidence for increased thermal accumulation present.

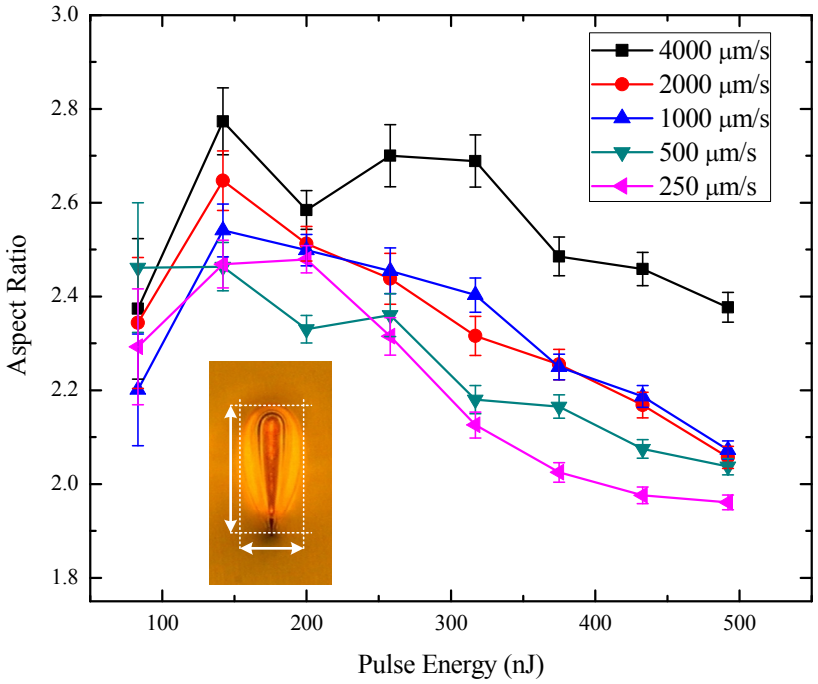

Figure 5-4. Graph showing variation in aspect ratio as a function of fabrication parameters. The inset image shows the measurements used for obtaining the data. The errors were calculated from the relative contributions from the uncertainties in the edges of the structures. The lines are included as a guide to the eye.

The depth of the waveguide structures from the surface of the sample was shown to have a strong dependence on the pulse energy, due to self-focussing

The critical power for self-focussing induced filamentation can be calculated from equation 5-2 [13]:

$$P_{cr} = \frac{3.77\lambda^2}{8\pi n_0 n_2} \qquad 5\text{-}2$$

where λ is the wavelength of the laser, n_0 is the linear refractive index and n_2 is the nonlinear refractive index. For the ONL2 substrate material, $n_0 = 2.2$, $n_2 = 6\times10^{-19}$ cm^2W^{-1}, and a laser wavelength of 1040 nm, the critical power for self-focussing is approximately 123 kW. Assuming a $sech^2$ pulse shape, the peak power of a laser pulse can be calculated from equation 5-3:

$$P_p = 0.88\frac{E_p}{\Delta\tau} \qquad 5\text{-}3$$

where P_p is the peak power of the pulse, E_p is the pulse energy, and $\Delta\tau$ is the pulse width. Re-arranging and substituting the critical power of 123 kW, and our pulse duration of 350 fs, we obtain a critical pulse energy for the onset of filamentation of approximately 49 nJ. This value is well below the minimum fabrication pulse energy of 83 nJ, indicating that catastrophic collapse due to self-focusing is present throughout. Figure 5-5 plots the depth of the waveguide position from the surface as a function of pulse energy. The translation speed did not affect the depth of the fabricated structures. This would be expected for nonlinear self-focussing which depends upon the peak power and not the translation speed.

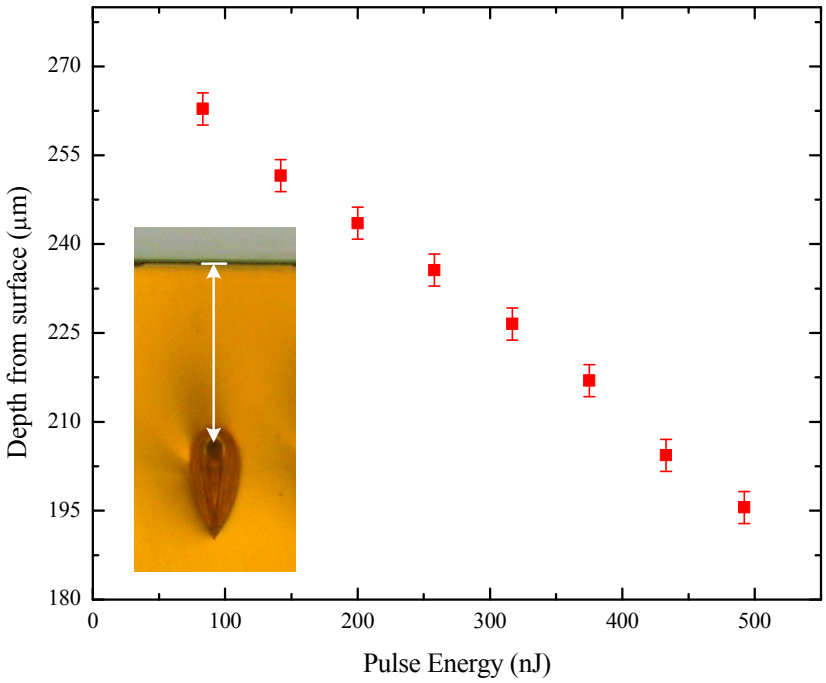

Figure 5-5. Graph showing depth dependence of the waveguide from the sample surface.

The depth of the waveguide from the sample surface reduces for higher pulse energies due to the stronger induced refractive index change from the pulse causing the beam to collapse at a shallower depth. This strong dependence of the waveguide depth on the pulse energy adds further weight to the cause of the central elongated region being primarily due to filamentation.

5.3.4 Guiding properties

In order to assess how light is guided in the fabricated structures, 1480 nm light was coupled into one side of the waveguide using direct fibre butt-coupling. Figure 5-6 shows a schematic diagram of the setup used to obtain near-field guided mode images. The opposite facet was imaged onto an Electrophysics 7920A Vidicon camera which was connected to a computer with a frame grabber card.

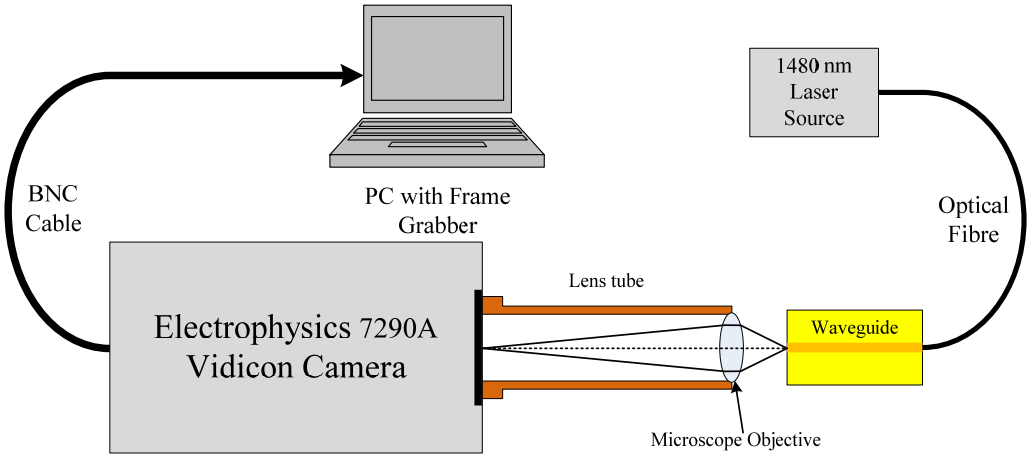

Figure 5-6. Schematic diagram of experimental setup for capturing near-field guided mode images.

The fabricated structures all showed strong guiding at the signal wavelength of 1480 nm. Figure 5-7 shows the typical guiding behaviour for waveguides fabricated with high pulse energies. Several distinct guiding regions were observed, with highly multimode guiding present for waveguides fabricated with high pulse energies. It is possible to couple into the elongated central region, which evidently has a strong positive refractive index change. There is a region at the top of the central structure that contains an even larger refractive index change, capable of guiding a single mode by itself, as shown in Figure 5-7 b). The elongated central 'core' region is surrounded by a region of a zero or negative index change, visible as a dark boundary layer in Figure 5-7 a). Outside of this boundary layer, a ring of positive refractive index change is present which can be coupled into as shown in Figure 5-7 e).

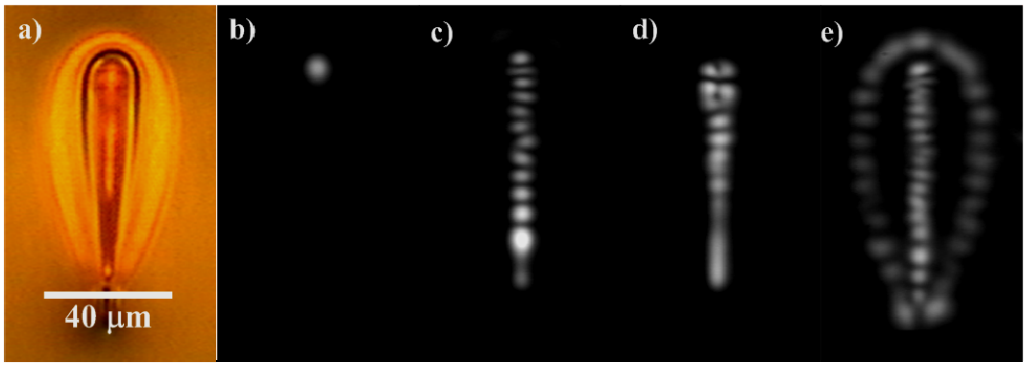

Figure 5-7. A) microscope image, b) – e) various guiding modal configurations obtainable by translating the input fibre. The waveguide was fabricated with 317 nJ pulses and a translation speed of 500 µm/s.

Clear, strong positive refractive index changes are present in these structures allowing the multimode guiding observed in Figure 5-7. This is in stark contrast to the strong negative refractive index changes observed in germanium sulphide based glasses by Petit *et al.* [163] and Anderson *et al.* [164]. It is possible that the the relatively high pulse energies used in the fabrication of these structures may enable the creation of the strong positive index changes observed here.

For waveguides fabricated with lower pulse energies, the smaller size of the structures reduces the number of guided modes as would be expected. Figure 5-8 shows microscope facet images and corresponding near-field guided modes for three waveguides fabricated with lower pulse energies. Clearly as the size of the structures is reduced, the outer ring becomes very weakly guiding, indicating that this ring has a significantly lower index contrast than the central core region. This is clearly observable comparing Figure 5-8 b) and d), where the central core region is still able to support several guided modes but the outer ring cannot. For the lowest pulse energy of 83 nJ as shown in Figure 5-8 f), structure is no longer observable on in the guided mode profile and only low order modes are supported vertically, with single-mode guiding occurring horizontally.

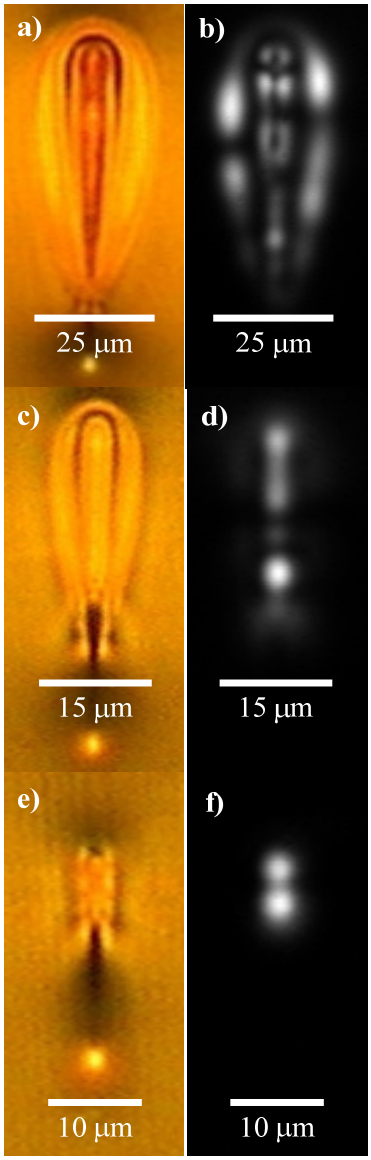

Figure 5-8. Microscope facet images and corresponding near-field guided mode images at 1480 nm for low pulse-energy waveguides.

Interestingly, the appearance of a small bright circular region below the main structure, visible on the microscope facet images, does not guide at 1480 nm for any waveguide. It is possible that this region does contain a positive refractive index change, but may be too small or too low an index contrast to support a guided mode at 1480 nm.

For the lowest pulse energy of 83 nJ, the fastest translation speed of 4000 µm/s yields a structure that is single-mode in both the horizontal and vertical axes.

Figure 5-9 shows the microscope image of the waveguide facet, guided mode image and plots of the intensity of the mode in the horizontal and vertical axes.

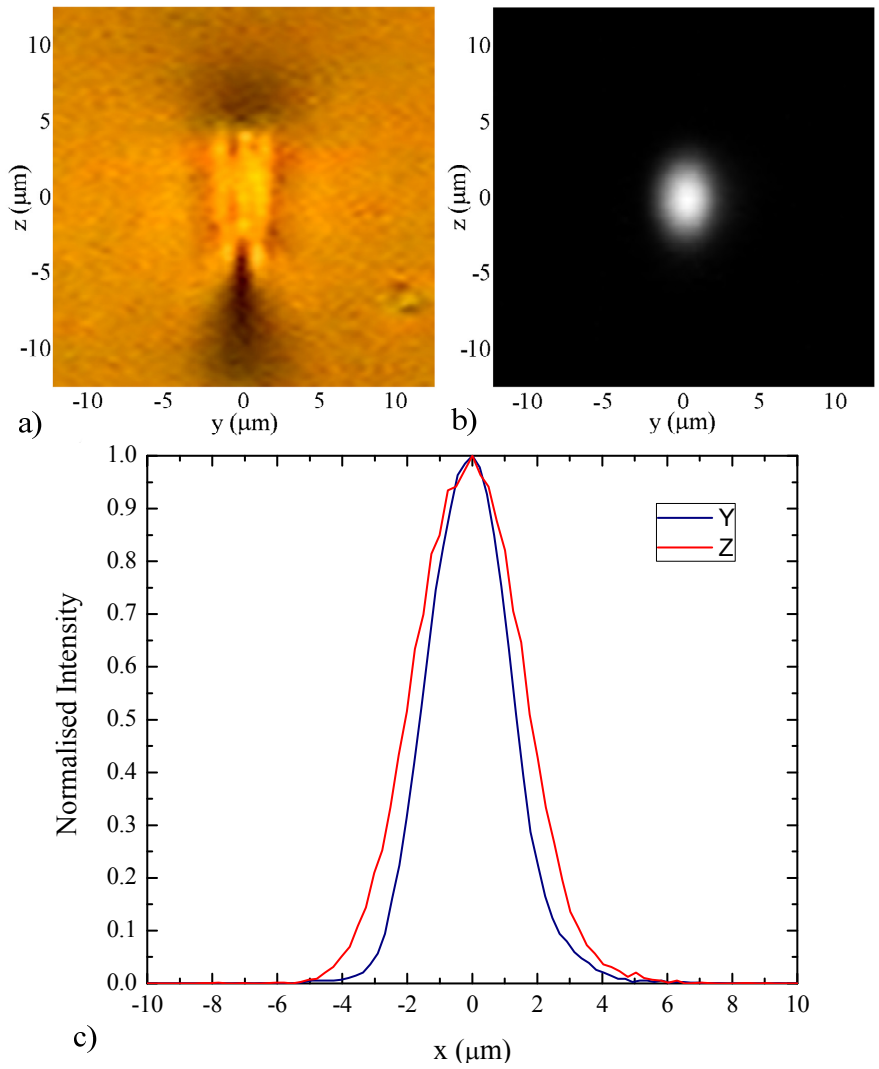

Figure 5-9. Single-mode guiding. a) microscope facet image, b) corresponding single guided-mode at 1480 nm. c) intensity line plots through the guided mode. The mode image captured from the camera was gamma corrected and normalised to obtain b) and c).

The single-mode guiding shown in Figure 5-9 indicates that the average refractive index change is considerably higher than that observed in other materials such as the glasses explored in Chapters 3 and 4. The $\frac{1}{e^2}$ mode field diameter is approximately 5 µm horizontally and 6 µm vertically. The amount of refractive

index contrast is difficult to estimate, and conventional techniques such as the RNF technique employed in Chapter 4 is not directly applicable to a substrate with such a high linear refractive index. Other techniques such as the micro-reflectivity technique would be capable of providing a refractive index profile, however no such facilities were available.

In order to compare the nonlinearity of this waveguide, we can calculate the value of γ, the effective nonlinearity. As shown earlier the value can be calculated from equation 5-4:

$$\gamma = \frac{2\pi n_2}{\lambda A_{eff}} \qquad 5\text{-}4$$

Calculating γ therefore requires the effective mode area A_{eff} to be calculated, which can be obtained from equation 5-5 [167]:

$$A_{eff} = \frac{\left(\iint_{-\infty}^{\infty} |F(x,y)|^2 dxdy\right)^2}{\iint_{-\infty}^{\infty} |F(x,y)|^4 \, dxdy} \qquad 5\text{-}5$$

Using the near field mode data shown in Figure 5-9, the value of γ was calculated using MATLAB. The program used for the evaluation of A_{eff} and subsequent calculation of γ is shown in the Appendix. Using the program, an effective mode area A_{eff} of 13.0 μm^2 was calculated, and with the n_2 value of 6×10^{-19} m^2W^{-1} the program yields a γ value of 196 $W^{-1}km^{-1}$.

This value of γ is considerably higher than many nonlinear fibres [167], however is lower than the 1000+ values obtained for As-S based small mode chalcogenide fibres and waveguides [150]. This is primarily due to As-S based substrate having a considerably higher value of n_2 than the ONL2 glass used for these experiments. Despite this, the waveguide shown here could still be used for integrated nonlinear optical applications, but would require more power to observe the same nonlinear behaviour. As-S based systems are notorious for strong photodarkening effects and large multi-photon absorption rates, which may limit their usability for a wide range of integrated nonlinear optics, particularly at high average powers [165]. The reduced toxicity of germanium based glasses

compared to arsenic is a practical benefit, which may allow use in situations requiring low toxicity.

5.4 SUPERCONTINUUM GENERATION EXPERIMENTS

5.4.1 Supercontinua

As a verification of the presence of nonlinear behaviour in the fabricated waveguides, supercontinuum generation experiments were carried out. Supercontinuum generation involves the generation of broadband light from a narrowband pump source using a range of nonlinear processes. Due to the high brightness broadband nature of the generated light, supercontinuum sources find applications in fields such as Optical Coherence Tomography (OCT) [168] or bandwidth expansion for few-optical-cycle pulse production [169]. For such applications, the generated radiation has to be temporally stable and spectrally smooth. For OCT, the attainable imaging resolution is inversely proportional to the bandwidth of the source, favouring broadband low-coherence radiation [168]. Near-infrared wavelengths are preferred for OCT because of their increased penetration depth in biological samples. The fabrication of broadband integrated supercontinuum sources is highly desirable in order to create compact cost effective sources for a wide range of applications.

The processes involved in supercontinuum generation depend on the sign of the group velocity dispersion (GVD) of the waveguide. If the net dispersion is positive, the regime is known as the ‘normal regime’, and if the net dispersion is negative, the regime is known as the ‘anomalous regime’. In the normal regime, the mechanisms for spectral broadening are primarily due to self phase modulation (SPM), cross-phase modulation (XPM) and Stimulated Raman Scattering (SRS). In the anomalous regime, these effects are augmented by a whole host of processes such as modulation instability, self-steepening and soliton fission. Strong dispersion causes the peak power of the pulse to be rapidly reduced due to temporal broadening of the incident pulse. Operating close to the zero dispersion point enables efficient supercontinuum generation. Chalcogenide glasses typically have zero dispersion wavelengths well into the mid-infrared (3-5

μm) [145], so efficient supercontinuum generation would require some form of dispersion management, such as compensating with dispersion shifted guiding structures such as micro-structured fibre, or by using a taper.

5.4.2 Experimental setup

In order to generate supercontinua, femtosecond pulses from an optical parametric amplifier were coupled into the waveguides. Figure 5-10 shows a schematic diagram of the experimental setup for generating supercontinua.

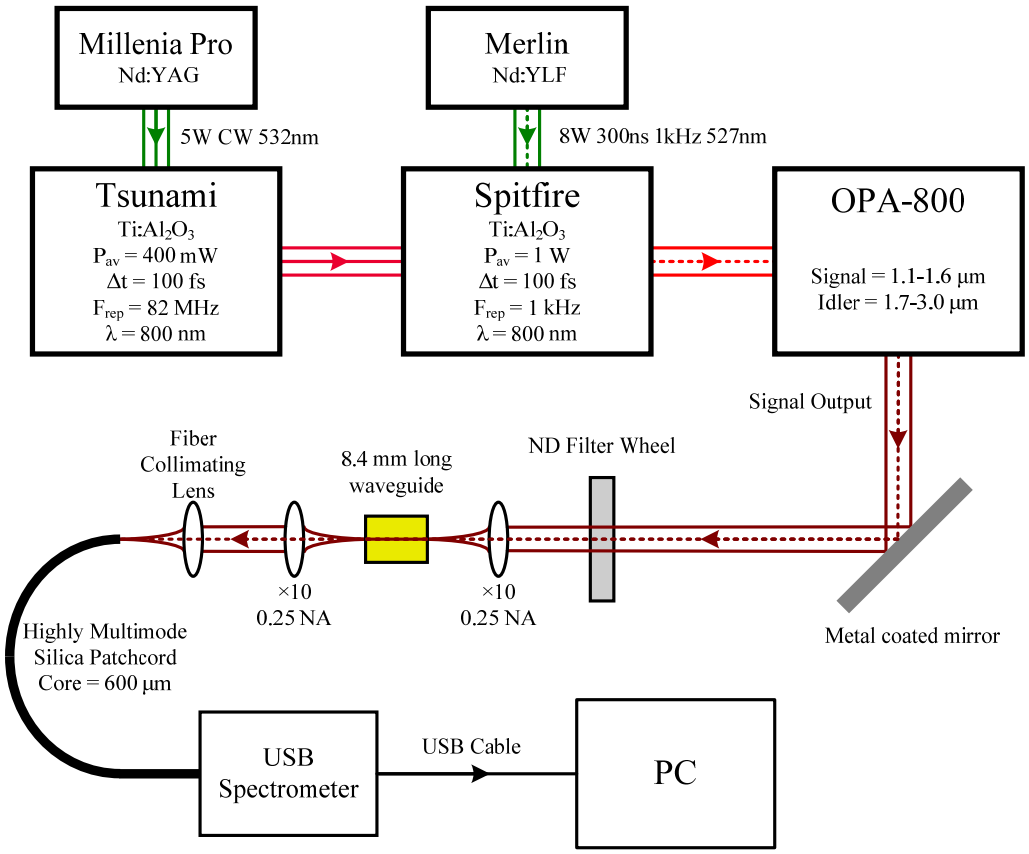

Figure 5-10. Experimental setup for supercontinuum generation.

The waveguides were pumped by an Optical Parametric Amplifier (OPA) (model Spectra Physics OPA-800) which was tuned to a central wavelength of 1500 nm. The bandwidth of the OPA was approximately 100 nm at the -15 dB points. The OPA was in turn pumped by a regeneratively amplified Ti:Sapphire laser (Spectra Physics Spitfire) emitting 1 mJ pulses at a repetition rate of 1 kHz with a pulse width of approximately 100 fs. The OPA pump source was linearly polarised and

aligned vertically. The output of the OPA was passed through a neutral density (ND) filter wheel and coupled into and out of the waveguide under test using ×10, 0.25 NA microscope objectives. The sample and both objectives were mounted on separate x-y-z translation stages. The output of the waveguide was coupled into a highly multimode silica patch cord (600 μm core) and fed into an Ocean Optics NIR512 near infrared spectrometer covering 850-1700 nm with a resolution of 3 nm. The patch cord was also fed separately into a BW-Tek BTC500E Mid-infrared spectrometer covering 1700-3000 nm with a resolution of 5 nm.

The two spectrometers were calibrated using an Ocean Optics LS1 broadband calibration source, which comprises a temperature controlled incandescent white light source operating with a black body spectrum at a colour temperature of 3000 K.

5.4.3 Supercontinuum results

Pulse energies of up to 11 μJ (measured before the coupling objective) at a repetition rate of 1 kHz were coupled into the waveguide under test. The small single-mode waveguide shown in Figure 5-9 was not able to be coupled into with high powers due to ablation occurring at the waveguide facet. The large multimode structures were able to guide significant amounts of the OPA light, however the focal plane of the input lens was moved *into* the sample in order to reduce the intensity at the waveguide facet, thus avoiding ablation. The broadest continuum was generated by the waveguide fabricated using 317 nJ pulses and a translation speed of 500 μm/s, as shown in Figure 5-7. The elongated central guiding region was used (as shown in Figure. 5-7 c)) as this gave the largest obtained signal and broadest continuum. Figure 5-11 shows the obtained continuum spectrum and corresponding pump spectrum from the OPA.

The supercontinuum obtained from the waveguide exhibits a -15 dB bandwidth spanning approximately 600 nm from 1320 nm to 1920 nm. The continuum is spectrally smooth, with a maximum peak to peak deviation of ±1.7 dB over the entire -15 dB bandwidth. No degradation was observed in the continuum

spectrum over a period of approximately 10 minutes during which the spectrum was captured, which indicates that photo-induced damaging effects such as photo-darkening had not occurred over these timescales.

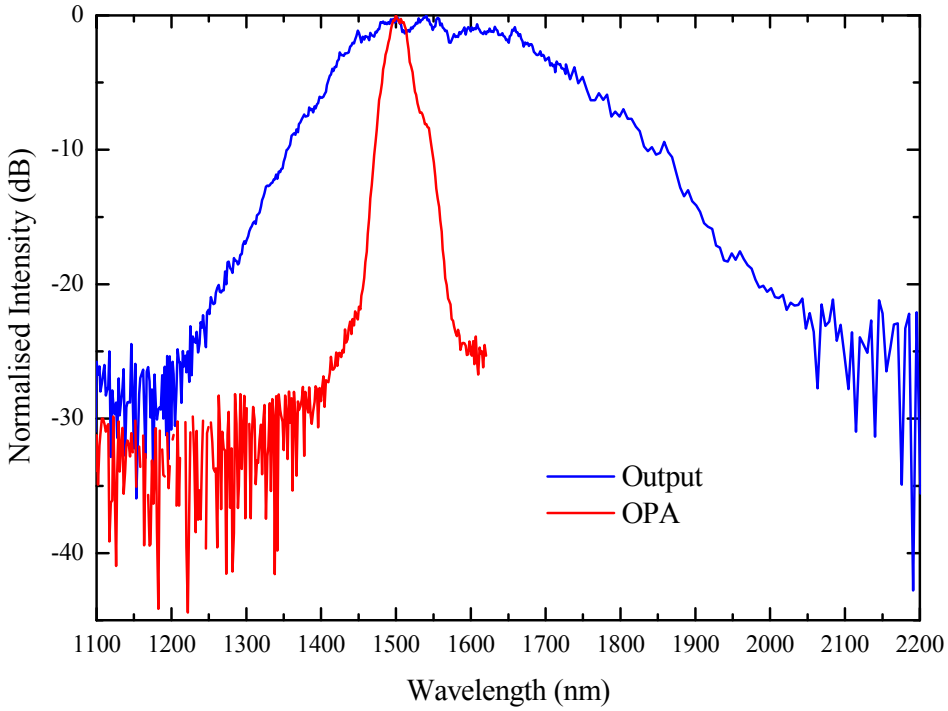

Figure 5-11. Supercontinuum generation from the ultrafast laser inscribed waveguide.

As the zero dispersion wavelength of chalcogenide glass is well in to the mid infrared, at around 5 μm, we are firmly in the normal dispersion regime. As a result, the primary contribution to spectral broadening is through strong self phase modulation (SPM) along with cross phase modulation (XPM). Pure SPM and XPM lead to strong symmetrical peaks modulating the continuum spectra which are not evident in the spectrum shown here; however the combination of SPM/XPM with normal dispersion has been shown to lead to significantly smoother spectra [170].

An additional reason for the spectral smoothness may be the highly multimode nature of the waveguide, so that each mode exhibits a different modal area and experiences a different effective nonlinearity and a different degree of broadening. When these spectra are combined at the output of the waveguide, the result is a

much smoother spectrum than would be expected for any one individual mode. Interestingly, the central wavelength of the continuum spectrum is also red shifted by 120 nm relative to the pump wavelength, indicating that the broadening is not only due to SPM and XPM but also includes a contribution from Raman scattering.

Using the same waveguide and guiding region, the idler port of the OPA, tuned to a central wavelength of 2.4 µm was aligned and coupled into the structure. Figure 5-12 shows the obtained supercontinuum spectrum.

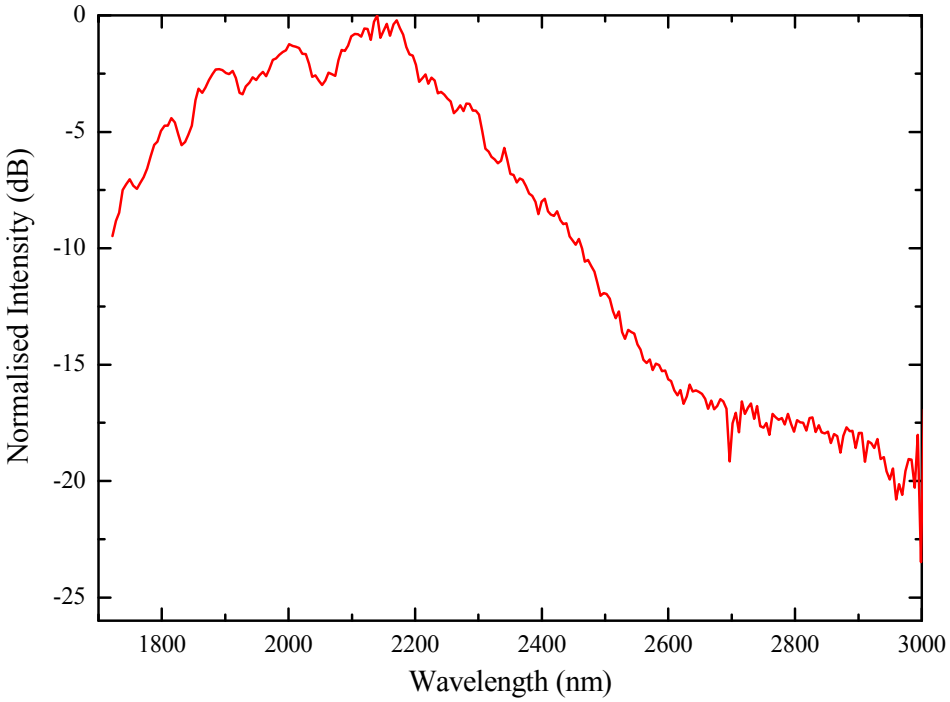

Figure 5-12. Supercontinuum generation when pumped with the idler port of the OPA tuned to 2.4 µm.

A broad continuum was generated in the mid-infrared extending up to approximately 2.6 µm. The obtained spectrum was unstable due to the poor stability of the idler output. The stability was particularly poor in the near-infrared region, preventing the capturing of a spectrum with the Ocean Optics spectrometer.

Upon inspecting the output of the idler port, it was clear that a significant amount of light at the signal wavelength of 1.5 µm was also present, which would cause

further nonlinear mixing and further wavelength generation with the idler. The generated spectrum shown in Figure 5-12 has a significant contribution from the 1.5 μm signal. Despite this, the spectrum shown in Figure 5-12 is the first demonstration of a truly mid-infrared supercontinuum from an ultrafast laser inscribed waveguide. Using a properly broadband coated filter would allow the 1.5 μm light to be removed from the idler output, however this was not available to be used.

Blomer *et al.* has shown that the nonlinear refractive index of fused silica is strongly affected by the ultrafast laser inscription process [171]. In particular, it was shown to be dependent upon the fabrication parameters, showing a strong decrease as more material modification was induced. This would suggest that using much lower pulse energies to fabricate waveguides may help to preserve the nonlinear refractive index n_2 and thus reduce the required pump pulse energies to generate a significant continuum. Unfortunately, surface ablation limited the amount of power which was able to be coupled into the waveguides fabricated with low pulse energies. In order to enable higher coupled powers into the single-mode waveguide, terminating the waveguide before the sample facet would prevent surface ablation whilst still providing good coupling efficiency.

Further improvements could also be achieved by using a glass composition with significantly higher n_2 such as GLS or Ge-As-Se based glasses. Another issue is that in the wavelength range used in this experiment, the strong positive GVD results in rapid temporal broadening of the pulse as it propagates through the waveguide, quickly reducing the peak powers and thus the amount of spectral broadening attained. This could potentially be addressed by controlling the position of the zero dispersion point through careful waveguide design or by fabricating a taper in the waveguide cross-section. Whilst it is desirable to remain in the normal dispersion regime for our application due to enhanced stability of the continuum, moving closer to the zero dispersion wavelength could improve the amount of broadening [172]. The use of a longer waveguide than the 8.4 mm used for these experiments could also dramatically improve performance and reduce the pulse energies required to create supercontinuum radiation.

5.5. CONCLUSIONS AND FURTHER WORK

The work presented in this chapter has contributed to the field in several ways. Firstly, the waveguides presented were the first bulk waveguides to be fabricated in an arsenic free chalcogenide glass using ULI. Secondly, the generation and guiding of mid-infrared light is the first demonstration within the field of ULI waveguides, opening up new application areas for this waveguide fabrication technique.

The supercontinuum generation experiments were the first report of continuum generation in waveguide fabricated using ULI. The supercontinuum obtained has potential for use in sensing and for OCT, where the stability and spectral smoothness has particular benefits in providing higher quality images than using conventional sources such as SLEDs and other continuum sources.

The work shown here could be progressed in several directions. The waveguide fabrication experiments were restricted to a single fabrication run on a 'one off' sample. Further fabrication experiments with a wider range of parameters may reveal different guiding regimes, and the use of multi-scan fabrication would allow greater control over the waveguide cross-section and refractive index contrast which would be particularly useful, especially for guiding mid-infrared wavelengths.

The mid-infrared guiding aspect has wide potential for the fabrication of optical sensor devices, as the fundamental absorption lines of many molecular species are present in this spectral region. Improved supercontinuum generation in the mid-infrared would provide a useful signal source for spectroscopic sensing in the mid-infrared, which could be coupled with passive mid-infrared waveguides to provide more complex sensing devices. The supercontinuum performance of the waveguides presented in this chapter could be improved by utilising the small single-mode waveguides, however surface ablation limited the amount of light that was able to be coupled into the structures. A termination in the waveguide well before the input facet would allow the focal plane of the input microscope

objective to be positioned well within the sample, reducing the surface intensity and reducing the likelihood of ablation taking place.

Integrated nonlinear optical devices such as all-optical switches could be fabricated with the optimisation of the substrate material and waveguide parameters to provide larger γ values. Nonlinear Mach-Zehnder modulators could be fabricated, which would provide low cost integrated all-optical switching in a compact format.

CHAPTER 6 – CONCLUSIONS AND FUTURE WORK

6.1 CONCLUSIONS

The work presented in this thesis has centred on the fabrication of optical waveguide devices in three separate material systems for three distinct applications. Chapters 3 and 4 present waveguide fabrication and characterisation experiments in novel laser gain media, and Chapter 5 presents waveguide fabrication and characterisation experiments in a highly nonlinear glass medium. The following provides a summary of the work presented in each chapter.

Chapter 3 presents waveguide fabrication work carried out in an erbium-doped oxyfluoride silicate glass. Optimisation of the waveguide writing parameters yielded low loss guiding using multi-scan fabrication and the use of low pulse energies. A low background insertion loss of 1.2 dB at 1537 nm was achieved, with coupling losses of 0.4 dB/facet and propagation losses of 0.3 dB/cm. Low loss waveguides were then fabricated in a wide range of dopant concentrations, with a peak net gain of 0.72 dB being achieved from a substrate doped with 1 wt% Er and 2 wt% Yb. This was the first demonstration of net gain in a non-phosphate Er-doped waveguide fabricated using ULI [173]. The relatively low amount of net gain achieved was found to be due to significant ion-clustering present in the substrate material. A laser cavity was constructed using FBGs either side of the waveguide amplifier. Laser action was observed, with textbook laser output power *vs* pump power characteristics [174]. The low output powers obtained were due to a modest amount of net gain provided by the substrate composition, the small sample length and an unoptimised cavity configuration.

Chapter 4 presents waveguide fabrication experiments carried out in novel Bismuth-doped glasses. Initially Bi-doped LAZS glass provided by the University of Leeds was used, with wide ranges of waveguide parameters fabricated. Both single and multi-scan fabrication were able to provide low-losses, with propagation losses of 0.3 dB/cm and coupling losses of 0.6 dB/facet. The waveguides exhibited ultra-broadband fluorescence centred on 1.3 μm under

diode pumping. This is the broadest fluorescence bandwidth observed for a waveguide fabricated using ULI [175]. No amplification was available from the waveguides, which was due to the substrate material being unable to provide gain. A proven material was sought, with waveguide fabrication subsequently being carried out in a Bi-doped alumino-silica glass provided by Osaka University. The fabricated waveguides were not able to provide particularly low-loss guiding, however large broadband internal gains of up to 6 dB/cm were observed for two lossy waveguides. The lack of gain on lower loss waveguides was attributed to the modification of the active Bi-centres by the ULI process. Despite this, the broadband internal gain of 6 dB/cm with more than 250 nm of bandwidth is a significant demonstration of the capabilities of this substrate material [176].

Chapter 5 presents waveguide fabrication work in a highly nonlinear germanium sulphide based chalcogenide glass. A wide range of waveguides were fabricated which were found to scale dramatically with the inscription parameters. At high pulse energies, highly multimode waveguides were produced, with several guiding regions. At the lowest pulse energy, small single-mode guiding was observed with a small mode field diameter of 5 × 6 μm. A γ value of 196 was calculated for this waveguide, indicating the potential for nonlinear integrated optics in these waveguides. Supercontinuum experiments were carried out by coupling in femtosecond pulses from a tunable optical parametric amplifier. A supercontinuum spanning 600 nm was generated, which was highly stable and spectrally smooth. This was the first such demonstration of supercontinuum generation from a waveguide fabricated using ULI and could have applications in OCT [177].

6.2 FUTURE WORK

It was concluded in Chapter 3 that the relatively low amount of net gain shown by the waveguides fabricated in Er doped oxyfluoride silicate glass was due to large amounts of ion clustering present in the host material. To progress the use of oxyfluoride silicate glass as an optical gain medium, significant optimisation of

the composition and dopant concentration is required. This could allow the achievement of much larger gain per unit length values. Some improvement to the amount of net gain could have been achieved by further optimisation of the waveguide parameters, and more importantly the provision of a longer sample. Once considerably more net gain is achieved, a wide range of devices could be fabricated, including telecoms devices such as high gain amplifiers and loss-less splitters, and laser based devices such as high power single longitudinal mode lasers and mode-locked lasers.

In Chapter 4, the lack of available gain from low-loss waveguides and the sole achievement of internal gain from two waveguides was found to be due the ULI process itself causing modification to the active Bi-centres in the material. In order to achieve net gain in Bi-doped material, modification to the substrate material is required. For example, the material could be designed such that the correct state of Bi is generated upon irradiation, or the substrate could be designed such that the form of Bi present in the material is restricted and cannot be changed. As the origin of the luminescence in Bi-doped systems is still a topic of considerable debate amongst the community, this may require some progression of the fabrication capabilities and knowledge of materials scientists. Another possible route would be to fabricate waveguide structures that allow considerable amounts of mode-overlap with unmodified material. Such an approach could make use of the large amounts of internal gain demonstrated from the Bi-doped material. Once net-gain has been achieved, a wide range of active devices could be fabricated, such as broadband optical amplifiers, high power tunable lasers and mode-locked lasers.

In Chapter 5, the chalcogenide waveguide fabrication was restricted to a single sample, with a single waveguide fabrication run. Considerable room for further waveguide parameter investigation experiments exists. In particular, the use of very low pulse energies combined with multi-scan fabrication could allow controllable large refractive index contrasts to be induced, which would enable three dimensional waveguides with tight bend radii to be fabricated. The mid-infrared guiding capabilities of the substrate material could be exploited for the

fabrication of a wide range of sensor devices, as many fundamental absorption lines of molecular species are within this spectral region. The optimisation of supercontinuum generation could be provided by controlling the waveguide dispersion through engineering of the waveguide structure or by fabricating waveguide tapers. This could enable low-threshold efficient supercontinuum generation in a small compact format, potentially being integrated with a mode-locked laser also fabricated using ULI. A range of integrated nonlinear optical devices could be fabricated such as all-optical switches, waveguide OPAs, and frequency shifters using XPM. All passive components could also be fabricated using ULI, enabling the integration of many components into a single substrate. The substrate itself could be further optimised in order to increase the nonlinear refractive index. Chalcogenides are capable of more than an order of magnitude greater in their n_2 values, which would immediately scale the value of γ accordingly and thus reduce the amount of power required to exploit the nonlinear properties.

REFERENCES

[1] D. Colladon, "On the reflections of a ray of light inside a parabolic liquid stream", *Comptes Rendus,* **15**, 800 (1842).

[2] J. Hecht, *City of light: the story of fiber optics* (Oxford University Press, USA, 2004).

[3] R. Shubert, and J. H. Harris, "Optical Surface Waves on Thin Films and Their Application to Integrated Data Processors," in *IEEE Transactions on Microwave Theory and Techniques* (1968), pp. 1048.

[4] P. K. Tien, "Light waves in thin films and integrated optics", *Applied Optics,* **10**, 2395 (1971).

[5] V. G. Ta'eed, M. D. Pelusi, B. J. Eggleton, D. Y. Choi, S. Madden, D. Bulla, and B. Luther-Davies, "Broadband wavelength conversion at 40 Gb/s using long serpentine As_2S_3 planar waveguides", *Optics Express,* **15**, 15047 (2007).

[6] E. J. Murphy, ed. *Integrated Optical Circuits and Components: Design and Applications* (CRC Press, 1999).

[7] D. Mattox, *Handbook of physical vapor deposition (PVD) processing* (Noyes Publications Westwood, NJ, 1998).

[8] K. Saenger, "Pulsed laser deposition: Part IA review of process characteristics and capabilities", *Processing of Advanced Materials,* **2**, 1 (1993).

[9] W. Huang, and R. R. A. Syms, "Sol-gel silica-on-silicon buried-channel EDWAs", *Journal of Lightwave Technology,* **21**, 1339 (2003).

[10] R. Srivastava, "Integrated optics by ion exchange", *Integrated Optics and Optoelectronics,* **CR45**, 126 (1993).

[11] L. McCaughan, "Critical materials issues in the performance and manufacturability of $LiNbO_3$ integrated optics", *Integrated Optics and Optoelectronics,* **CR45**, 15 (1993).

[12] H. Ebendorff-Heidepriem, "Laser writing of waveguides in photosensitive glasses", *Optical Materials,* **25**, 109 (2004).

[13] C. B. Schaffer, A. Brodeur, and E. Mazur, "Laser-induced breakdown and damage in bulk transparent materials induced by tightly focused femtosecond laser pulses", *Measurement Science & Technology,* **12**, 1784 (2001).

[14] L. Keldysh, "Ionization in the field of a strong electromagnetic wave", *Soviet Physics JETP,* **20**, (1964).

[15] N. Bloembergen, "Laser-Induced Electric Breakdown in Solids", *IEEE Journal of Quantum Electronics,* **Qe10**, 375 (1974).

[16] X. Liu, D. Du, and G. Mourou, "Laser ablation and micromachining with ultrashort laser pulses", *IEEE Journal of Quantum Electronics,* **33**, 1706 (1997).

[17] D. Du, X. Liu, G. Korn, J. Squier, and G. Mourou, "Laser-Induced Breakdown by Impact Ionization in SiO_2 with Pulse Widths from 7 ns to 150 fs", *Applied Physics Letters,* **64**, 3071 (1994).

[18] B. C. Stuart, M. D. Feit, A. M. Rubenchik, B. W. Shore, and M. D. Perry, "Laser-Induced Damage in Dielectrics with Nanosecond to Subpicosecond Pulses", *Physical Review Letters,* **74**, 2248 (1995).

[19] B. C. Stuart, M. D. Feit, S. Herman, A. M. Rubenchik, B. W. Shore, and M. D. Perry, "Nanosecond-to-femtosecond laser-induced breakdown in dielectrics", *Physical Review B,* **53**, 1749 (1996).

[20] B. C. Stuart, M. D. Feit, S. Herman, A. M. Rubenchik, B. W. Shore, and M. D. Perry, "Optical ablation by high-power short-pulse lasers", *Journal of the Optical Society of America B-Optical Physics,* **13**, 459 (1996).

[21] D. Du, X. Liu, and G. Mourou, "Reduction of multi-photon ionization in dielectrics due to collisions", *Applied Physics B - Lasers and Optics,* **63**, 617 (1996).

[22] M. Lenzner, J. Kruger, S. Sartania, Z. Cheng, C. Spielmann, G. Mourou, W. Kautek, and F. Krausz, "Femtosecond optical breakdown in dielectrics", *Physical Review Letters,* **80**, 4076 (1998).

[23] A. Kaiser, B. Rethfeld, M. Vicanek, and G. Simon, "Microscopic processes in dielectrics under irradiation by subpicosecond laser pulses", *Physical Review B,* **61**, 11437 (2000).

[24] L. N. Gaier, M. Lein, M. I. Stockman, P. L. Knight, P. B. Corkum, M. Y. Ivanov, and G. L. Yudin, "Ultrafast multiphoton forest fires and fractals in clusters and dielectrics", *Journal of Physics B - Atomic Molecular and Optical Physics,* **37**, L57 (2004).

[25] D. M. Rayner, A. Naumov, and P. B. Corkum, "Ultrashort pulse non-linear optical absorption in transparent media", *Optics Express,* **13**, 3208 (2005).

[26] E. N. Glezer, and E. Mazur, "Ultrafast-laser driven micro-explosions in transparent materials", *Applied Physics Letters,* **71**, 882 (1997).

[27] E. N. Glezer, M. Milosavljevic, L. Huang, R. J. Finlay, T. H. Her, J. P. Callan, and E. Mazur, "Three-dimensional optical storage inside transparent materials", *Optics Letters,* **21**, 2023 (1996).

[28] S. K. Sundaram, C. B. Schaffer, and E. Mazur, "Microexplosions in tellurite glasses", *Applied Physics A - Materials Science & Processing,* **76**, 379 (2003).

[29] E. Toratani, M. Kamata, and M. Obara, "Self-fabrication of void array in fused silica by femtosecond laser processing", *Applied Physics Letters,* **87**, 3 (2005).

[30] J. Ihlemann, B. Wolff, and P. Simon, "Nanosecond and femtosecond excimer laser ablation of fused silica", *Applied Physics A - Materials Science & Processing,* **54**, 363 (1992).

[31] P. R. Herman, R. S. Marjoribanks, A. Oettl, K. Chen, I. Konovalov, and S. Ness, "Laser shaping of photonic materials: deep-ultraviolet and ultrafast lasers", *Applied Surface Science,* **154**, 577 (2000).

[32] K. M. Davis, K. Miura, N. Sugimoto, and K. Hirao, "Writing waveguides in glass with a femtosecond laser", *Optics Letters,* **21**, 1729 (1996).

[33] C. B. Schaffer, A. Brodeur, J. F. Garcia, and E. Mazur, "Micromachining bulk glass by use of femtosecond laser pulses with nanojoule energy", *Optics Letters,* **26**, 93 (2001).

[34] A. M. Streltsov, and N. F. Borrelli, "Study of femtosecond-laser-written waveguides in glasses", *Journal of the Optical Society of America B - Optical Physics,* **19**, 2496 (2002).

[35] J. W. Chan, T. R. Huser, S. H. Risbud, J. S. Hayden, and D. M. Krol, "Waveguide fabrication in phosphate glasses using femtosecond laser pulses", *Applied Physics Letters,* **82**, 2371 (2003).

[36] C. B. Schaffer, J. F. Garcia, and E. Mazur, "Bulk heating of transparent materials using a high-repetition-rate femtosecond laser", *Applied Physics A - Materials Science & Processing,* **76**, 351 (2003).

[37] L. Sudrie, M. Franco, B. Prade, and A. Mysyrowicz, "Study of damage in fused silica induced by ultra-short IR laser pulses", *Optics Communications,* **191**, 333 (2001).

[38] Y. Shimotsuma, P. G. Kazansky, J. R. Qiu, and K. Hirao, "Self-organized nanogratings in glass irradiated by ultrashort light pulses", *Physical Review Letters,* **91**, 4 (2003).

[39] E. Bricchi, B. G. Klappauf, and P. G. Kazansky, "Form birefringence and negative index change created by femtosecond direct writing in transparent materials", *Optics Letters,* **29**, 119 (2004).

[40] P. P. Rajeev, M. Gertsvolf, C. Hnatovsky, E. Simova, R. S. Taylor, P. B. Corkum, D. M. Rayner, and V. R. Bhardwaj, "Transient nanoplasmonics inside dielectrics", *Journal of Physics B - Atomic Molecular and Optical Physics,* **40**, S273 (2007).

[41] M. Sakakura, and M. Terazima, "Oscillation of the refractive index at the focal region of a femtosecond laser pulse inside a glass", *Optics Letters,* **29**, 1548 (2004).

[42] M. Sakakura, and M. Terazima, "Initial temporal and spatial changes of the refractive index induced by focused femtosecond pulsed laser irradiation inside a glass", *Physical Review B,* **71**, (2005).

[43] M. Sakakura, M. Terazima, Y. Shimotsuma, K. Miura, and K. Hirao, "Heating and rapid cooling of bulk glass after photoexcitation by a focused femtosecond laser pulse", *Optics Express,* **15**, 16800 (2007).

[44] M. Sakakura, M. Terazima, Y. Shimotsuma, K. Miura, and K. Hirao, "Observation of pressure wave generated by focusing a femtosecond laser pulse inside a glass", *Optics Express,* **15**, 5674 (2007).

[45] S. H. Cho, H. Kumagai, and K. Midorikawa, "In situ observation of dynamics of plasma formation and refractive index modification in silica glasses excited by a femtosecond laser", *Optics Communications,* **207**, 243 (2002).

[46] W. Gawelda, D. Puerto, J. Siegel, A. Ferrer, A. R. de la Cruz, H. Fernandez, and J. Solis, "Ultrafast imaging of transient electronic plasmas produced in conditions of femtosecond waveguide writing in dielectrics", *Applied Physics Letters,* **93**, 3 (2008).

[47] K. Miura, J. R. Qiu, H. Inouye, T. Mitsuyu, and K. Hirao, "Photowritten optical waveguides in various glasses with ultrashort pulse laser", *Applied Physics Letters,* **71**, 3329 (1997).

[48] K. Hirao, and K. Miura, "Writing waveguides and gratings in silica and related materials by a femtosecond laser", *Journal of Non-Crystalline Solids,* **239**, 91 (1998).

[49] G. Cerullo, R. Osellame, S. Taccheo, M. Marangoni, D. Polli, R. Ramponi, P. Laporta, and S. De Silvestri, "Femtosecond micromachining of symmetric waveguides at 1.5 mu m by astigmatic beam focusing", *Optics Letters,* **27**, 1938 (2002).

[50] M. Ams, G. D. Marshall, D. J. Spence, and M. J. Withford, "Slit beam shaping method for femtosecond laser direct-write fabrication of symmetric waveguides in bulk glasses", *Optics Express,* **13**, 5676 (2005).

[51] J. R. Liu, Z. Y. Zhang, S. D. Chang, C. Flueraru, and C. P. Grover, "Directly writing in fused of 1-to-N optical waveguide power splitters silica glass using a femtosecond laser", *Optics Communications,* **253**, 315 (2005).

[52] Y. Nasu, M. Kohtoku, and Y. Hibino, "Low-loss waveguides written with a femtosecond laser for flexible interconnection in a planar light-wave circuit", *Optics Letters,* **30**, 723 (2005).

[53] R. R. Thomson, A. S. Bockelt, E. Ramsay, S. Beecher, A. H. Greenaway, A. K. Kar, and D. T. Reid, "Shaping ultrafast laser inscribed optical

waveguides using a deformable mirror", *Optics Express,* **16**, 12786 (2008).

[54] S. M. Eaton, H. Zhang, M. L. Ng, J. Z. Li, W. J. Chen, S. Ho, and P. R. Herman, "Transition from thermal diffusion to heat accumulation in high repetition rate femtosecond laser writing of buried optical waveguides", *Optics Express,* **16**, 9443 (2008).

[55] P. G. Kazansky, W. J. Yang, E. Bricchi, J. Bovatsek, A. Arai, Y. Shimotsuma, K. Miura, and K. Hirao, ""Quill" writing with ultrashort light pulses in transparent materials", *Applied Physics Letters,* **90**, 3 (2007).

[56] W. J. Yang, P. G. Kazansky, and Y. P. Svirko, "Non-reciprocal ultrafast laser writing", *Nature Photonics,* **2**, 99 (2008).

[57] Y. Sikorski, A. A. Said, P. Bado, R. Maynard, C. Florea, and K. A. Winick, "Optical waveguide amplifier in Nd-doped glass written with near-IR femtosecond laser pulses", *Electronics Letters,* **36**, 226 (2000).

[58] R. Osellame, S. Taccheo, G. Cerullo, M. Marangoni, D. Polli, R. Ramponi, P. Laporta, and S. De Silvestri, "Optical gain in Er-Yb doped waveguides fabricated by femtosecond laser pulses", *Electronics Letters,* **38**, 964 (2002).

[59] R. Osellame, S. Taccheo, M. Marangoni, R. Ramponi, P. Laporta, D. Polli, S. De Silvestri, and G. Cerullo, "Femtosecond writing of active optical waveguides with astigmatically shaped beams", *Journal of the Optical Society of America B-Optical Physics,* **20**, 1559 (2003).

[60] S. Taccheo, G. Della Valle, R. Osellame, G. Cerullo, N. Chiodo, P. Laporta, O. Svelto, A. Killi, U. Morgner, M. Lederer, and D. Kopf, "Er : Yb-doped waveguide laser fabricated by femtosecond laser pulses", *Optics Letters,* **29**, 2626 (2004).

[61] G. Della Valle, R. Osellame, N. Chiodo, S. Taccheo, G. Cerullo, P. Laporta, A. Killi, U. Morgner, M. Lederer, and D. Kopf, "C-band waveguide amplifier produced by femtosecond laser writing", *Optics Express,* **13**, 5976 (2005).

[62] S. M. Eaton, C. A. Merchant, R. Iyer, A. J. Zilkie, A. S. Helmy, J. S. Aitchison, P. R. Herman, D. Kraemer, R. J. D. Miller, C. Hnatovsky, and

R. S. Taylor, "Raman gain from waveguides inscribed in KGd(WO4)(2) by high repetition rate femtosecond laser", *Applied Physics Letters,* **92**, (2008).

[63] A. G. Okhrimchuk, A. V. Shestakov, I. Khrushchev, and J. Mitchell, "Depressed cladding, buried waveguide laser formed in a YAG : Nd^{3+} crystal by femtosecond laser writing", *Optics Letters,* **30**, 2248 (2005).

[64] G. A. Torchia, A. Rodenas, A. Benayas, E. Cantelar, L. Roso, and D. Jaque, "Highly efficient laser action in femtosecond-written Nd : yttrium aluminum garnet ceramic waveguides", *Applied Physics Letters,* **92**, 3 (2008).

[65] A. M. Streltsov, and N. F. Borrelli, "Fabrication and analysis of a directional coupler written in glass by nanojoule femtosecond laser pulses", *Optics Letters,* **26**, 42 (2001).

[66] K. Minoshima, A. M. Kowalevicz, I. Hartl, E. P. Ippen, and J. G. Fujimoto, "Photonic device fabrication in glass by use of nonlinear materials processing with a femtosecond laser oscillator", *Optics Letters,* **26**, 1516 (2001).

[67] K. Minoshima, A. M. Kowalevicz, E. P. Ippen, and J. G. Fujimoto, "Fabrication of coupled mode photonic devices in glass by nonlinear femtosecond laser materials processing", *Optics Express,* **10**, 645 (2002).

[68] C. Florea, and K. A. Winick, "Fabrication and characterization of photonic devices directly written in glass using femtosecond laser pulses", *Journal of Lightwave Technology,* **21**, 246 (2003).

[69] S. M. Eaton, W. Chen, L. Zhang, H. Zhang, R. Iyer, J. S. Aitchison, and P. R. Herman, "Telecom-band directional coupler written with femtosecond fiber laser", *IEEE Photonics Technology Letters,* **18**, 2174 (2006).

[70] W. J. Chen, S. M. Eaton, H. B. Zhang, and P. R. Herman, "Broadband directional couplers fabricated in bulk glass with high repetition rate femtosecond laser pulses", *Optics Express,* **16**, 11470 (2008).

[71] S. Nolte, M. Will, J. Burghoff, and A. Tuennermann, "Femtosecond waveguide writing: a new avenue to three-dimensional integrated optics", *Applied Physics A - Materials Science & Processing,* **77**, 109 (2003).

[72] A. M. Kowalevicz, V. Sharma, E. P. Ippen, J. G. Fujimoto, and K. Minoshima, "Three-dimensional photonic devices fabricated in glass by use of a femtosecond laser oscillator", *Optics Letters,* **30**, 1060 (2005).

[73] R. Osellame, V. Maselli, N. Chiodo, D. Polli, R. M. Vazquez, R. Ramponi, and G. Cerullo, "Fabrication of 3D photonic devices at 1.55 mu m wavelength by femtosecond Ti : Sapphire oscillator", *Electronics Letters,* **41**, 315 (2005).

[74] R. R. Thomson, H. T. Bookey, N. D. Psaila, A. Fender, S. Campbell, W. N. MacPherson, J. S. Barton, D. T. Reid, and A. K. Kar, "Ultrafast-laser inscription of a three dimensional fan-out device for multicore fiber coupling applications", *Optics Express,* **15**, 11691 (2007).

[75] G. D. Marshall, M. Ams, and M. J. Withford, "Direct laser written waveguide-Bragg gratings in bulk fused silica", *Optics Letters,* **31**, 2690 (2006).

[76] H. Zhang, S. M. Eaton, J. Li, and P. R. Herman, "Type II femtosecond laser writing of Bragg grating waveguides in bulk glass", *Electronics Letters,* **42**, 1223 (2006).

[77] H. B. Zhang, S. M. Eaton, J. Z. Li, A. H. Nejadmalayeri, and P. R. Herman, "Type II high-strength Bragg grating waveguides photowritten with ultrashort laser pulses", *Optics Express,* **15**, 4182 (2007).

[78] H. B. Zhang, S. M. Eaton, and P. R. Herman, "Single-step writing of Bragg grating waveguides in fused silica with an externally modulated femtosecond fiber laser", *Optics Letters,* **32**, 2559 (2007).

[79] G. D. Marshall, P. Dekker, M. Ams, J. A. Piper, and M. J. Withford, "Directly written monolithic waveguide laser incorporating a distributed feedback waveguide-Bragg grating", *Optics Letters,* **33**, 956 (2008).

[80] M. Ams, P. Dekker, G. D. Marshall, and M. J. Withford, "Monolithic 100 mW Yb waveguide laser fabricated using the femtosecond-laser direct-write technique", *Optics Letters,* **34**, 247 (2009).

[81] M. Kamata, M. Obara, R. R. Gattass, L. R. Cerami, and E. Mazur, "Optical vibration sensor fabricated by femtosecond laser micromachining", *Applied Physics Letters,* **87**, 3 (2005).

[82] H. B. Zhang, S. Ho, S. M. Eaton, J. Z. Li, and P. R. Herman, "Three-dimensional optical sensing network written in fused silica glass with femtosecond laser", *Optics Express,* **16**, 14015 (2008).

[83] Y. Bellouard, A. Said, M. Dugan, and P. Bado, "Fabrication of high-aspect ratio, micro-fluidic channels and tunnels using femtosecond laser pulses and chemical etching", *Optics Express,* **12**, 2120 (2004).

[84] R. Osellame, V. Maselli, R. M. Vazquez, R. Ramponi, and G. Cerullo, "Integration of optical waveguides and microfluidic channels both fabricated by femtosecond laser irradiation", *Applied Physics Letters,* **90**, (2007).

[85] Y. Bellouard, A. A. Said, and P. Bado, "Integrating optics and micro-mechanics in a single substrate: a step toward monolithic integration in fused silica", *Optics Express,* **13**, 6635 (2005).

[86] R. R. Thomson, S. Campbell, I. J. Blewett, A. K. Kar, and D. T. Reid, "Optical waveguide fabrication in z-cut lithium niobate ($LiNbO_3$) using femtosecond pulses in the low repetition rate regime", *Applied Physics Letters,* **88**, (2006).

[87] R. Osellame, M. Lobino, N. Chiodo, M. Marangoni, G. Cerullo, R. Ramponi, H. T. Bookey, R. R. Thomson, N. D. Psaila, and A. K. Kar, "Femtosecond laser writing of waveguides in periodically poled lithium niobate preserving the nonlinear coefficient", *Applied Physics Letters,* **90**, (2007).

[88] S. Campbell, R. R. Thomson, D. P. Hand, A. K. Kar, D. T. Reid, C. Canalias, V. Pasiskevicius, and F. Laurell, "Frequency-doubling in femtosecond laser inscribed periodically-poled potassium titanyl phosphate waveguides", *Optics Express,* **15**, 17146 (2007).

[89] A. Zoubir, M. Richardson, C. Rivero, A. Schulte, C. Lopez, K. Richardson, N. Ho, and R. Vallee, "Direct femtosecond laser writing of waveguides in As_2S_3 thin films", *Optics Letters,* **29**, 748 (2004).

[90] W. Yang, C. Corbari, P. G. Kazansky, K. Sakaguchi, and I. C. S. Carvalho, "Low loss photonic components in high index bismuth borate

glass by femtosecond laser direct writing", *Optics Express,* **16**, 16215 (2008).

[91] K. Miura, J. R. Qiu, S. Fujiwara, S. Sakaguchi, and K. Hirao, "Three-dimensional optical memory with rewriteable and ultrahigh density using the valence-state change of samarium ions", *Applied Physics Letters,* **80**, 2263 (2002).

[92] W. Watanabe, D. Kuroda, K. Itoh, and J. Nishii, "Fabrication of Fresnel zone plate embedded in silica glass by femtosecond laser pulses", *Optics Express,* **10**, 978 (2002).

[93] E. Desurvire, *Erbium-Doped Fiber Amplifiers : Principles and Applications* (Wiley, 2002).

[94] G. Keiser, *Optical communications essentials* (McGraw-Hill Professional, 2003).

[95] A. Polman, and F. van Veggel, "Broadband sensitizers for erbium-doped planar optical amplifiers: review", *Journal of the Optical Society of America B-Optical Physics,* **21**, 871 (2004).

[96] J. Canning, "Fibre lasers and related technologies", *Optics and Lasers in Engineering,* **44**, 647 (2006).

[97] S. X. Shen, and A. Jha, "The influence of F^--ion doping on the fluorescence ($^4I_{13/2}$ –> $^4I_{15/2}$) line shape broadening in Er^{3+}-doped oxyfluoride silicate glasses", *Optical Materials,* **25**, 321 (2004).

[98] R. Osellame, N. Chiodo, G. Della Valle, S. Taccheo, R. Ramponi, G. Cerullo, A. Killi, U. Morgner, M. Lederer, and D. Kopf, "Optical waveguide writing with a diode-pumped femtosecond oscillator", *Optics Letters,* **29**, 1900 (2004).

[99] G. Della Valle, R. Osellame, G. Galzerano, N. Chiodo, G. Cerullo, P. Laporta, and O. Svelto, "Passive mode locking by carbon nanotubes in a femtosecond laser written waveguide laser", *Applied Physics Letters,* **89**, (2006).

[100] G. Della Valle, S. Taccheo, R. Osellame, A. Festa, G. Cerullo, and P. Laporta, "1.5 μm single longitudinal mode waveguide laser fabricated by femtosecond laser writing", *Optics Express,* **15**, 3190 (2007).

[101] R. R. Thomson, S. Campbell, I. J. Blewett, A. K. Kar, D. T. Reid, S. Shen, and A. Jha, "Active waveguide fabrication in erbium-doped oxyfluoride silicate glass using femtosecond pulses", *Applied Physics Letters,* **87**, (2005).

[102] R. R. Thomson, H. T. Bookey, N. Psaila, S. Campbell, D. T. Reid, S. X. Shen, A. Jha, and A. K. Kar, "Internal gain from an erbium-doped oxyfluoride-silicate glass waveguide fabricated using femtosecond waveguide inscription", *IEEE Photonics Technology Letters,* **18**, 1515 (2006).

[103] A. Killi, U. Morgner, M. J. Lederer, and D. Kopf, "Diode-pumped femtosecond laser oscillator with cavity dumping", *Optics Letters,* **29**, 1288 (2004).

[104] P. Jeyagopal, R. Jaganathan, M. Kottaisamy, K. R. Kannan, and R. L. Narayanan, "Luminescence of Bi^{3+} in boron rich La_2O_3-CaO-B_2O_3 (glass and crystalline) ternary system", *Materials Research Bulletin,* **26**, 481 (1991).

[105] Y. Fujimoto, and M. Nakatsuka, "Infrared luminescence from bismuth-doped silica glass", *Japanese Journal of Applied Physics Part 2-Letters,* **40**, L279 (2001).

[106] X. G. Meng, M. Y. Peng, D. P. Chen, L. Y. Yang, X. W. Jiang, C. S. Zhu, and D. P. Qiu, "Broadband infrared luminescence of bismuth-doped borosilicate glasses", *Chinese Physics Letters,* **22**, 615 (2005).

[107] X. G. Meng, J. R. Qiu, M. Y. Peng, D. P. Chen, Q. Z. Zhao, X. W. Jiang, and C. S. Zhu, "Infrared broadband emission of bismuth-doped barium-aluminum-borate glasses", *Optics Express,* **13**, 1635 (2005).

[108] X. G. Meng, J. R. Qiu, M. Y. Peng, D. P. Chen, Q. Z. Zhao, X. W. Jiang, and C. S. Zhu, "Near infrared broadband emission of bismuth-doped aluminophosphate glass", *Optics Express,* **13**, 1628 (2005).

[109] M. Y. Peng, J. R. Qiu, D. P. Chen, X. G. Meng, and C. S. Zhu, "Superbroadband 1310 nm emission from bismuth and tantalum codoped germanium oxide glasses", *Optics Letters,* **30**, 2433 (2005).

[110] M. Y. Peng, C. Wang, D. P. Chen, J. R. Qiu, X. W. Jiang, and C. S. Zhu, "Investigations on bismuth and aluminum co-doped germanium oxide glasses for ultra-broadband optical amplification", *Journal of Non-Crystalline Solids,* **351**, 2388 (2005).

[111] Y. Fujimoto, and M. Nakatsuka, "Al-27 NMR structural study on aluminum coordination state in bismuth doped silica glass", *Journal of Non-Crystalline Solids,* **352**, 2254 (2006).

[112] H. P. Xia, and X. J. Wang, "Near infrared broadband emission from Bi^{5+}-doped Al_2O_3-GeO_2-X (X=Na_2O,BaO,Y_2O_3) glasses", *Applied Physics Letters,* **89**, 3 (2006).

[113] Y. Fujimoto, Y. Hirata, Y. Kuwada, T. Sato, and M. Nakatsuka, "Effect of GeO2 additive on fluorescence intensity enhancement in bismuth-doped silica glass", *Journal of Materials Research,* **22**, 565 (2007).

[114] A. G. Okhrimchuk, L. N. Butvina, E. M. Dianov, N. V. Lichkova, V. N. Zagorodnev, and K. N. Boldvrev, "Near-infrared luminescence of RbPb2Cl5 : Bi crystals", *Optics Letters,* **33**, 2182 (2008).

[115] J. J. Ren, G. P. Dong, S. Q. Xu, R. Q. Bao, and J. R. Qiu, "Inhomogeneous broadening, luminescence origin and optical amplification in bismuth-doped glass", *Journal of Physical Chemistry A,* **112**, 3036 (2008).

[116] V. O. Sokolov, V. G. Plotnichenko, and E. M. Dianov, "Origin of broadband near-infrared luminescence in bismuth-doped glasses", *Optics Letters,* **33**, 1488 (2008).

[117] M. Y. Peng, C. Zollfrank, and L. Wondraczek, "Origin of broad NIR photoluminescence in bismuthate glass and Bi-doped glasses at room temperature", *Journal of Physics-Condensed Matter,* **21**, 6 (2009).

[118] Y. Fujimoto, and M. Nakatsuka, "Optical amplification in bismuth-doped silica glass", *Applied Physics Letters,* **82**, 3325 (2003).

[119] E. M. Dianov, V. V. Dvoyrin, V. M. Mashinsky, A. A. Umnikov, M. V. Yashkov, and A. N. Gur'yanov, "CW bismuth fibre laser", *Quantum Electronics,* **35**, 1083 (2005).

[120] Y. S. Seo, Y. Fujimoto, and M. Nakatsuka, "Optical amplification in a bismuth-doped silica glass at 1300 nm telecommunications window", *Optics Communications,* **266**, 169 (2006).

[121] Y. S. Seo, Y. Fujimoto, and M. Nakatsuka, "Simultaneous amplification at two wavelengths near 1300 nm in a 6.5-cm-long bismuth-doped silica glass", *IEEE Photonics Technology Letters,* **18**, 1901 (2006).

[122] E. M. Dianov, A. V. Shubin, M. A. Melkumov, O. I. Medvedkov, and I. A. Bufetov, "High-power cw bismuth-fiber lasers", *Journal of the Optical Society of America B-Optical Physics,* **24**, 1749 (2007).

[123] V. V. Dvoyrin, V. M. Mashinsky, and E. M. Dianov, "Yb-Bi pulsed fiber lasers", *Optics Letters,* **32**, 451 (2007).

[124] I. Razdobreev, L. Bigot, V. Pureur, A. Favre, G. Bouwmans, and M. Douay, "Efficient all-fiber bismuth-doped laser", *Applied Physics Letters,* **90**, 3 (2007).

[125] J. Ren, B. Wu, X. Jiang, H. Dong, H. Zeng, and J. Qiu, "Broadband optical amplification near 1300 nm in bismuth-doped germanate glass", *Applied Physics B - Lasers and Optics,* **88**, 363 (2007).

[126] J. J. Ren, Y. B. Qiao, C. S. Zhu, X. W. Jiang, and J. R. Qiu, "Optical amplification near 1300 nm in bismuth-doped strontium germanate glass", *Journal of the Optical Society of America B - Optical Physics,* **24**, 2597 (2007).

[127] Y. S. Seo, C. Lim, Y. Fujimoto, and M. Nakatsuka, "9.6 dB, gain at a 1310 nm Wavelength for a bismuth-doped fiber amplifier", *Journal of the Optical Society of Korea,* **11**, 63 (2007).

[128] I. A. Bufetov, S. V. Firstov, V. E. Khopin, O. I. Medvedkov, A. N. Guryanov, and E. M. Dianov, "Bi-doped fiber lasers and amplifiers for a spectral region of 1300-1470 nm", *Optics Letters,* **33**, 2227 (2008).

[129] E. M. Dianov, S. V. Firstov, V. F. Khopin, O. I. Medvedkov, A. N. Guryanov, and I. A. Bufetov, "Bi-doped fibre lasers operating in the range 1470-1550 nm", *Quantum Electronics,* **39**, 299 (2009).

[130] E. M. Dianov, A. A. Krylov, V. V. Dvoyrin, V. M. Mashinsky, P. G. Kryukov, O. G. Okhotnikov, and M. Guina, "Mode-locked Bi-doped fiber

laser", *Journal of the Optical Society of America B - Optical Physics,* **24**, 1807 (2007).

[131] S. Kivisto, J. Puustinen, M. Guina, O. G. Okhotnikov, and E. M. Dianov, "Tunable modelocked bismuth-doped soliton fibre laser", *Electronics Letters,* **44**, 1456 (2008).

[132] S. Kivisto, R. Gumenyuk, J. Puustinen, M. Guina, E. M. Dianov, and O. G. Okhotnikov, "Mode-Locked Bi-Doped All-Fiber Laser With Chirped Fiber Bragg Grating", *IEEE Photonics Technology Letters,* **21**, 599 (2009).

[133] C. Batchelor, W. J. Chung, S. Shen, and A. Jha, "Enhanced room-temperature emission in Cr^{4+} ions containing alumino-silicate glasses", *Applied Physics Letters,* **82**, 4035 (2003).

[134] M. Y. Peng, X. G. Meng, D. P. Chen, and J. R. Qiu, "Comment on "Enhanced room-temperature emission in Cr^{4+} ions containing alumino-silicate glasses" [Appl. Phys. Lett. 82, 4035 (2003)]", *Applied Physics Letters,* **87**, 2 (2005).

[135] J. R. Liu, Z. Y. Zhang, C. Flueraru, X. P. Liu, S. D. Chang, and C. P. Grover, "Waveguide shaping and writing in fused silica using a femtosecond laser", *IEEE Journal of Selected Topics in Quantum Electronics,* **10**, 169 (2004).

[136] M. Young, "Optical fiber index profiles by the refracted-ray method (Refracted Near-field Scanning)", *Applied Optics,* **20**, 3415 (1981).

[137] P. Oberson, B. Gisin, B. Huttner, and N. Gisin, "Refracted near-field measurements of refractive index and geometry of silica-on-silicon integrated optical waveguides", *Applied Optics,* **37**, 7268 (1998).

[138] T. Suzuki, and Y. Ohishi, "Ultrabroadband near-infrared emission from Bi-doped Li_2O-Al_2O_3-SiO_2 glass", *Applied Physics Letters,* **88**, 3 (2006).

[139] S. F. Zhou, H. F. Dong, H. P. Zeng, G. F. Feng, H. C. Yang, B. Zhu, and J. R. Qiu, "Broadband optical amplification in Bi-doped germanium silicate glass", *Applied Physics Letters,* **91**, 3 (2007).

[140] S. F. Zhou, W. Q. Lei, J. X. Chen, J. H. Hao, H. P. Zeng, and J. R. Qiu, "Laser-Induced Optical Property Changes Inside Bi-Doped Glass", *IEEE Photonics Technology Letters,* **21**, 386 (2009).

[141] S. F. Zhou, W. Q. Lei, N. Jiang, J. H. Hao, E. Wu, H. P. Zeng, and J. R. Qiu, "Space-selective control of luminescence inside the Bi-doped mesoporous silica glass by a femtosecond laser", *Journal of Materials Chemistry,* **19**, 4603 (2009).

[142] A. B. Seddon, "Chalcogenide glasses - A review of their preparation, properties and applications", *Journal of Non-Crystalline Solids*, 44 (1994).

[143] M. Asobe, T. Ohara, I. Yokohama, and T. Kaino, "Low power all-optical switching in a nonlinear optical loop mirror using chalcogenide glass fibre", *Electronics Letters,* **32**, 1396 (1996).

[144] A. Ganjoo, H. Jain, C. Yu, R. Song, J. V. Ryan, J. Irudayaraj, Y. J. Ding, and C. G. Pantano, "Planar chalcogenide glass waveguides for IR evanescent wave sensors", *Journal of Non-Crystalline Solids,* **352**, 584 (2006).

[145] V. G. Ta'eed, N. J. Baker, L. B. Fu, K. Finsterbusch, M. R. E. Lamont, D. J. Moss, H. C. Nguyen, B. J. Eggleton, D. Y. Choi, S. Madden, and B. Luther-Davies, "Ultrafast all-optical chalcogenide glass photonic circuits", *Optics Express,* **15**, 9205 (2007).

[146] J. T. Gopinath, M. Soljacic, E. P. Ippen, V. N. Fuflyigin, W. A. King, and M. Shurgalin, "Third order nonlinearities in Ge-As-Se-based glasses for telecommunications applications", *Journal of Applied Physics,* **96**, 6931 (2004).

[147] A. Zakery, and S. R. Elliott, "Optical properties and applications of chalcogenide glasses: a review", *Journal of Non-Crystalline Solids,* **330**, 1 (2003).

[148] R. S. Quimby, and B. G. Aitken, "Multiphonon energy gap law in rare-earth doped chalcogenide glass", *Journal of Non-Crystalline Solids,* **320**, 100 (2003).

[149] J. H. Lee, T. Nagashima, T. Hasegawa, S. Ohara, N. Sugimoto, and K. Kikuchi, "Bismuth-oxide-based nonlinear fiber with a high SBS threshold and its application to four-wave-mixing wavelength conversion using a pure continuous-wave pump", *Journal of Lightwave Technology,* **24**, 22 (2005).

[150] M. D. Pelusi, V. G. Ta'eed, L. B. Fu, E. Magi, M. R. E. Lamont, S. Madden, D. Y. Choi, D. A. P. Bulla, B. Luther-Davies, and B. J. Eggleton, "Applications of highly-nonlinear chalcogenide glass devices tailored for high-speed all-optical signal processing", *IEEE Journal of Selected Topics in Quantum Electronics,* **14**, 529 (2008).

[151] V. G. Ta'eed, L. B. Fu, M. Pelusi, M. Rochette, I. C. M. Littler, D. J. Moss, and B. J. Eggleton, "Error free all optical wavelength conversion in highly nonlinear As-Se chalcogenide glass fiber", *Optics Express,* **14**, 10371 (2006).

[152] M. R. E. Lamont, L. B. Fu, M. Rochette, D. J. Moss, and B. J. Eggleton, "2R optical regenerator in As_2Se_3 chalcogenide fiber characterized by a frequency-resolved optical gating analysis", *Applied Optics,* **45**, 7904 (2006).

[153] P. A. Thielen, L. B. Shaw, P. C. Pureza, V. Q. Nguyen, J. S. Sanghera, and I. D. Aggarwal, "Small-core As-Se fiber for Raman amplification", *Optics Letters,* **28**, 1406 (2003).

[154] J. F. Viens, C. Meneghini, A. Villeneuve, T. V. Galstian, E. J. Knystautas, M. A. Duguay, K. A. Richardson, and T. Cardinal, "Fabrication and characterization of integrated optical waveguides in sulfide chalcogenide glasses", *Journal of Lightwave Technology,* **17**, 1184 (1999).

[155] S. J. Madden, D. Y. Choi, D. A. Bulla, A. V. Rode, B. Luther-Davies, V. G. Ta'eed, M. D. Pelusi, and B. J. Eggleton, "Long, low loss etched As_2S_3 chalcogenide waveguides for all-optical signal regeneration", *Optics Express,* **15**, 14414 (2007).

[156] M. R. E. Lamont, V. G. Ta'eed, M. A. F. Roelens, D. J. Moss, B. J. Eggleton, D. Y. Choi, S. Madden, and B. Luther-Davies, "Error-free

wavelength conversion via cross-phase modulation in 5cm of As_2S_3 chalcogenide glass rib waveguide", *Electronics Letters,* **43**, 945 (2007).

[157] M. D. Pelusi, V. G. Ta'eed, M. R. E. Lamont, S. Madden, D. Y. Choi, B. Luther-Davies, and B. J. Eggleton, "Ultra-high Nonlinear As_2S_3 planar waveguide for 160-Gb/s optical time-division demultiplexing by four-wave mixing", *IEEE Photonics Technology Letters,* **19**, 1496 (2007).

[158] M. R. E. Lamont, B. Luther-Davies, D. Y. Choi, S. Madden, and B. J. Eggleton, "Supercontinuum generation in dispersion engineered highly nonlinear (γ=10/W/m) As_2S_3 chalcogenide planar waveguide", *Optics Express,* **16**, 14938 (2008).

[159] M. R. E. Lamont, B. Luther-Davies, D. Y. Choi, S. Madden, X. Gai, and B. J. Eggleton, "Net-gain from a parametric amplifier on a chalcogenide optical chip", *Optics Express,* **16**, 20374 (2008).

[160] M. Galili, J. Xu, H. C. H. Mulvad, L. K. Oxenlowe, A. T. Clausen, P. Jeppesen, B. Luther-Davies, S. Madden, A. Rode, D. Y. Choi, M. Pelusi, F. Luan, and B. J. Eggleton, "Breakthrough switching speed with an all-optical chalcogenide glass chip: 640 Gbit/s demultiplexing", *Optics Express,* **17**, 2182 (2009).

[161] O. M. Efimov, L. B. Glebov, K. A. Richardson, E. Van Stryland, T. Cardinal, S. H. Park, M. Couzi, and J. L. Bruneel, "Waveguide writing in chalcogenide glasses by a train of femtosecond laser pulses", *Optical Materials,* **17**, 379 (2001).

[162] M. Hughes, W. Yang, and D. Hewak, "Fabrication and characterization of femtosecond laser written waveguides in chalcogenide glass", *Applied Physics Letters,* **90**, 3 (2007).

[163] L. Petit, N. Carlie, T. Anderson, J. Choi, M. Richardson, and K. C. Richardson, "Progress on the Photoresponse of Chalcogenide Glasses and Films to Near-Infrared Femtosecond Laser Irradiation: A Review", *IEEE Journal of Selected Topics in Quantum Electronics,* **14**, 1323 (2008).

[164] T. Anderson, L. Petit, N. Carlie, J. Choi, J. Hu, A. Agarwal, L. Kimerling, K. Richardson, and M. Richardson, "Femtosecond laser photo-response of $Ge_{23}Sb_7S_{70}$ films", *Optics Express,* **16**, 20081 (2008).

[165] K. S. Bindra, H. T. Bookey, A. K. Kar, B. S. Wherrett, X. Liu, and A. Jha, "Nonlinear optical properties of chalcogenide glasses: Observation of multiphoton absorption", *Applied Physics Letters,* **79**, 1939 (2001).

[166] H. Bookey, "Linear and Nonlinear optics of Chalcogenide bulk glasses and fibre for ultrafast all optical switching," in *Department of Physics* (Heriot Watt University, 2004).

[167] G. Agrawal, "Nonlinear fiber optics," in *Academic, New York* (Elsevier, 2007), p. 35.

[168] I. Hartl, X. D. Li, C. Chudoba, R. K. Ghanta, T. H. Ko, J. G. Fujimoto, J. K. Ranka, and R. S. Windeler, "Ultrahigh-resolution optical coherence tomography using continuum generation in an air-silica microstructure optical fiber", *Optics Letters.,* **26**, 608 (2001).

[169] B. Schenkel, R. Paschotta, and U. Keller, "Pulse compression with supercontinuum generation in microstructure fibers", *Journal of the Optical Society of America B - Optical Physics,* **22**, 687 (2005).

[170] W. J. Tomlinson, R. H. Stolen, and C. V. Shank, "Compression of optical pulses chirped by self-phase modulation in fibers", *Journal of the Optical Society of America,* **1**, 139 (1984).

[171] D. Blomer, A. Szameit, F. Dreisow, T. Schreiber, S. Nolte, and A. Tunnermann, "Nonlinear refractive index of fs-laser-written waveguides in fused silica", *Optics Express,* **14**, 2151 (2006).

[172] K. R. Tamura, H. Kubota, and M. Nakazawa, "Fundamentals of stable continuum generation at high repetition rates", *IEEE Journal of Quantum Electronics,* **36**, 773 (2000).

[173] N. D. Psaila, R. R. Thomson, H. T. Bookey, A. K. Kar, N. Chiodo, R. Osellame, G. Cerullo, A. Jha, and S. Shen, "Er : Yb-doped oxyfluoride silicate glass waveguide amplifier fabricated using femtosecond laser inscription", *Applied Physics Letters,* **90**, (2007).

[174] N. D. Psaila, R. R. Thomson, H. T. Bookey, N. Chiodo, S. Shen, R. Osellame, G. Cerullo, A. Jha, and A. K. Kar, "Er : Yb-doped oxyfluoride silicate glass waveguide laser fabricated using ultrafast laser inscription", *IEEE Photonics Technology Letters,* **20**, 126 (2008).

[175] N. D. Psaila, R. R. Thomson, H. T. Bookey, A. K. Kar, N. Chiodo, R. Osellame, G. Cerullo, G. Brown, A. Jha, and S. Shen, "Femtosecond laser inscription of optical waveguides in bismuth ion doped glass", *Optics Express,* **14**, 10452 (2006).

[176] N. Psaila, R. R. Thomson, H. T. Bookey, A. K. Kar, Y. Fujimoto, M. Nakatsuka, N. Chiodo, R. Osellame, and G. Cerullo, "Ultra Broadband Gain from a Bismuth-doped Glass Waveguide Fabricated Using Ultrafast Laser Inscription", *2008 Conference on Lasers and Electro-Optics & Quantum Electronics and Laser Science Conference, Vols 1-9*, 2215 (2008).

[177] N. D. Psaila, R. R. Thomson, H. T. Bookey, S. X. Shen, N. Chiodo, R. Osellame, G. Cerullo, A. Jha, and A. K. Kar, "Supercontinuum generation in an ultrafast laser inscribed chalcogenide glass waveguide", *Optics Express,* **15**, 15776 (2007).

APPENDIX

MATLAB code used for the calculation of γ:

```
clear all;

%set all constants to be used

n2 = 6e-19;          %nonlinear refractive index of substrate in m^2 W^-1
lambda = 1.48e-6;    %wavelength in m
pii = 3.1415926535

%Import x scale and values

fileimport = (uiimport);
profcell = struct2cell(fileimport);
xdata = profcell{1,1};
xscale = xdata(1:(length(xdata)),1);
xvalue = xdata(1:(length(xdata)),2);

xscale = xscale.*(1e-6) %convert to metres

%Import y scale and values

fileimport = (uiimport);
profcell = struct2cell(fileimport);
ydata = profcell{1,1};
yscale = ydata(1:(length(ydata)),1);
yvalue = ydata(1:(length(ydata)),2);

yscale = yscale.*(1e-6) %convert to metres

%Calculate square and quad power of each

xsquare = xvalue.^2;
xquad = xvalue.^4;
ysquare = yvalue.^2;
yquad = yvalue.^4;

%Integrate xsquare

for i = 1:(length(xsquare)-1);
    xsqintcal(i) = (((xsquare(i+1) - xsquare(i))/2) + xsquare(i)) * xscale(2)
end
xsqint = sum(xsqintcal);

%Integrate xquad

for i = 1:(length(xquad)-1);
    xquintcal(i) = (((xquad(i+1) - xquad(i))/2) + xquad(i)) * xscale(2);
end
xquint = sum(xquintcal);

%Integrate ysquare

for i = 1:(length(ysquare)-1);
```

```
    ysqintcal(i) = (((ysquare(i+1) - ysquare(i))/2) + ysquare(i)) * yscale(2)
end
ysqint = sum(ysqintcal);

%Integrate yquad

for i = 1:(length(yquad)-1);
    yquintcal(i) = (((yquad(i+1) - yquad(i))/2) + yquad(i)) * yscale(2);
end
yquint = sum(yquintcal);

%Calculate Aeff

AeffX = (xsqint^2)/xquint
AeffY = (ysqint^2)/yquint

Aeff = AeffX * AeffY

%Calculate gamma

gamma = (2 * pii * n2) / (lambda * Aeff)

gamma = gamma * 1000 %calculate gamma in W^-1 km^-1

gamma %display gamma value
```